


SURFACE-ENHANCED RAMAN SPECTROSCOPY OF BLOOD COMPONENTS
WITH THE AIM OF CANCER DIAGNOSIS



by
Ertuğ Avcı

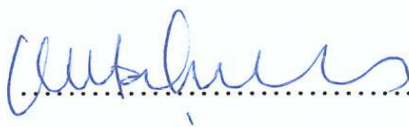
Submitted to Graduate School of Natural and Applied Sciences
in Partial Fulfillment of the Requirements
for the Degree of Doctor of Philosophy in
Biotechnology

Yeditepe University
2019

SURFACE-ENHANCED RAMAN SPECTROSCOPY OF BLOOD COMPONENTS
WITH THE AIM OF CANCER DIAGNOSIS

APPROVED BY:

Prof. Dr. Mustafa Çulha
(Thesis Supervisor)
(Yeditepe University)



Assist. Prof. Dr. Andrew John Harvey
(Yeditepe University)



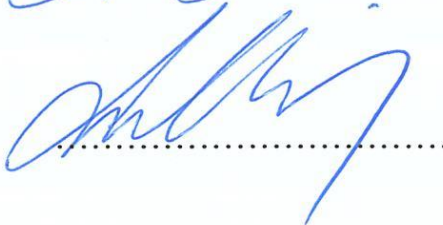
Assist. Prof. Dr. Hüseyin Çimen
(Yeditepe University)



Assist. Prof. Dr. Kaan Keçeci
(İstanbul Medeniyet University)



Assist. Prof. Dr. Sultan Sibel Erdem
(İstanbul Medipol University)



DATE OF APPROVAL:/...../2019

ACKNOWLEDGEMENTS

I would like to thank my supervisor Prof. Mustafa ulha for giving me the opportunity to study in his laboratory and for supporting me throughout the years with his suggestions, advices, and comments. It was very good for me to work with a hardworking, successful, and meantime, humble professor.

I am also grateful to my thesis monitoring committee members Assist Prof. Andrew J. Harvey and Assist. Prof. Kaan Keeci for their helps, comments and suggestions during my thesis monitor meetings.

I would like to thank Assoc. Prof. Soner Doėan for providing me blood serum samples and for his help and suggestions. I'm also thankful to Assist. Prof. Bilge Gven Tuna, Assoc. Prof. Fatih Altıntoprak, Assoc. Prof. Kayhan Baėak, Prof. Mehmer Eser, Dr. İsmail Zengin, and M.Sc. Mnevver B. iekdal for providing me blood serum samples.

I would like to thank all my friends in Yeditepe University. I have met many friends and I have learned many from them. Thank you my friends!

I would like to thank Yeditepe University for providing me a good environment for studying and providing me financial support.

ABSTRACT

SURFACE-ENHANCED RAMAN SPECTROSCOPY OF BLOOD COMPONENTS WITH THE AIM OF CANCER DIAGNOSIS

Cancer is among the most common diseases in the world. Early detection of cancer is critically important to improve prognosis and increase cure rates. Although there are screening methods which involve imaging techniques or tumor marker finding in blood, faster and cost effective other methods must be developed when the seriousness of the disease is considered. Recent years, surface-enhanced Raman spectroscopy (SERS) has started to show its potential to be used as an alternative technique in clinics. Among the applications of the technique, the use of label-free SERS for cancer screening in blood is newly emerging. In this study, SERS analysis on blood serum samples was applied for cancer detection using silver nanoparticles (AgNPs) as SERS substrates. For this aim, SERS spectra of binary mixtures of blood proteins were acquired first. It was found that partial least squares-discriminant analysis (PLS-DA) is better method than principal component analysis (PCA) in order to differentiate large proteins. It was shown that using different concentrations of AgNPs for SERS study of serum and comparison of the acquired spectra provides valuable information about the origins of the blood serum spectrum. Addition of three proteins as models (human serum albumin, transferrin, and lysozyme) to filtered serum showed that proteins directly affect the spectral shape without contributing any SERS bands. Then, discrimination of serum samples of cancer patients from healthy individuals and from the patients with chronic diseases were performed using partial least squares-discriminant analysis (PLS-DA) on SERS data. Over 90 percent diagnostic accuracies were achieved in most of the tests. Moreover, when SERS spectra of the blood serum samples obtained from cancer patients before tumor removal and after tumor removal were compared it was observed that spectral patterns of serum samples after tumor removal were similar to spectral patterns of serum samples of healthy individuals. The data in this thesis suggest that SERS study of serum has potential to be used as a quick and cost effective tool for cancer detection and its differentiation from other chronic diseases in clinics.

ÖZET

KAN BİLEŞENLERİNİN YÜZEYDE-ZENGİNLEŞTİRİLMİŞ RAMAN SPEKTROSKOPİSİ İLE KANSER TANISI AMAÇLI ANALİZİ

Kanser dünyadaki en yaygın hastalıklardan birisidir. Bu nedenle erken kanser tespiti, prognozun iyileşmesi ve tedavi oranının artması için oldukça önemlidir. Çeşitli görüntüleme teknikleri ve tümör belirteçleri bulunmasına dayalı metotlar halihazırda kullanılıyor olsa da hastalığın ciddiyeti göz önüne alındığında daha hızlı ve daha ucuz yeni tekniklerin geliştirilmesi gerekmektedir. Son yıllarda, yüzeyde-zenginleştirilmiş Raman spektroskopisi (YZRS), alternatif bir teknik olarak klinikte kullanılabilme potansiyeli göstermektedir. Bu çalışmada, YZRS ile kan serumu örneklerinin kanser tespiti amaçlı analizi gümüş nanopartiküllerin (GNP) YZRS süstratı olarak kullanılmasıyla gerçekleştirildi. Bunun için, ilk olarak, ikili protein karışımlarının YZRS spektrumları çalışıldı. Kısmi en küçük karelerin diskriminant analizinin (KEKK-DA) büyük proteinleri ayırt edebilmede temel bileşenler analizinden (TBA) daha verimli olduğu görüldü. İlave olarak, serumun YZRS spektrumlarının kaynağının neler olduğunu anlamak için farklı GNP derişimlerinin kullanılıp elde edilen spektrumların karşılaştırılması gerektiği bulundu. Proteinlerin, serumun YZRS spektrumunu etkilediği ama bunu kendi spektrumlarını serum spektrumuna katmadan yaptıkları üç farklı protein kullanılarak gösterildi. Kanser hastalarının serumlarının sağlıklı bireylerin serumlarından ve kronik hastalığa sahip kişilerin serumlarından ayır edilmesi YZRS verilerine KEKK-DA uygulanarak gerçekleştirildi. Testlerin çoğunda yüzde doksan üstü tanısal genel doğruluğa ulaşıldı. İlave olarak, kanser hastalarından tümör alımı operasyonu öncesi ve sonrası alınan serumların YZRS spektrumları karşılaştırıldığında, tümör alındıktan sonraki spektrumun sağlıklı bireylerin serum spektrumlarına tümör alımı öncesi alınan serumların spektrumlarından daha çok benzediği gözlemlendi. Bu tez çalışmasındaki veriler kanser tanısında ve kanserin diğer kronik hastalıklardan ayırt edilebilmesinde YZRS'nin çabuk ve daha az maliyetli bir yöntem olarak kliniklerde kullanılabilme potansiyeli olduğunu göstermektedir.

TABLE OF CONTENTS

ACKNOWLEDGEMENTS.....	iii
ABSTRACT.....	iv
ÖZET	v
LIST OF FIGURES	viii
LIST OF TABLES.....	xvii
LIST OF SYMBOLS/ABBREVIATIONS.....	xx
1. INTRODUCTION.....	1
1.1. CANCER AND ITS DIAGNOSIS.....	1
1.2. RAMAN SPECTROSCOPY	4
1.2.1. Raman Scattering.....	4
1.2.2. Basic Theory of Raman Scattering.....	9
1.2.3. Raman Instrument.....	12
1.2.4. Plasmonics	13
1.2.5. Surface-Enhanced Raman Scattering.....	15
1.2.6. A Review of Current Literature on Label-Free Cancer Detection Based on Blood plasma and Serum SERS	17
2. AIM OF THE STUDY	20
3. MATERIALS AND METHODS	21
3.1. CHEMICALS AND MATERIALS.....	21
3.2. SILVER NANOPARTICLE SYNTHESIS	21
3.3. SAMPLE PREPARATION	22
3.3.1. Preparation of Protein Mixtures for SERS Study of Binary Mixtures of Proteins	22
3.3.2. Preparation of Solutions.....	22
3.3.3. Preparation of Blood Serum Samples.....	23
3.4. SERS EXPERIMENTAL SETUP.....	25
3.5. SERS DATA PROCESSING	25

4. RESULTS AND DISCUSSION.....	26
4.1. CHARACTERIZATION OF SILVER NANOPARTICLES.....	26
4.2. INFLUENCE OF PROTEIN SIZE ON SURFACE-ENHANCED RAMAN SCATTERING SPECTRA IN BINARY PROTEIN MIXTURES	28
4.3. LABEL-FREE SURFACE-ENHANCED RAMAN SCATTERING FOR CANCER DETECTION	51
4.3.1. Reproducibility of the SERS Spectra of Filtered and Unfiltered Serum	51
4.3.2. On the Origins of Serum SERS Spectra	58
4.3.3. SERS Study of Purines and Purine Derivatives.....	63
4.3.4. Discrimination of Cancer and Chronic Diseases Using SERS	74
5. CONCLUSIONS AND FUTURE PERSPECTIVES.....	113
REFERENCES	115
APPENDIX A.....	130

LIST OF FIGURES

Figure 1.1. Jablonski diagram of energy transitions for absorption, fluorescence, phosphorescence, Rayleigh scattering, and Raman scattering (Stokes scattering and Anti-Stokes scattering).	7
Figure 1.2. Raman spectrum of a LiNbO ₃ single crystal.	8
Figure 1.3. Information obtained from a Raman spectrum.	9
Figure 1.4. Wave model for Rayleigh, Stokes, and anti-Stokes scattering.	11
Figure 1.5. Components of a Raman instrument.	12
Figure 1.6. Lasers of a Raman instrument.	13
Figure 1.7. Illustration of localized surface plasmon resonance.	14
Figure 1.8. The UV-Vis spectra of AgNPs with different sizes, with aggregation process, and with different surrounding medium.	14
Figure 4.1. UV-Visible spectrum of the hydroxylamine hydrochloride reduced AgNPs. ..	26
Figure 4.2. UV-Visible spectra of the citrate reduced AgNPs for seven months (a total of 29 spectra).	27
Figure 4.3. Zeta potential of citrate reduced AgNP colloid over seven months. Standard deviations are of three different measurements..	27
Figure 4.4. SERS spectra of citrate reduced AgNPs and hydroxylamine reduced AgNPs. 29	

Figure 4.5. A part of the deposition area of 0.4 μ M Cyt c-0.6 μ M Hb and AgNP mixture. SERS spectra were acquired from the encircled area.	31
Figure 4.6. Ten SERS spectra of each protein and their standard deviations (in black). . .	32
Figure 4.7. PCA plot of SERS spectra of eight proteins.	33
Figure 4.8. SERS spectra of the mixtures of Lys and apoTrf with different relative concentrations, and their PCA analysis.	34
Figure 4.9. SERS spectra of the mixtures of Cyt c and Hb with different relative concentrations, and their PCA analysis.	36
Figure 4.10. SERS spectra of the mixtures of HSA and Fb with different relative concentrations, and their PCA analysis.	38
Figure 4.11. SERS spectra of the mixtures of IgG and IgA with different relative concentrations, and their PCA analysis.	40
Figure 4.12. Plot of RMSECV results for different latent variable numbers.	41
Figure 4.13. Cross-validated PLS-DA classification results of the SERS spectra of eight proteins.....	42
Figure 4.14. RMSECV results of Lys and apoTrf mixtures as a function of the number of latent variable numbers.	43
Figure 4.15. Cross-validated PLS-DA classification results of the SERS spectra of the mixtures of Lys and apoTrf with different relative concentrations.	44
Figure 4.16. RMSECV results of Cyt c and Hb mixtures as a function of the number of latent variable numbers.	45

Figure 4.17. Cross-validated PLS-DA classification results of the SERS spectra of the mixtures of Cyt c and Hb with different relative concentrations.	46
Figure 4.18. RMSECV results of HSA and Fb mixtures as a function of the number of latent variable numbers.	47
Figure 4.19. Cross-validated PLS-DA classification results of the SERS spectra of the mixtures of HSA and Fb with different relative concentrations.	48
Figure 4.20. RMSECV results of IgG and IgA mixtures as a function of the number of latent variable numbers.	49
Figure 4.21. Cross-validated PLS-DA classification results of the SERS spectra of the mixtures of IgG and IgA with different relative concentrations.....	50
Figure 4.22. Raw SERS spectra of three dried droplets of whole serum samples with different AgNP concentrations (32x, 16x, 8x).	52
Figure 4.23. Raw SERS spectra of three dried droplets of whole serum samples with different AgNP concentrations (4x, 2x, 1x, 0.5x).....	53
Figure 4.24. Raw SERS spectra of three dried droplets of filtered serum samples with different AgNP concentrations (32x, 16x, 8x).	54
Figure 4.25. Raw SERS spectra of three dried droplets of filtered serum samples with different AgNP concentrations (4x, 2x, 1x, 0.5x).	55
Figure 4.26. Mapping the middle of dried droplets of mixtures of protein and AgNP colloid with different concentrations.	56
Figure 4.27. SERS spectra of serum after methanol extraction with different serum to methanol ratios (v/v).	57

Figure 4.28. Comparison of the SERS spectra of whole serum, filtered serum, and serum after methanol extraction.	57
Figure 4.29. SERS spectra of some molecules found in blood serum and SERS spectrum of AgNP.	59
Figure 4.30. SERS spectra of whole serum after spiking some molecules found in blood serum.....	60
Figure 4.31. Comparison of the SERS spectra of uric acid (Ur), hypoxanthine (Hx), and whole serum (WS) and filtered serum (FS) with different AgNP concentrations.	62
Figure 4.32. Changes in SERS spectrum of free serum (FS) when different concentrations of human serum albumin (HSA), transferrin, and lysozyme (Lys) are spiked.....	64
Figure 4.33. SERS spectra of uric acid in phosphate buffer (pH 12, without NaCl) with and without NaCl.	65
Figure 4.34. SERS spectra of uric acid in PBS at different pH values.	66
Figure 4.35. SERS spectra of uric acid in 10 mM borate buffer (pH 8.5) with and without NaCl.	66
Figure 4.36. SERS spectra of borate buffer at different borate concentrations.	67
Figure 4.37. SERS spectra of AgNPs in the presence of one percent NaCl and 50 mM borate buffer plus one percent NaCl..	67
Figure 4.38. SERS spectra of adenine, guanine and their mixtures at 8x and 32x AgNP concentrations.	68
Figure 4.39. SERS spectra of adenine, hypoxanthine and their mixtures at 8x and 32x AgNP concentrations.	69

Figure 4.40. SERS spectra of adenine, uric acid and their mixtures at 8x and 32x AgNP concentrations.	70
Figure 4.41. SERS spectra of adenine, xanthine and their mixtures at 8x and 32x AgNP concentrations.	70
Figure 4.42. SERS spectra of uric acid, guanine and their mixtures at 8x and 32x AgNP concentrations.	71
Figure 4.43. SERS spectra of guanine, xanthine and their mixtures at 8x and 32x AgNP concentrations.	71
Figure 4.44. SERS spectra of guanine, hypoxanthine and their mixtures at 8x and 32x AgNP concentrations.	72
Figure 4.45. SERS spectra of uric acid, hypoxanthine and their mixtures at 8x and 32x AgNP concentrations.	73
Figure 4.46. SERS spectra of xanthine, hypoxanthine and their mixtures at 8x and 32x AgNP concentrations.	73
Figure 4.47. SERS spectra of xanthine, uric acid and their mixtures at 8x and 32x AgNP concentrations.	74
Figure 4.48. Average SERS spectra of serum samples of cancer and chronic disease afflicted patients and healthy subjects obtained using 32x AgNP.	75
Figure 4.49. Box plots of the intensity values of the eight SERS bands.	77
Figure 4.50. PLS-DA scores plot of cancer and control group (32x AgNP).	78
Figure 4.51. ROC curve for cancer and control group (32x AgNP).	79

Figure 4.52. Permutation test of cancer vs. control groups (32x AgNP).	80
Figure 4.53. Frequency of window usage in models generated using genetic algorithms. Arrow indicates the used RMSECV value.	82
Figure 4.54. Shaded regions are the chosen shift regions with genetic algorithms (GA) for cancer vs. control study with 32x AgNP.	82
Figure 4.55. PLS-DA scores plot of cancer and control group (32x AgNP, with genetic algorithms (GA)).	83
Figure 4.56. ROC curve for cancer and control group (32x AgNP, with GA).	84
Figure 4.57. Permutation test of cancer vs. control groups (32x AgNP, with GA).	84
Figure 4.58. PLS-DA scores plot of chronic and cancer groups (32x AgNP).	85
Figure 4.59. ROC curve for chronic and cancer group (32x AgNP).	86
Figure 4.60. Permutation test of chronic vs. cancer groups (32x AgNP).	87
Figure 4.61. Shaded regions are the chosen shift regions with genetic algorithms (GA) for chronic vs. cancer study with 32x AgNP.	88
Figure 4.62. PLS-DA scores plot of chronic and cancer group (32x AgNP, with GA).	88
Figure 4.63. ROC curve for chronic and cancer group (32x AgNP, with GA).	89
Figure 4.64. Permutation test of chronic vs. cancer groups (32x AgNP, with GA).	90
Figure 4.65. PLS-DA scores plot of chronic and control groups (32x AgNP).	90
Figure 4.66. ROC curve for chronic and control group (32x AgNP).	91

Figure 4.67. Permutation test of chronic vs. control groups (32x AgNP).	92
Figure 4.68. Shaded regions are the chosen shift regions with genetic algorithms (GA) for chronic vs. control study with 32x AgNP.	92
Figure 4.69. PLS-DA scores plot of chronic and control group (32x AgNP, with GA). ...	93
Figure 4.70. ROC curve for chronic and control group (32x AgNP, with GA).	94
Figure 4.71. Permutation test of chronic vs. control groups (32x AgNP, with GA).	94
Figure 4.72. Average SERS spectra of serum samples of cancer and chronic disease afflicted patients and healthy subjects obtained using 8x AgNP.	96
Figure 4.73. The difference spectra of cancer group and control group obtained using 32x AgNP and 8x AgNP.	97
Figure 4.74. The difference spectra of chronic disease group and control group obtained using 32x AgNP and 8x AgNP.	97
Figure 4.75. PLS-DA scores plot of cancer and control group (8x AgNP).	98
Figure 4.76. ROC curve for cancer and control group (8x AgNP).	99
Figure 4.77. Permutation test of cancer vs. control groups (8x AgNP).	99
Figure 4.78. Shaded regions are the chosen shift regions with genetic algorithms (GA) for cancer vs. control study with 8x AgNP.	100
Figure 4.79. PLS-DA scores plot of cancer and control group (8x AgNP, with genetic algorithms (GA)).	101
Figure 4.80. ROC curve for cancer and control group (8x AgNP, with GA).	102

Figure 4.81. Permutation test of cancer vs. control groups (8x AgNP, with GA).	102
Figure 4.82. PLS-DA scores plot of chronic and cancer groups (8x AgNP).	103
Figure 4.83. ROC curve for chronic and cancer group (8x AgNP).	104
Figure 4.84. Permutation test of chronic vs. cancer groups (8x AgNP).	104
Figure 4.85. Shaded regions are the chosen shift regions with genetic algorithms (GA) for chronic vs. cancer study with 8x AgNP.	105
Figure 4.86. PLS-DA scores plot of chronic and cancer group (8x AgNP, with GA).	105
Figure 4.87. ROC curve for chronic and cancer group (8x AgNP, with GA).	106
Figure 4.88. Permutation test of chronic vs. cancer groups (8x AgNP, with GA).	107
Figure 4.89. PLS-DA scores plot of chronic and control groups (8x AgNP).	107
Figure 4.90. ROC curve for chronic and control group (8x AgNP).	108
Figure 4.91. Permutation test of chronic vs. control groups (8x AgNP).	109
Figure 4.92. Shaded regions are the chosen shift regions with genetic algorithms (GA) for chronic vs. control study with 8x AgNP..	109
Figure 4.93. PLS-DA scores plot of chronic and control group (8x AgNP, with GA). ...	110
Figure 4.94. ROC curve for chronic and control group (8x AgNP, with GA).	111
Figure 4.95. Permutation test of chronic vs. control groups (8x AgNP, with GA).	111

Figure 4.96. SERS spectra of serum samples of cancer patients before and after tumor removal. 112



LIST OF TABLES

Table 3.1. The list of chronic disease patients.	23
Table 3.2. The list of cancer patients. Blood samples after tumor removal were obtained from the patients with star symbol.	24
Table 4.1. Physicochemical properties of the proteins.	28
Table 4.2. Confusion table results for the PLS-DA cross validation model.	42
Table 4.3. Confusion table results for the PLS-DA cross validation model of Lys and apoTrf mixtures.	44
Table 4.4. Sensitivity and specificity results for classification of Lys and apoTrf mixtures.	45
Table 4.5. Confusion table results for the PLS-DA cross validation model of Cyt c and Hb mixtures.	46
Table 4.6. Sensitivity and specificity results for classification of Cyt c and Hb mixtures.	47
Table 4.7. Confusion table results for the PLS-DA cross validation model of HSA and Fb mixtures.	48
Table 4.8. Sensitivity and specificity results for classification of HSA and Fb mixtures.	49
Table 4.9. Confusion table results for the PLS-DA cross validation model of IgG and IgA mixtures.	50
Table 4.10. Sensitivity and specificity results for classification of IgG and IgA mixtures.	51

Table 4.11. Classification results of SERS spectra of the cancer and the control group obtained using 32x AgNP.	78
Table 4.12. Classification results of SERS spectra of the cancer and the control group obtained using 32x AgNP (with GA).	83
Table 4.13. Classification results of SERS spectra of the chronic and the cancer group obtained using 32x AgNP.	86
Table 4.14. Classification results of SERS spectra of the chronic and the cancer group obtained using 32x AgNP (GA).	89
Table 4.15. Classification results of SERS spectra of the chronic and the control group obtained using 32x AgNP.	91
Table 4.16. Classification results of SERS spectra of the chronic and the control group obtained using 32x AgNP (GA).	93
Table 4.17. Classification results of SERS spectra of the cancer and the control group obtained using 8x AgNP.	98
Table 4.18. Classification results of SERS spectra of the cancer and the control group obtained using 8x AgNP (GA).	101
Table 4.19. Classification results of SERS spectra of the chronic and the cancer group obtained using 8x AgNP.	103
Table 4.20. Classification results of SERS spectra of the chronic and the cancer group obtained using 8x AgNP (GA).	106
Table 4.21. Classification results of SERS spectra of the chronic and the control group obtained using 8x AgNP.	108

Table 4.22. Classification results of SERS spectra of the chronic and the control group obtained using 8x AgNP (GA).	110
--	-----



LIST OF SYMBOLS/ABBREVIATIONS

$^{\circ}\text{C}$	Degrees Celsius
cm^{-1}	Wavenumber
E_0	Amplitude of the wave
mg	Milligram
ml	Milliliter
mV	Millivolt
mW	Milliwatt
nm	Nanometer
α	Polarizability of a bond
μ	Dipole moment
μl	Microliter
μM	Micromolar
μm	Micrometer
a.u.	Arbitrary units
ApoTrf	Apotransferrin
AgNP	Silver nanoparticle
AUC	Area under curve
AuNP	Gold nanoparticle
CaF_2	Calcium fluoride
CCD	Charge-coupled device
CE	Chemical enhancement mechanism
CT	Computed tomography
Cyt c	Cytochrome c
DLS	Dynamic light scattering
DNA	Deoxyribonucleic acid
EDTA	Ethylenediaminetetraacetic acid
EM	Electromagnetic enhancement mechanism
Fb	Fibrinogen

FS	Filtered serum
GA	Genetic algorithms
Hb	Hemoglobin
HCA	Hierarchical cluster analysis
HSA	Human serum albumin
IgA	Immunoglobulin A
IgG	Immunoglobulin G
LDA	Linear discriminant analysis
LSP	Localized surface plasmon
LSPR	Localized surface plasmon resonance
Lys	Lysozyme
MRI	Magnetic resonance imaging
NaCl	Sodium chloride
NIR	Near infrared
NM	Nanomaterial
OH	Hydroxyl
PBS	Phosphate-buffered saline
PCA	Principal component analysis
PET	Positron emission tomography
Phe	Phenylalanine
pI	Isoelectric point
PLS-DA	Partial least squares-discriminant analysis
RMSECV	Root mean square errors of cross validation
ROC	Receiver operating characteristic
S.D.	Standard deviation
SERS	Surface-enhanced Raman scattering
Trp	Tryptophan
Tyr	Tyrosine
UV	Ultraviolet
UV-Vis	Ultraviolet-Visible
WS	Whole serum

1. INTRODUCTION

1.1. CANCER AND ITS DIAGNOSIS

Human body is composed of trillions of cells [1]. In general terms, cells come together and form tissues, and tissues form organs. All organs and tissues work in an ordered and synchronized fashion in the human body. Cells grow by dividing. One cell divides into two cells, two cells become four cells and so on. Cells divide not only for baby growing in his/her mother's womb or during growing of a baby to be a child and an adult, but also to replace older damaged cells. Normal cells divide in a controlled way just when they need to. Cancerous cells, on the other hand, divide uncontrollably. These cells start to divide and keep dividing. The rapidly dividing cells push aside the healthy cells around them, and form a small cancer. At first, this small cancer is small to see, and then it begins to grow beyond the organ where it started.

Cells divide when their genes tell them to, but if a gene has a mutation, it can tell a cell to divide when there is no reason for it to divide. Most cancers start because of mutations in several different genes [2]. DNA repair systems in cells try to recover functionality of the genes but can not be always successful in their jobs; therefore proteins may not be produced using those genes or produced proteins may become unfunctional. Missing of proteins and presence of unfunctional proteins breaks up the harmony inside the cells. Other things which can change functionality of genes other than changing the structure of a gene are some epigenetic modifications such as methylation, acetylation, phosphorylation and ribosylation [3]. Regional inversions, deletions, and insertions of DNA sequences, and some chromosomal rearrangements may be the other causes [4].

The three major gene classes which are responsible for cancer are oncogenes, tumor suppressor genes, and DNA repair genes [5]. In cancerous cells, proto-oncogenes become oncogenes due to the factors mentioned above. Some widely known examples of oncogenes are the genes called RAS, MYC, and Erk [6]. Tumor suppressor genes check cell dividing and proliferation, start DNA repair events in the case of any DNA damage, and trigger apoptosis when DNA repair tries are unsuccessful. The most widely known example of

them is TP53 gene [7]. Deletions, point mutations, epigenetic silencing, improper separation of chromosomes, and mitotic recombinations make tumor suppressor genes functional, leading to carcinogenesis [1, 7]. DNA repair genes attract the proteins which repairs damaged DNA sequences [8]. In the case of DNA repair failure, they lead cells to apoptosis or necrosis. When these genes are unfunctional, carcinogenesis may occur. One of the best known DNA repair genes is BRCA gene [9]. Any mutation in these BRCA gene increases the risk of breast cancer.

Genetic disorder and liabilities are not the sole causes of cancer [10]. The use of tobacco and products derived from tobacco, and alcohol, exposure to ionizing radiation, UV radiation, air pollution, and chemical carcinogens in environment, dietary habits, viruses etc. increases humans' risk to have cancer disease.

The most prevalent cancer type in the world is lung cancer [11]. For males, lung cancer is the most observed and death causing one, followed by prostate cancer and colorectal cancer (for incidence) and liver and stomach cancer (for mortality). For women is breast cancer is the most observed and death causing one, followed by colorectal and lung cancer (for incidence). In the case of mortality, lung cancer is the second, colorectal is the third prevalent one.

Today, cancer diagnosis is achieved using different types of tests and imaging techniques [12-15]. After initial evaluation of a clinician, different combinations of test and imaging techniques are used for specific symptoms. Tests involve biopsy followed by histopathological examination and some blood tests. Imaging techniques are used to locate tumor tissue and its size if there any. The general steps and methods for diagnosis are the followings:

Biopsy and histopathological evaluation: Biopsy is the removal of a tissue to analyze in a laboratory. There are different biopsy techniques specific for different regions of the body. In a laboratory, samples are chemically treated and/or sectioned, and examined under microscope. Cancer grade can also be determined. With this method, results may be available after a few days, and sometimes diagnosis can be done inaccurately.

Imaging techniques: Using imaging techniques, clinicians can examine patient's body, locate tumor tissue, and determine its size and stage. Which kind of technique to be used is determined by body part to be examined and type of cancer to be detected. Magnetic resonance imaging (MRI), computed tomography (CT), x-ray imaging, positron emission tomography (PET), ultrasound, colonoscopy, and endoscopy are the major techniques for cancer screening and diagnosis. Besides the advantages of each imaging techniques, cost (expensive instrumentation) and some resolution limitations can be stated as disadvantages of these conventionally used imaging techniques.

Blood tests: Blood samples are taken from patients, and analyzed in a laboratory. Composition of the samples based on cell type, cell count are analyzed (for example a leukemia cell, a circulating tumor cell can be found among many other cells), and some biomolecules which can be clue about the presence of a cancer are screened. Three types of blood tests are the followings:

- **Complete blood count:** This frequently used test counts the amount of different types of cells in a blood sample. If the amount of certain types of cells are present in very low amount or in a very high amount , or if abnormal cell are detected, then different types of blood cancers can be identified (for example, leukemia, lymphoma, and myeloma). Bone marrow biopsy is helpful after this test for further confirmation of the diagnosis.
- **Blood protein test:** Electrophoresis technique is used to separate and examine blood proteins. For example, in the case of multiple myeloma, detection of certain immunoglobulins may be helpful for diagnosis. Bone marrow biopsy is helpful after this test for further confirmation of the diagnosis.
- **Tumor marker tests:** Tumor markers are specific biomolecules which are produced by cancerous cells. If they are detected in blood, it can be helpful for diagnosis of different cancer types. Examples are alpha-fetoprotein for liver cancer, prostate specific antigen for prostate cancer. The amount of tumor markers can increase in some other conditions other than cancer. This restricts the use of tumor markers for a better diagnosis.

- Circulating tumor cells: Some cancerous cells from tumor tissues may pass to blood stream. Detection of these cells are used for diagnosis.

Although some blood tests are very useful for certain cancer types of which specific tumor marker and/or protein, markers of many other cancer types are not yet discovered; therefore these tests may not be useful in many situations. Cell counting methods are costly and time consuming.

As the state of technology evolves in time, researchers all over the world work for yielding better efficiency of the conventional methods and techniques, and try to lower their cost for community. Meanwhile, different techniques which have been used in different areas (i.e., other than clinics) have been tried to be incorporated into the clinics as an alternative method, and one of them is Raman spectroscopy.

1.2. RAMAN SPECTROSCOPY

1.2.1. Raman Scattering

As well known, in the last a few decades of the 19th century and the first decades of the 20th century, the world welcomed many breakthroughs in the field of physics. One of the main contributors to the field was John William Strutt (Lord Rayleigh). He discovered the physical explanations of why the sky is blue [16-18]. He observed that molecules in the atmosphere scatter the incident sunlight. This type of scattering is now called as Rayleigh scattering. Photons in sun light having a size of 400-700 nm (i.e., visible portion of the sun light) scatters over very small particles like oxygen and nitrogen molecules (~300 picometer). Since photons have much bigger size than the molecules (about 1000 times more), scattering of photons over molecules cannot be interpreted as a result of actual collisions. When photons (i.e., electromagnetic wave) come along and interact with molecules, they change the electromagnetic field around these molecules. Protons and electrons of the molecules partially separate and form “dipoles”. Since photons oscillate at a certain frequency, they also make dipoles start to oscillate at the same frequency. During these oscillations, dipoles emit their own photons which have the same frequency of the dipole creating incident photons. This means that in Rayleigh scattering, energy of the

photons is preserved, and as an analogy to Newtonian mechanics it is called as elastic scattering.

Lord Rayleigh analyzed the blue sky phenomenon using James Clerk Maxwell's equations for the electromagnetic field in detail; he found that intensity of scattered radiation varies inversely with the fourth power of the wavelength [19, 20]. This meant that shorter blue wavelengths of the sun light would be scattered more efficiently than the longer red wavelengths of the sun light. Rayleigh also interpreted the color of sea as the reflection of the color of the sky.

After three years of Rayleigh's death, in 1922, another brilliant young scientist, Chandrasekhara Venkata Raman, reported that sea was also scattering the light [21]. After that Raman started investigating the light scattering phenomenon more intensively with his colleagues in Calcutta, India.

In 1923, Arthur Compton showed that scattered X-rays from electrons of a carbon sample had longer wavelengths than those targeted onto the sample [22]. In his experiments, both electrons and scattering X-rays went separate ways upon collision while scattering X-rays had longer wavelengths (e.g., a ball "A" hits another ball "B", and incoming ball goes in a different direction while losing its energy). Compton thought that this was due to conservation of energy and momentum, and photons may be considered as particles. This was the first demonstration of inelastic scattering. In 1927, Compton was awarded with the Nobel Prize in Physics for this discovery.

Meanwhile Raman was studying on the nature of light scattering on various media such as liquids, gases, and crystals, and trying to understand the nature of so called "secondary radiations", and their difference from fluorescence. Findings might be due to fluorescence due to impurities in liquid chemicals, therefore they further purified chemicals to avoid fluorescence contribution in his experiments. What he found that the secondary radiation (the scattering light through liquids upon illumination with sunlight) was polarizing. It was very important because most of the fluorescence was unpolarised radiations. On the other hand, power of light was not sufficient for obtain higher efficiencies in his experiments; therefore this new type of scattering could be observable only on a few liquids. After Compton's findings, he thought that his and his colleague's findings might be analogous to

that of Compton's. That time, he used optic parts of a telescope to be able to obtain stronger sunlight for his studies on scattering, and purified the liquids by repeated distillation in vacuum environment. He used around 80 different liquids to prove universality of the new type of scattering. Later, he used monochromatic light source for further experiments. For each liquid, on spectrograms, he observed additional lines present on the right side of the lines occurred due to incident light, meaning that those additional lines had longer wavelengths. Findings of these experiments were published in the journal *Nature* having a title "A new type of secondary radiation" on 31st March 1928 [23]. This new type of scattering is now called as Raman scattering. C.V. Raman received a Nobel Prize in 1930 for his valuable contributions to the field of physics.

Rayleigh and Raman scattering can be explained further on a Jablonski diagram (Figure 1.1). Scattering can be thought of as a two photon process. During Rayleigh scattering process, the molecule which absorbs photon cannot reach an excited electronic, therefore the state where the molecule reaches is called virtual state. Then, the energy level of the molecule comes back down to the initial ground state while emitting the absorbed energy. Therefore the energy of the emitted photon (therefore also its wavelength) is equal to the energy of the incident photon. During Raman scattering, the molecule reaches a virtual state, and then comes back to a final state which is different than the initial state. Therefore, the frequency and the energy of the emitted photon become different than the incident photon. If the scattered photon possesses less energy than the incident photon, this type of scattering is called Stokes scattering (Figure 1.1). If the inverse happens, then it is called anti-Stokes scattering. In a scattering event, Rayleigh scattering comprises more than 99.9 percent of total scatterings. The other two comprise extremely small portion ($\sim 10^{-7}$) of scattered photons. Molecules have a stronger tendency to be at ground state energy level at room temperature, therefore intensity of Stokes scattering is more intense than anti-Stokes scattering.

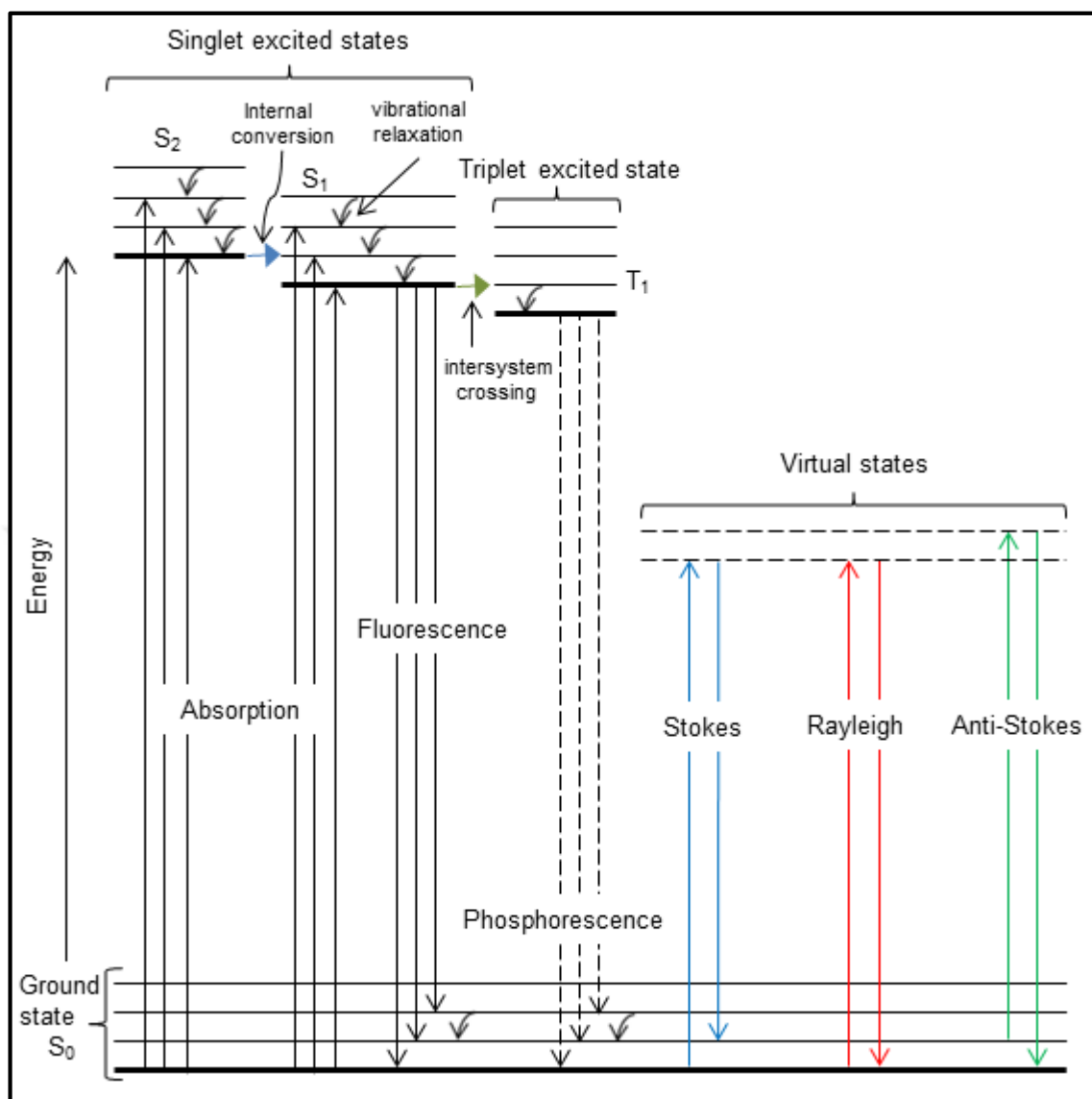


Figure 1.1. Jablonski diagram of energy transitions for absorption, fluorescence, phosphorescence, Rayleigh scattering, and Raman scattering (Stokes scattering and Anti-Stokes scattering).

Stokes and Anti-Stokes scattering are presented in Raman spectrum plots as Raman shift values, which are shown in terms of wavenumbers rather than wavelength values. Wavenumber of a Raman shift value is found using the following equation:

$$Raman\ shift\ (cm^{-1}) = \left(\frac{1}{\lambda_{incident\ light}} - \frac{1}{\lambda_{scattered\ light}} \right) \times 10^7 \quad (1.1)$$

According to the equation, wavenumber values for Stokes scattering are positive values, because their wavelengths are longer than the incident light. On the other hand, for Anti-Stokes scattering, wavenumber values are negative. Figure 1.2 shows a typical Raman spectrum plot. The intensity values of the Raman bands are shown in arbitrary units. To be able to obtain spectrum of both types of scattering, notch filters must be used on the instrument (it removes only Rayleigh scattering). If edge filters are used, only Stokes shifts can be obtained. For the study of biological structures, Stokes shifts are generally used for Raman spectrum plots.

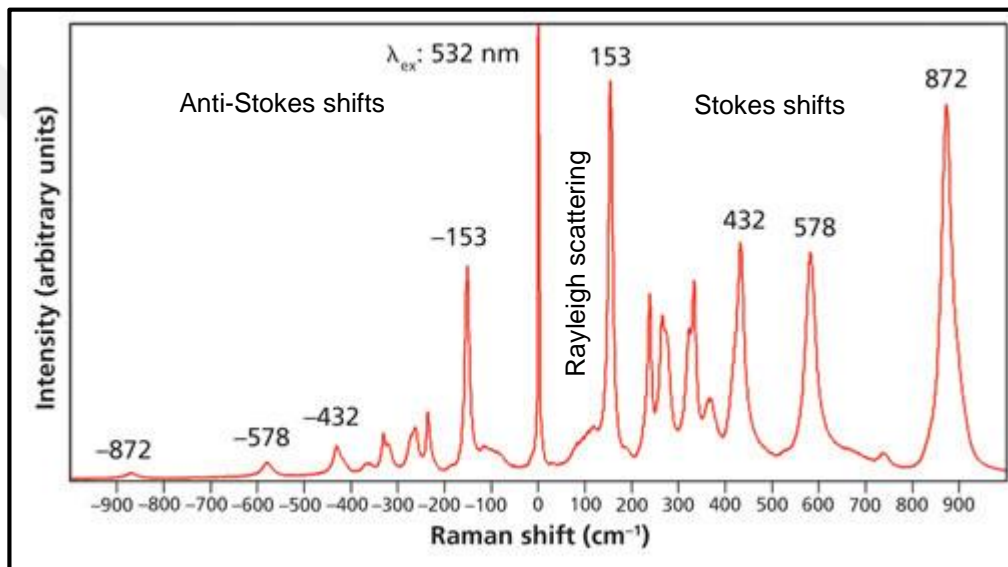


Figure 1.2. Raman spectrum of a LiNbO₃ single crystal [24].

Raman spectroscopy is an extremely useful tool for various types of researches, because Raman bands give information on many levels about the analytes (Figure 1.3). Chemical bonds possess different vibrational modes and vibrational energy levels, and each scatters the light with different energies. Therefore, in a Raman spectrum, each bond of the molecule demonstrates itself as a distinct Raman band. Since different molecules possess different types of bonds and different combinations of types of bonds, their Raman spectra become unique to them, providing a “fingerprint” information for molecules. Frequency changes of Raman bands are useful for assessment of stress and strain on samples. The use of polarised Raman is useful for symmetry and orientation of crystals. The change of the

width of a Raman band may give hints about deformation of analyte. Quantitative analyses can also be performed using intensity changes of Raman bands.

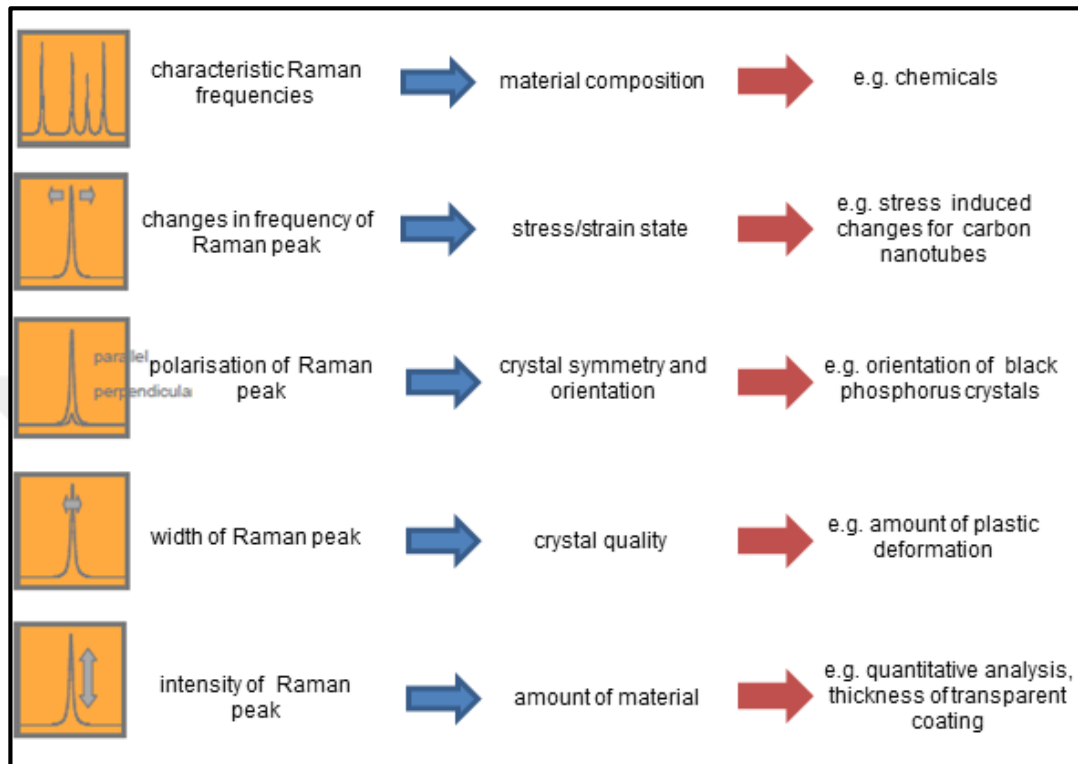


Figure 1.3. Information obtained from a Raman spectrum.

1.2.2. Basic Theory of Raman Scattering

Electric field is a vector quantity having an amplitude part and a phase part can be defined as in Equation 1.2

$$\vec{E} = E_0 \cos(2\pi \nu_0 t) \quad (1.2)$$

where E_0 is amplitude of the wave, ν_0 is the frequency of the incident light beam. When an electric field is applied to a molecule, it will try to push the plus charges towards its direction and the electron cloud goes to the opposite direction of that electric field [25]. This creates a dipole configuration. Dipole moment is defined as the product of the charge q and the separation distance d between these two charge centers.

$$\mu = qxd \quad (1.3)$$

Dipole moment μ for the molecule is also proportional to the applied electric field \vec{E} . Therefore, Equation 1.3 can be written as Equation 1.4

$$\mu = \alpha E \quad (1.4)$$

where α defines polarizability of a bond in the presence of an electric field. By combining Equation 1.2 with 1.4, we find

$$\mu = \alpha E_0 \cos(2\pi \nu_0 t) \quad (1.5)$$

In the absence of an electric field, a molecule vibrates at its own vibrational frequencies. On the other hand, in the presence of an electric field, oscillations of the induced dipole moment are amplitude modulated at the frequency ν_{vib} of the molecular vibration, which depends on polarisability changes of the molecular bonds (Figure 1.4).

Polarisability changes as a function of the distance r between the vibrating atomic nuclei. Therefore, polarisability can be also written as

$$\alpha = \alpha_0 + \frac{\partial \alpha}{\partial r} (r - r_{eq}) \quad (1.6)$$

where α_0 is the polarisability when distance between nuclei at equilibrium was at the equilibrium distance r_{eq} . Distance r is the distance between nuclei at any time (which means that it is time dependent). Hence, the change of the internuclei distance can be written as

$$r - r_{eq} = r_m \cos(2\pi \nu_{vib} t) \quad (1.7)$$

where r_m is the maximum distance between nuclei relative to equilibrium position. By combining Equation 1.6 with 1.7, we find

$$\alpha = \alpha_0 + \frac{\partial \alpha}{\partial r} r_m \cos(2\pi \nu_{vib} t) \quad (1.8)$$

When Equation 1.8 and 1.5 is combined and rewritten using trigonometric rule $\cos a \cos b = \frac{1}{2}[\cos(a + b) + \cos(a - b)]$, we find

$$\begin{aligned} \mu = & \alpha E_0 \cos(2\pi \nu_0 t) + \left(\frac{E_0}{2}\right) r_m \left(\frac{\partial \alpha}{\partial r}\right) \cos[2\pi(\nu_0 - \nu_{vib})t] \\ & + \left(\frac{E_0}{2}\right) r_m \left(\frac{\partial \alpha}{\partial r}\right) \cos[2\pi(\nu_0 + \nu_{vib})t] \end{aligned} \quad (1.9)$$

where first part of the Equation 1.9 is of Rayleigh scattering, and the second part corresponds to Stokes scattering, and the third part correspond to and anti-Stokes Raman scattering. According to the equation, Raman scattering occurs when polarizability changes as a function of r (distance between nuclei) and $(\partial \alpha / \partial r)$ has a non-zero value during a vibration.

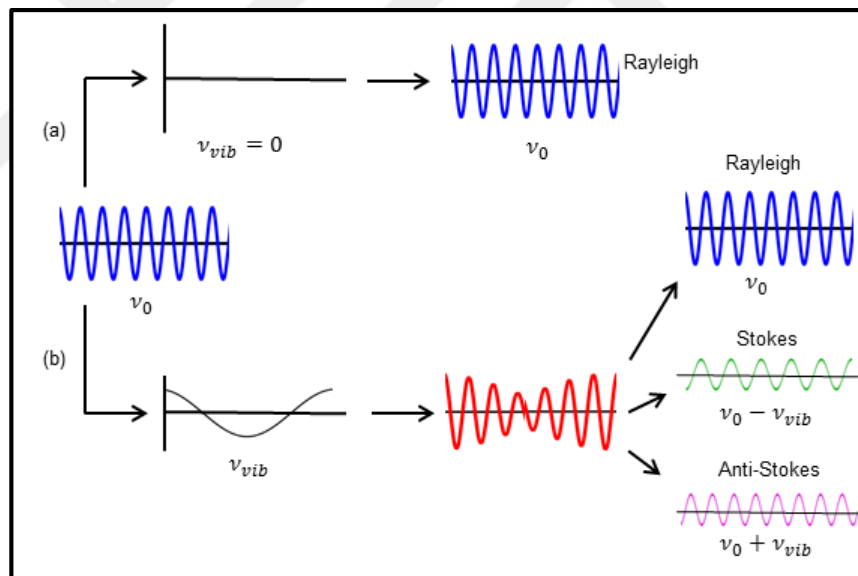


Figure 1.4. (a) When molecule does not vibrate, oscillation frequency ν_0 of the induced dipole is equal to the frequency of the incident light; (b) When molecule vibrates with a frequency ν_{vib} , the electric dipole is modulated by the molecule, and total induced electric dipole is resolvable into three frequency components.

1.2.3. Raman Instrument

A Raman instrument (Figure 5 and 6) consists of lasers as excitation sources (Figure 6), beam steers (mirrors) for adjustment of laser path, filters appropriate for each laser wavelengths for Rayleigh scattering removal, slit for removing unwanted light and intensifying the Raman scattering, grating, CCD detector, microscope, and a stage for sample handling.

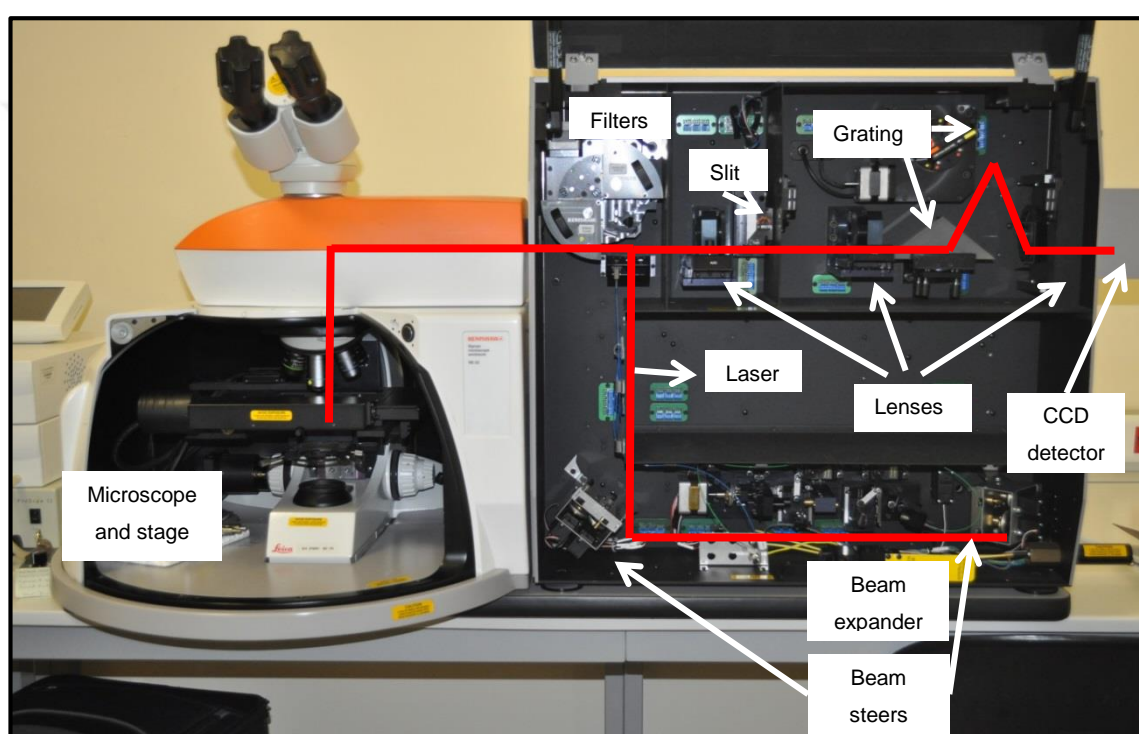


Figure 1.5. Components of a Raman instrument.

The choice of laser wavelength depends on the sample to be analyzed. 244 nm lasers are generally used for biological studies because some molecules such as DNA, protein, and some amino acids absorb UV light. 325 nm lasers are used for studies on wide band gap semiconductors. 488 nm, 514 nm, 633 nm and 785 nm lasers are used for various fields such as catalysis, semiconductor studies, and researches on polymers, minerals and biological structures. 830 nm laser is mainly used for biological studies. Near infrared (NIR) lasers (785 and 830 nm) are better for biological researches because photodegradation of samples and fluorescence issues can be avoided.

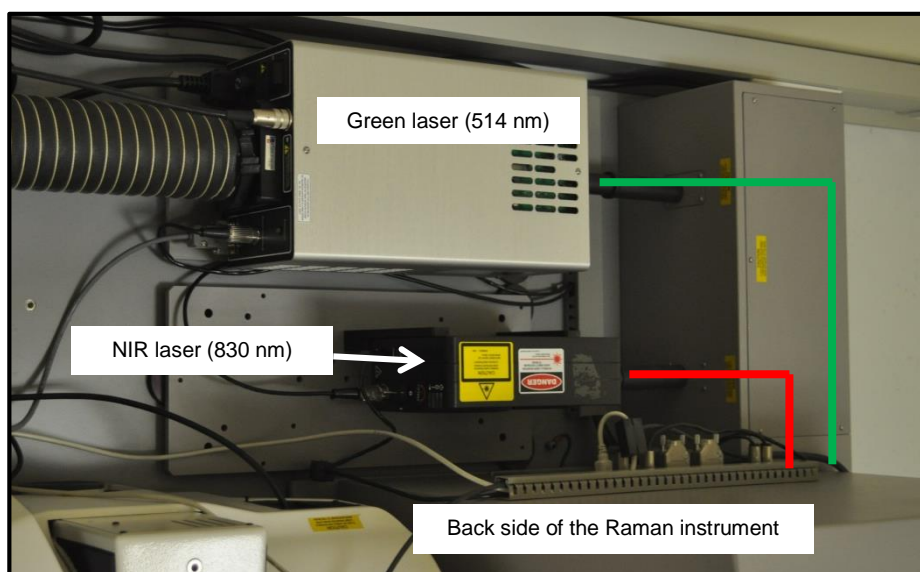


Figure 1.6. Lasers of a Raman instrument

1.2.4. Plasmonics

Plasmon word comes from unification of the Greek word “plasma” and “mons”. Plasma means molded or shaped, and mons means a mountain or body. In physics, the model of a conductor is an array of metallic ions surrounded by a sea of electrons, which is called “free electron gas”. Plasmon is a quasi-particle that can be described by a collection of interacting particles and conduction electrons make up the free electron gas [26]. In other terms, electron gas around nanoparticles oscillates collectively and a plasmon phenomenon occurs around them. When these plasmons occurs at the interface between metal and dielectric surface, it is called “surface plasmons” [27]. There are two types of surface plasmons: propagating ones and non-propagating ones. The latter one is called “localized surface plasmon” (LSP) and occurs around nanometer sized noble metals due to confinement of plasmons [28]. The wavelengths of light is much larger than the size of a nanoparticle. When light interacts with a nanoparticle, the external electric field of light creates a distortion in the electron cloud that makes up surface plasmons. If nanoparticles are excited at a resonant frequency, the absorption of light and the response of the nanoparticles become very strong, and this time it is called “localized surface plasmon resonance” (LSPR) (Figure 1.7). The light wavelength at which LSPR occurs depends on

size and shape of nanoparticles, aggregation state of nanoparticles, and refractive index of the environment surrounding the nanoparticles (Figure 1.8) [29, 30].

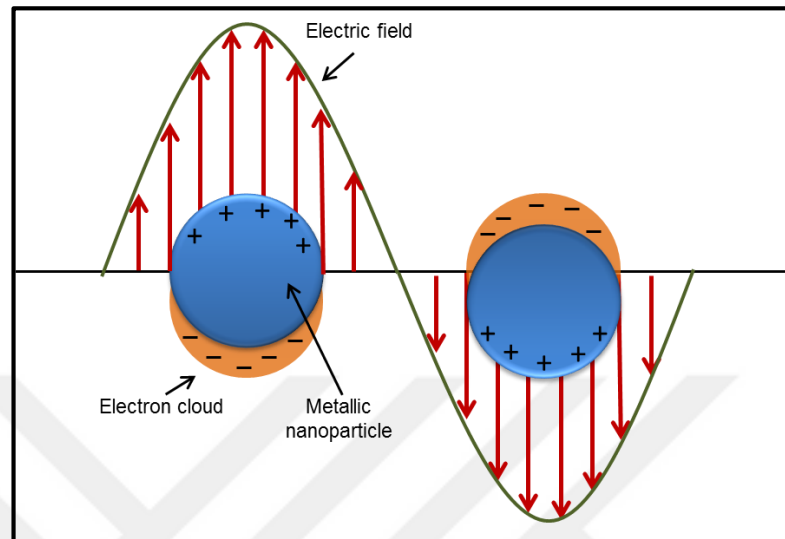


Figure 1.7. Illustration of localized surface plasmon resonance.

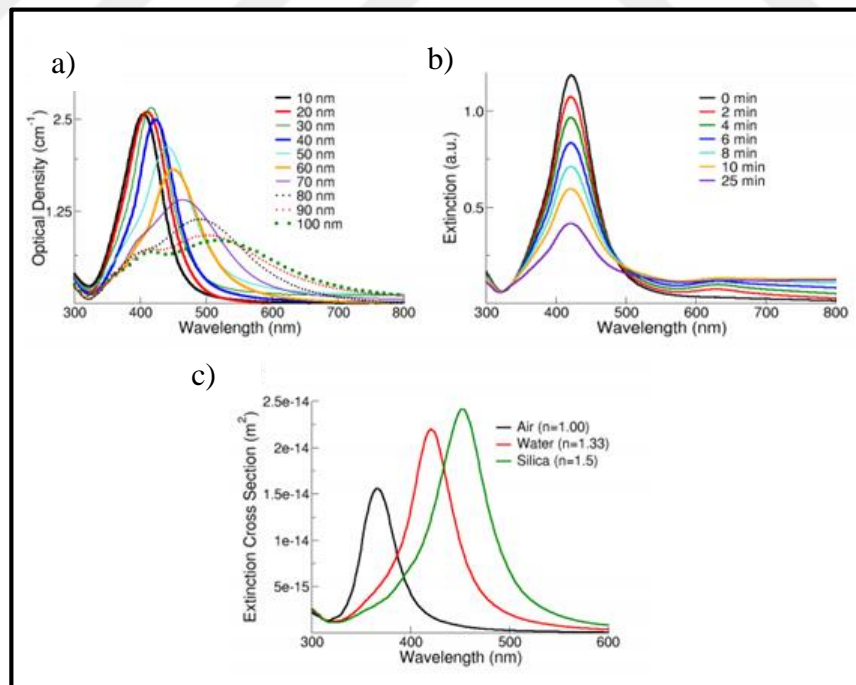


Figure 1.8. (a) The UV-Vis spectra of AgNPs with different sizes. (b) The change of the UV-Vis spectrum of colloidal 50 nm sized AgNPs during their aggregation process. (c) The effects of surrounding medium of 50 nm sized AgNPs on their UV-Vis spectrum [30].

1.2.5. Surface-Enhanced Raman Scattering

Surface-enhanced Raman scattering (SERS) can be defined as the much more enhanced Raman scattering from molecules when they are either adsorbed on or be in close vicinity of noble metal nanoparticles such as gold nanoparticles (AuNP) and silver nanoparticles (AgNP) [31]. This type of enhanced Raman scattering was found firstly in 1974 by Fleischmann *et al.* while studying Raman scattering of pyridine on roughened silver electrode surfaces [32]. Three years later, in 1977, Van Duyne and his graduate student Jeanmaire found that the reason for 10^5 - 10^6 times enhanced Raman signals might not only be surface roughness, and stated that there must have been other things which caused enhanced Raman scattering, and electric field enhancement could be the reason for this phenomenon [33]. In the same year, a separate group of Albrecht and Creighton reported “Anomalously Intense Raman Spectra of Pyridine at a Silver Electrode” [34]. They proposed that enhanced Raman signal was due to a charge transfer between surface and adsorbed pyridine molecules, resulting in resonance Raman scattering. This finding is now accepted as “chemical enhancement theory of SERS”. After these findings, Van Duyne met and discussed with physicists, learned from them more about surface plasmons, and developed “electromagnetic field enhancement theory of SERS” [35]. Later, other reports on this new type of scattering further revealed the effects of surface plasmons [36-39]. Today, both chemical enhancement theory and electromagnetic theory are accepted as the contributors of SERS theory.

As it was discussed in the previous section that a localized surface plasmon resonance occurs on noble metal nanoparticle surfaces in the presence of an electromagnetic field. When Raman scattering molecules come nearby of these nanoparticles, their induced dipole moments increase, therefore the amount of Raman scattering from that molecule increase. The highest enhancements occurs when molecules are present between adjacent nanoparticles due to a “hot spot” formation between adjacent nanoparticles (i.e., when the distance between nanoparticles is less than 4 nanometer) [40, 41]. Generally, in a SERS experiment, more than 25 percent of total enhancement (in many cases more than 50 percent) are obtained from the molecules in the hot spots, although total surface area of the hot spots are less one percent of the total surface of the nanoparticles interacting with a

light source [42, 43]. This extreme intensity increase in hot spots even makes single molecule detection possible [44-46].

The major parameters in a SERS experiment are laser wavelength, SERS substrate type (i.e., colloidal AgNPs, AuNPs or solid substrates), size, shape, and surface chemistry of nanoparticles, and aggregation status of nanoparticles. All these parameters are interconnected. Intensity of the SERS bands may differ with the wavelength of laser. Some laser wavelengths may be more suitable for some molecules. Especially, fluorescence may be a problem with visible wavelengths while dealing with biological molecules. The use of a near infrared (NIR) laser overcomes this problem. Size and shape of nanoparticles effect surface plasmon formation. Surface chemistry defines interaction of the molecules with nanoparticle surface. For example, positively charged molecules can interact better with a negatively charged nanoparticle than negatively charged molecules. In addition, the molecules possessing certain functional groups such as amines and thiols can bind easily to noble metal nanoparticle surfaces. Molecule orientation on the nanoparticle surface also effects the shape of obtained spectra, because the Raman scattering of the chemical bonds which are the nearest to the nanoparticle surface is more enhanced. Aggregation status of nanoparticles is directly linked to hot spot formation. More aggregated colloidal nanoparticles may produce more hot spots, hence produce higher SERS signals. On the other hand, direction of accumulation of nanoparticles during aggregation should be perpendicular to impinging laser [47]. Direction of hot spot formation and chaotic nature of aggregation can be resolved by using solid SERS substrates. On the other hand, production of these type of substrates are costly and time consuming. In addition, since they are contaminated within an experiment, they are not reusable. As seen, there are always trade-offs among different options, therefore a SERS experimenter must chose a proper laser wavelength and substrate for his/her “specific experiment”.

During last two decades, surface-enhanced Raman scattering has been used for various types of studies. In literature, lots of articles are reported about SERS studies on detection, identification, imaging of biological molecules [48-57], microorganisms [58-64], viruses [65-69], cells [70-76], and tissues [77-84]. Providing fingerprint of molecules with much more enhanced Raman scattering, SERS technique will be continue to be a valuable tool for biological studies, and even for clinics for routine analysis.

1.2.6. A Review of Current Literature on Label-Free Cancer Detection Based on Blood plasma and Serum SERS

First report about the use of label-free SERS for cancer detection was of Feng *et al* [85]. They collected plasma samples of 43 Nasopharyngeal cancer patients and of 33 healthy volunteers. Concentrated hydroxylamine reduced AgNPs (H-AgNPs) were mixed with plasma samples at a 1:1 proportion. After two hours of incubation at four °C, a drop of the mixture was spotted on an aluminum plate and spectra were collected using a 785 nm laser. Principal component analysis (PCA) and linear discriminant analysis (LDA) were used for analysis of the acquired spectra. Sensitivity of the diagnostic analysis was 90.7 percent, with a specificity of 100 percent. Overall accuracy was 95.4 percent. Spectral patterns of two groups were also compared. Intensity values of the SERS peaks at 725, 1330, 1445 and 1580 cm^{-1} were higher in the SERS spectra of cancer plasma samples. On the other hand, intensity values of 494, 589, 638, 813, 1004 and 1134 cm^{-1} were higher in the SERS spectra of healthy plasma samples.

Feng *et al.* studied gastric cancer detection using SERS and evaluated effects of the polarized laser light on detection [86]. SERS spectra of plasma samples of 32 gastric cancer patients and of 33 healthy individuals were acquired using concentrated H-AgNPs as SERS substrates and a 785 nm laser. Before acquisition plasma and AgNP colloid mixture waited for two hours. Principal component analysis (PCA) and linear discriminant analysis (LDA) were used for analysis of the acquired spectra. One hundred percent diagnostic sensitivity and 97 percent specificity were achieved when left-handed circularly polarized laser was used. Sensitivity and specificity values were less than these values when non-polarized laser, linear-polarized laser, right-handed circularly polarized laser were used. Although authors did not give a satisfactory explanation for this results. They concluded that the differences of the chiral properties of the molecules in plasma samples were shown up well with left-handed circularly polarized laser.

Lin *et al.* studied colorectal cancer detection [87]. SERS spectra of serum samples of 38 colorectal cancer patients and of 45 healthy individuals were acquired using citrate reduced AuNPs (cit-AuNP) as SERS substrates and a 785 nm laser. Before acquisition serum and AuNP colloid mixture waited for two hours. Two different analyses for discrimination

purposes were performed. First, ratio of the SERS intensity of 725 cm^{-1} and 638 cm^{-1} bands for each spectrum were compared. They stated that 725 cm^{-1} band was stemming from adenine and 638 cm^{-1} band was stemming from tyrosine. A sensitivity of 68.4 percent and a specificity of 95.6 percent were attained. After that, using PCA-LDA analysis for the entire spectra a sensitivity of 97.4 percent and a specificity of 100 percent were attained.

Duo Lin *et al.* studied differentiation of different stages of nasopharyngeal cancer [88]. They used citrate reduced AuNPs as SERS substrates. After simple mixing with plasma of 60 healthy people, 25 nasopharyngeal cancer (at T1 stage), and 75 nasopharyngeal cancer patients (T2-T4 stage), they collected their SERS spectra and analyzed using PCA-LDA. Accuracy for differentiation of T1 stage samples from control samples was 83.5 percent and for differentiation of T2-T4 stage samples from control samples was 93.3 percent. Sixty three percent accuracy was obtained when T1 samples were differentiated from T2-T4 samples.

Xiaozhou Li *et al.* collected SERS spectra of 23 healthy people and 22 esophageal cancer patient before operation and three months after operation [89]. SERS spectra were acquired after direct mixing serum samples with citrate reduced AgNPs. Both PCA and hierarchical cluster analysis (HCA) were used for discrimination of the collected spectra. Seventy seven percent accuracy of discrimination was obtained with HCA analysis. The use of PCA resulted in 89.6 percent accuracy. They also observed that spectra of the post-operative serum samples more similar to that of control group than pre-operative serum samples. They concluded that SERS could also be used efficiency of cancer treatment.

Some other serum or plasma based SERS studies have been also reported in literature such as discrimination of prostate cancer [90], myeloma [91], cervical cancer [92], breast cancer [93, 94].

Bonifacio *et al.* analyzed SERS spectra of blood plasma and serum using both AuNP and AgNP colloids [95]. In their study, they acquired SERS spectra of the samples while they are in liquid form. They showed that the use of Li-heparin containing collection tubes for plasma SERS studies results in more reproducible spectra than the use of EDTA or citrate containing collection tubes. The presence of protein parts suppressed the SERS signal of other metabolites and cause less reproducible spectra; therefore they stated that the use of

filtered serum would be more appropriate. Three different laser wavelengths (785 nm, 633 nm, and 514 nm) were compared for maximum signal intensity and spectral reproducibility, and found that 785 nm was the best for serum SERS studies. Moreover, they compared SERS spectra of uric acid and hypoxanthine with serum spectra, and demonstrated that some SERS bands of serum spectra could be due to uric acid and hypoxanthine.



2. AIM OF THE STUDY

Utilization of label-free SERS of blood serum for cancer diagnosis is newly growing and promising approach. If this is achieved, different types of cancers can be diagnosed by simply using a few microliters of serum and SERS substrate, and a Raman instrument (either with a benchtop one or a hand held one). In order to realize this, several points must have been understood first. Blood serum is a extremely complex liquid consisting of various types of proteins and biomolecules. Therefore a stepwise study have been needed to understand the origins of the SERS bands before cancer diagnosis and identification studies using SERS. For this aim,

- SERS study of some blood proteins had to be performed to understand SERS spectra of proteins. As a model, SERS spectra of binary mixtures of different blood proteins were analyzed. The effects of protein size on the final shape of the SERS spectra of the mixtures.were discussed and discrimination of each protein in the mixtures were tried using different statistical methods.
- SERS spectrum of filtered and unfiltered blood serum were compared. The effects of addition of proteins to filtered serum on its SERS spectra were demonstrated.
- The effects of concentration of SERS substrate (AgNP colloid) on serum SERS spectra were analyzed and the effects of certain molecules on serum SERS spectra were studied.
- SERS spectra of some purines and purine derivatives and their mixtures were studied to obtain deeper understanding about serum SERS spectra.

After these studies, discrimination of serum samples of cancer patients from samples collected from healthy donors and patients with chronic diseases was performed.

Lastly, the effects of tumor removal from cancer patients on the SERS spectra of their serum was demonstrated.

3. MATERIALS AND METHODS

3.1. CHEMICALS AND MATERIALS

Human serum albumin, hemoglobin, apotransferrin, immunoglobulin G, immunoglobulin A, cytochrome c, lysozyme, fibrinogen, silver nitrate, sodium hydroxide, sodium citrate, methanol, arginine proline, serine, valine, histidine, tryptophan, tyrosine, phenylalanine, urea, mannose, thymine, cytosine, guanine, xanthine, hypoxanthine, adenine, uric acid, commercial human serum, sodium phosphate dibasic, sodium phosphate monobasic, boric acid, phosphate buffered saline (PBS) were purchased from Sigma-Aldrich (Germany). Hydroxylamine hydrochloride and Amicon 3 kDa 15 ml centrifugal filtration tubes were purchased from Merck (Germany). Aqueous solutions were prepared using double distilled, deionized water from Millipore DirectQ-ultraviolet (UV) system.

3.2. SILVER NANOPARTICLE SYNTHESIS

Citrate reduced silver nanoparticles (AgNPs) were synthesized using Lee-Miesel method [96]. One hundred and eighty mg of silver nitrate was added into one liter of distilled water and stirred until boiling. Then, 20 ml of one percent (w/v) trisodium citrate solution added dropwise, and kept boiling for another one and half hour. After cooling, loss of water due to evaporation was compensated by adding water to make it one liter of colloidal AgNP suspension.

Hydroxylamine reduced AgNPs were synthesized using Leopold-Lend method [97]. Ten ml of hydroxylamine hydrochloride (1.5×10^{-2} M) and sodium hydroxide (3×10^{-2} M) mixture was added to 90 ml of silver nitrate solution (1.11×10^{-3} M) and stirred for 15 min. The synthesized colloidal nanoparticles were characterized with dynamic light scattering (DLS) (Zetasizer Nano ZS, Malvern) and UV-Visible spectroscopy (Lambda 25, Perkin Elmer). Citrate reduced ones had an average size of 30 nm and hydroxylamine reduced ones had an average size of 50 nm. In order to concentrate the suspensions, they were centrifuged at

5500 rpm for 30 minutes, whole water on the top of the precipitated was removed, and appropriate amount of water was added to obtain a specific concentration.

3.3. SAMPLE PREPARATION

3.3.1. Preparation of Protein Mixtures for SERS Study of Binary Mixtures of Proteins

Protein solutions were prepared in the concentration of two μM . Then, a volume of 100 μl binary mixtures of protein solutions was prepared by mixing a specific concentration of proteins, such as 1.2 μM hemoglobin and 0.8 μM cytochrome c (the total protein concentration for all the protein mixtures was kept constant at two μM). Then, the prepared solutions were mixed with 100 μl of 16 times concentrated hydroxylamine reduced AgNP colloidal suspension (16x) (final concentrations of protein mixtures and AgNP colloidal suspensions was one μM and 8x, respectively).

3.3.2. Preparation of Solutions

For evaluation of the effects of the addition of various molecules to serum, appropriate amount of the chemicals was weighed so that final concentrations of the chemicals were one mM both in water and in commercial human serum.

For evaluation of the effects of the addition of proteins to filtered commercial human serum, appropriate amount of protein powders were weighed and added into serum.

For the SERS study of binary mixtures of purines and purine derivatives, appropriate amount of their powder was weighed and added to either phosphate or borate buffer to prepare solutions with 200 μM concentrations.

3.3.3. Preparation of Blood Serum Samples

In order to prepare filtered human serum, commercial human serum was filtered with 3 kDa 15 ml Amicon filters by centrifugation at 4000 rpm for one hour.

Protein extraction from commercial human serum was achieved by methanol extraction. Fifty μl of serum samples mixed with different amounts of ice cold methanol (50 μl , 100 μl , 150 μl , 200 μl , 250 μl , and 300 μl). Mixtures were vortexed for one minute and incubated at $-20\text{ }^{\circ}\text{C}$ for 30 minutes. Then they were centrifuged at 11000 rpm at $+4\text{ }^{\circ}\text{C}$ for 30 minutes. Supernatants were pipetted and put into different microcentrifuge tubes, and air dried in a cabin. After drying, 50 μl of distilled water was added into tubes and vortexed.

Blood samples of cancer patients, patients with chronic diseases, and healthy individuals were obtained from Sakarya University Training and Research Hospital. Human samples collection was approved by the Yeditepe University Human Ethical Committee. Of healthy individuals, eighteen person was male and 12 was female donors (mean age: 54.9, standard deviation: 11.2, median age: 56). The list of chronic disease patients and their information are provided in Table 3.1. The list of cancer patients and their information can be seen in Table 3.2. After collection, blood samples was kept at the room temperature for about 45 minutes in serum collection tubes, then centrifuged at 2000 g for 10 minutes. Supernatant part of the samples was then transferred to clean DNase, RNase free 1.5 ml microcentrifuge tubes. Samples were kept at $-80\text{ }^{\circ}\text{C}$ freezer until used.

Table 3.1. The list of chronic disease patients.

Patient	Age	Gender	Chronic disease
P1	38	M	kidney stone
P2	48	M	diabetes
P3	63	M	hypertension
P4	38	F	stomach related
P5	42	F	bronchitis, heart related problems
P6	55	F	hypertension, respiratory distress

P7	55	F	hypertension
P8	55	F	diabetes, hypertension, atherosclerosis
P9	55	F	kidney stone, diabetes
P10	60	F	osteoporosis
P11	63	F	bile stone
P12	66	F	diabetes, hypertension, osteoporosis
P13	66	F	sinuses, osteoporosis
P14	75	F	arthritis
P15	80	F	arthritis
Mean age	57.3		
± SD	12.4		
Median age	55		

Table 3.2. The list of cancer patients. Blood samples after tumor removal were obtained from the patients with star symbol.

Patient	Age	Gender	Cancer Type	Days passed after tumor removal for second blood take
P1	55	M	Abdominal cancer	
P2*	46	F	Breast cancer	123
P3	57	F	Breast cancer	
P4	73	F	Breast cancer	
P5	60	M	Colon cancer	
P6	61	M	Colon cancer	
P7*	66	M	Colon cancer	14
P8*	71	M	Colon cancer	58
P9	72	M	Colon cancer	
P10	82	M	Colon cancer	
P11*	56	M	Fibrosis	98
P12*	66	M	Gastric cancer	21
P13	71	M	Gastric cancer	
P14	56	F	Gastrointestinal cancer	
P15*	60	F	Liver cancer	17
P16	63	M	Small intestinal cancer	
P17	65	M	Anorectal cancer	
P18	43	F	Rectal cancer	

P19	51	F	Rectal cancer	
P20*	58	F	Rectal cancer	73
P21*	41	M	Rectal cancer	13
P22*	56	M	Rectal cancer	118
P23	59	M	Rectal cancer	
P24*	64	M	Rectal cancer	28
P25*	65	M	Rectal cancer	28
P26*	66	M	Rectal cancer	90
P27*	72	M	Rectal cancer	61
P28*	73	M	Rectal cancer	16
P29	77	M	Rectal cancer	
P30	87	M	Rectal cancer	
Mean age	63.1			
± SD	10.6			
Median age	63.5			

3.4. SERS EXPERIMENTAL SETUP

All prepared samples were mixed with appropriate amount of AgNP colloids and mixtures spotted on CaF₂ slides. SERS spectra of the samples were acquired using a Renishaw inVia Reflex Raman spectrometer. Spectrometer was equipped with 830 nm laser. An 50x objective was used. The system was automatically calibrated against a silicon wafer peak at 520 cm⁻¹ each time before experiments. Laser power was 1.5-3 mW. Exposure time was 10 seconds.

3.5. SERS DATA PROCESSING

The spectra were smoothed, baseline corrected, and normalized using Wire 4.0 (Raman spectrometer's software). Multivariate data analysis was performed using SPSS 20.0 (IBM) and PLS-Toolbox (Eigenvector Research Inc.).

4. RESULTS AND DISCUSSION

4.1. CHARACTERIZATION OF SILVER NANOPARTICLES

As stated in the materials and methods section, AgNPs were synthesized using two different reducing agents, hydroxylamine hydrochloride and citrate, namely. UV-Visible spectroscopy is widely used for determination of the size of noble metal nanoparticles (NPs) such as gold [98] and silver [99]. The peak values of the absorption spectra of the AgNPs give information about the most abundant NP size (i.e., average size) in a colloidal AgNP suspension [100]. Figure 4.1 shows UV-Vis spectrum of the hydroxylamine hydrochloride reduced AgNPs. Absorption maximum of the spectrum was 415 nm, corresponding to an average size of 44 nm. Zeta potential of the AgNPs was -27 mV.

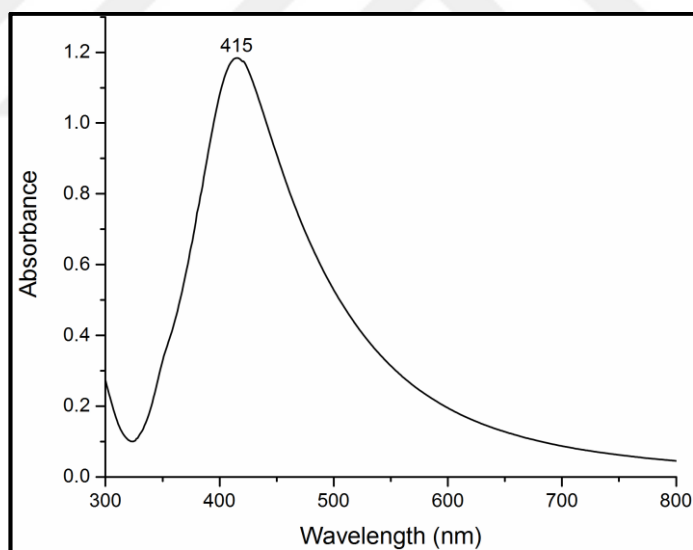


Figure 4.1. UV-Visible spectrum of the hydroxylamine hydrochloride reduced AgNPs.

Since the aim of the second part of the thesis study was about the evaluation of the SERS technique for label free cancer detection and its possible use in a clinical environment, the stability of the SERS substrates (i.e., AgNPs) for a time period was crucial. Therefore, UV-Vis spectra of the citrate reduced AgNPs were acquired once in a week over seven months and results were shown in Figure 4.2. As seen in the figure, all UV-Vis spectra were similar and their standard deviation was extremely small implying that AgNP colloid was

stable over seven months. The maximum absorbance was at 405 nm, corresponding to an average size of 30 nm.

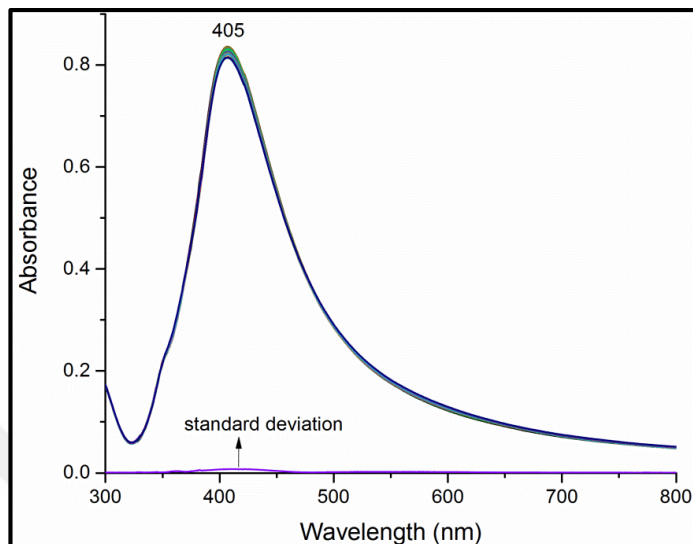


Figure 4.2. UV/Visible spectra of the citrate reduced AgNPs for seven months (a total of 29 spectra).

Zeta potentials of the citrate reduced AgNP were also acquired once in a week over seven months (Figure 4.3). Zeta potential of the AgNPs was stable around -40 mV for that time period.

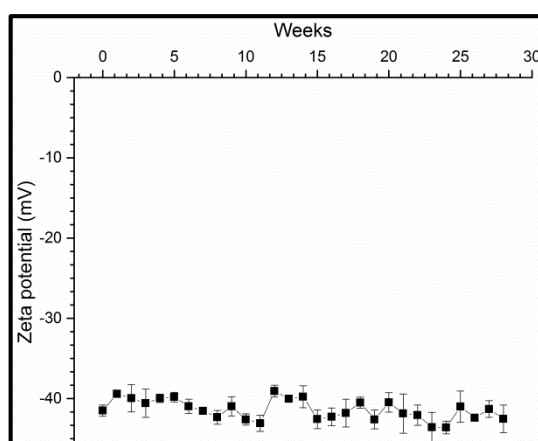


Figure 4.3. Zeta potential of the citrate reduced AgNP colloid over seven months. Standard deviations are of three different measurements.

4.2. INFLUENCE OF PROTEIN SIZE ON SURFACE-ENHANCED RAMAN SCATTERING SPECTRA IN BINARY PROTEIN MIXTURES

Proteins possess complex structure and have either globular or elongated (fibrous) shape. As they contain various types of zwitterionic amino acids, their overall charges change according to the pH of the surrounding environment. The pH where they carry zero net charge is called isoelectric point (pI). Below their isoelectric point, proteins are basic in nature and possess positive charge, whereas above this point, they are acidic and possess negative charge. The surface charges (zeta potential) of the proteins used in this study were measured in pure water (pH 6.9) using Zetasizer and are presented in Table 4.1. While apotransferrin, human serum albumin (HSA), fibrinogen, hemoglobin, and immunoglobulin A (IgA) are negatively charged, lysozyme, cytochrome c, and immunoglobulin G (IgG) are positively charged at pH 6.9. The other important point in the table is that hydrodynamic radius of the protein increases as the molecular weight of the protein increases. The seven proteins, which obey this trend, are globular proteins, and the only protein that does not obey is fibrinogen. It is a fibrous protein and has a length of 47.5 nm [101]. Since DLS technique assumes the particles in suspensions as spheres, real physical dimensions of fibrinogen are not similar to its hydrodynamic radius due to its elongated structure. On the other hand, its hydrodynamic radius was found as 15.68 nm, which is consistent with previous studies [101-103].

Table 4.1. Physicochemical properties of the proteins.

Protein	MW (kDa)	Hydrodynamic radius (nm)	Isoelectric point (pI)	Zeta potential (mV)	Property
Hemoglobin	64.5	3.90	6.8	-10.4	Acidic
HSA	66.5	4.40	4.7-5.2	-28.9	Acidic
Apotransferrin	76-81	7.91	5.9	-16.9	Acidic
IgA	150-350	16.25	4.63-6.85	-27.2	Acidic
Fibrinogen	340	15.68	5.8-6.1	-9.53	Acidic
Cytochrome c	12.3	2.01	10.5	+22.5	Basic
Lysozyme	14.3	2.15	11.4	+25.9	Basic
IgG	150	12.66	5.5-9.5	+14.5	Basic

The choice of a substrate is a very important step for the quality and reproducibility of the SERS spectra. In most of SERS studies, AgNPs or gold nanoparticles (AuNPs) are used due to simple preparation, low cost, and high sensitivity [104-106]. Since Raman cross sections of many molecules (especially of biologically relevant ones) are small, many times anomalous signals stemming from the molecular remnants of the colloid synthesis or molecules coating the nanoparticle surface interfere and appear on the acquired spectra [107, 108]. When the low intensity of the SERS spectra of proteins is considered, these anomalous signals can make the interpretation of the protein spectra harder. The citrate reduced AgNPs are the most widely used substrates in our laboratories and in the SERS community. Another prevalently used colloidal AgNP type is the hydroxylamine reduced one. Figure 4.4 shows SERS spectra of both colloidal AgNP types. Before acquisition of these spectra, colloidal AgNP suspensions were centrifuged and all the aqueous supernatants on the top of the muddy AgNP precipitates were removed for further elimination of species causing anomalous signals. As seen in the figure, SERS spectrum of the citrate reduced AgNPs possess many citrate bands. On the other hand, the only band in the SERS spectrum of hydroxylamine reduced AgNPs is around 1050 cm^{-1} which is attributed to nitrate ions (for AgNP synthesis, silver nitrate is used as silver source). Therefore, hydroxylamine reduced colloidal AgNPs were used for SERS study of proteins.

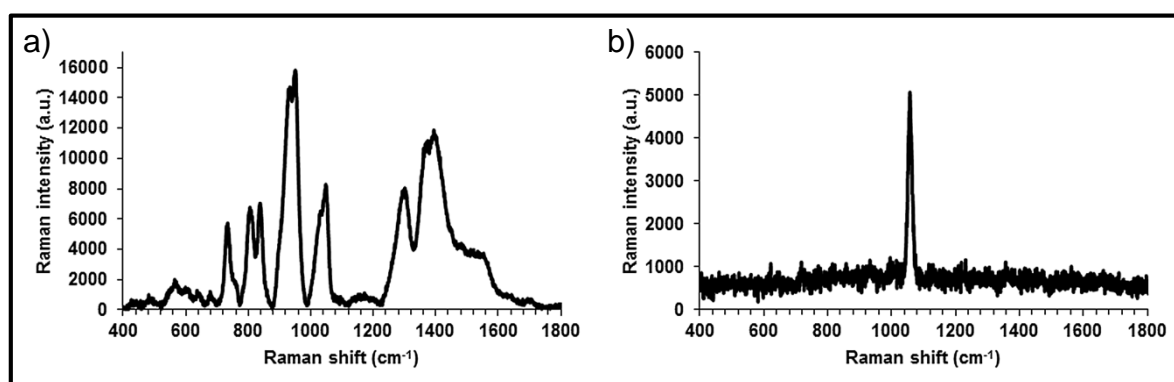


Figure 4.4. SERS spectra of (a) citrate reduced AgNPs and (b) hydroxylamine reduced AgNPs.

The other important point for protein-SERS is the concentration of AgNPs. In order to obtain good quality, reproducible spectra from proteins, concentrated AgNP colloids should be used. This necessity was demonstrated in previous reports published in literature

[109-112]. Sizes of proteins are in nanometer scale; therefore proteins can be thought of as nanostructures. Upon mixing with AgNPs, they coat the NPs and they fill the voids among the AgNPs in the aggregates, which might have a quenching effect on surface plasmon formation. This might be a negative contributing factor to the quality of the SERS spectra of proteins. Therefore, an increased number of AgNPs in the experiment increases the probability of proteins in the close proximity to AgNP surfaces in the aggregates.

Zeta potential of the AgNP colloid was measured as -27 mV, which means that it would interact better with positively charged proteins than negatively charged ones. The pH of the AgNP colloid and protein mixture was found as 7.01 which was not significantly different from the pH of the water (6.90) used to dissolve proteins. Therefore, zeta potentials of the proteins did not change much, and their degree of interaction with AgNPs remained more or less the same. The negatively charged proteins formed small aggregates due to weak interactions with AgNPs, while positively charged ones formed larger aggregates due to stronger interactions. This phenomenon was shown in previous reports by our group [109, 110]. Since acquired SERS spectra of negatively charged proteins from dried deposited area of a sessile droplet are poor, to facilitate further accumulation of proteins and AgNPs in a more confined area, the droplets dried in suspended position. A report of our group in previous years showed that with this method, quality and reproducibility of the protein SERS spectra increases [110]. In addition, intensity of the spectra varies within deposited area [113], and for quantitative analysis using droplet deposition technique, all spectra for all samples have to be acquired from same regions. In this study, all spectra were acquired from the middle regions of the deposited areas. A representative image of the spectra acquired area is demonstrated in Figure 4.5. Ten SERS spectra of each protein and their standard deviations are shown in Figure 4.6. Each protein has its distinct spectral shape.

PCA (principal component analysis) is widely used for large Raman datasets having multiple dimensions [114-117]. In this method, a number of variables are reduced while retaining most of the variance. Differentiation and classification of large datasets using the extracted principal components provide further analysis of the data. Figure 4.7 shows the differentiation of the eight different proteins used in this study using PCA. First, the three principal components explained 89 percent of the total variance among proteins. Cytochrome c and hemoglobin were well separated from the others. They contain the heme

group, and the contribution of this group to their SERS spectra gives these two proteins their distinct fingerprint spectral properties. The clusters of the other five proteins (fibrinogen, HSA, lysozyme, apotransferrin, and IgG) were also differentiated. On the other hand, PCA scores of IgA were widely spread. The intragroup variability might have been the reason for this. PCA is not a supervised method, and both variability within the groupings and variability between the groupings contribute to the variance, and sharp spectral features affect variance. The intragroup variances (i.e., variance among the ten spectra of each mixture) here resulted in the wide distribution of the IgA scores on the plot.

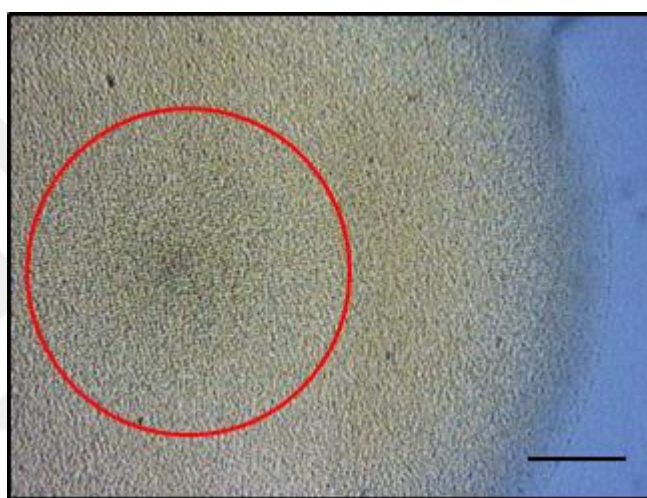


Figure 4.5. A part of the deposition area of 0.4 μM Cyt c-0.6 μM Hb and AgNP mixture. SERS spectra were acquired from the encircled area. Scale bar represents 200 μm .

After proving that each protein was well distinguished by PCA, the next study was the analysis of the samples containing binary mixtures of proteins for size effects on SERS spectra. As stated in the introduction section, there are only three reports about SERS study of the protein mixtures, and two of them are from our group. In one of earlier study by our group, proteins were separated using convective assembly method and detected with SERS [111]. In the other study, protein-melting temperatures were used to be able to detect each protein in ternary mixtures using SERS [112]. In that work, concentrations of the proteins were the same (50 $\mu\text{g}/\text{ml}$) and citrate reduced silver nanoparticles were used for SERS analysis. In order to show dissimilarity between spectra acquired at different temperatures, two-dimensional Euclidian distance plots were constructed.

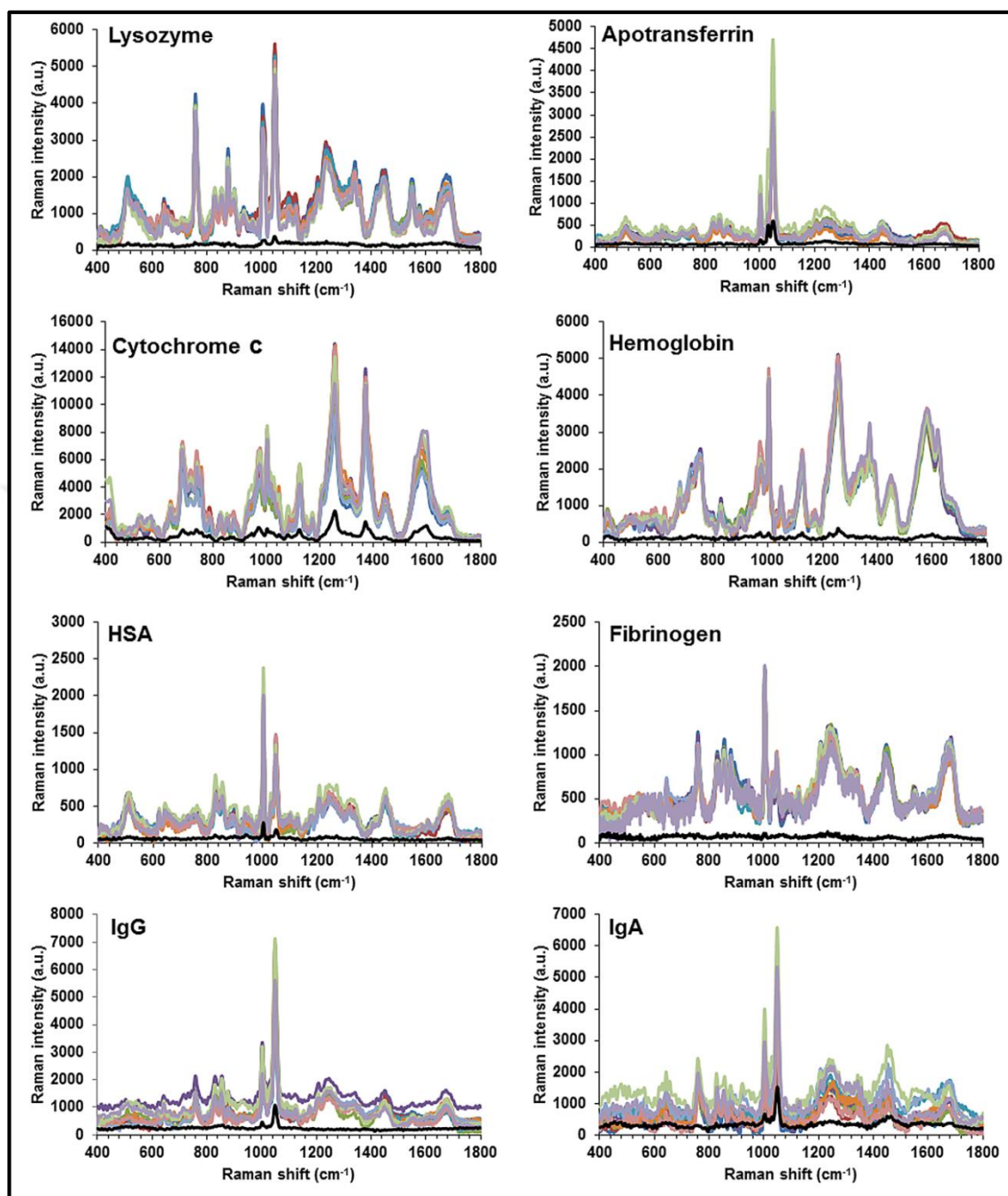


Figure 4.6. Ten SERS spectra of each protein and their standard deviations (in black).

In another report, Zhen *et al.* used a heat-induced SERS sensing method for detection of binary mixtures of proteins [118]. They classified proteins into groups as proteins with and without chromophores. Total concentration of the proteins in each mixture was 10 μ M, and the AgNPs were citrate reduced ones. The studied proteins were small or mid-sized compared to the protein sizes used in this study.

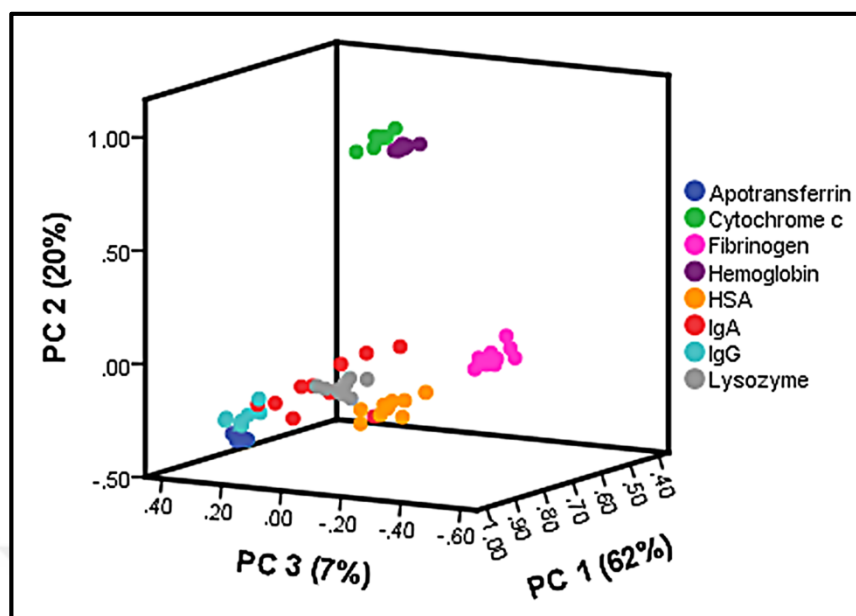


Figure 4.7. PCA plot of SERS spectra of eight proteins.

In addition, in their work, the investigations were only based on spectral differences, and there was no multivariate analysis. SERS spectra of proteins are usually weak compared with other smaller molecules and the major contributions to the spectra come from three aromatic ring containing amino acids, namely, tyrosine, tryptophan, and phenylalanine. The spectra become even weaker as the size of the protein increases. Mixing more than one proteins also further complicates interpretation of the SERS spectra. Therefore, multivariate analysis and data reduction approaches can be helpful for thorough interpretation of the collected data sets.

Figure 4.8 (a) shows the spectra of lysozyme (Lys) and apotransferrin (apoTrf) mixtures with different relative concentrations, and Figure 4.8 (b) shows the plot of the peak intensities of 758 cm^{-1} (Trp), 1002 cm^{-1} (Phe), and 1240 cm^{-1} (Amide III) [119] at increased concentration of the Lys in the mixture. Note that each spectrum was average of 10 spectra collected at different locations on the droplet area. As seen in Figure 4.8 (b), as the concentration of the Lys increases relative to apoTrf, the intensities of the three peaks increase. The intensities of the other bands also increase, but, for comparison, only intensity of three peaks was plotted. Lys was positively charged and apoTrf was negatively charged in AgNP-proteins mixture; therefore Lys would make stronger interactions with negatively charged AgNPs than apoTrf does, and the bands originating from Lys in the

SERS spectra would dominate in the presence of Lys in the mixture. On the other hand, the results presented on Figure 4.8 (a) show that at relatively higher apoTrf concentrations, spectra resembled to the spectrum of only apoTrf rather than of only Lys, which tells us that interactions due to charges are not the only determinant in the SERS of proteins. It is strongly possible that apoTrf has stronger binding affinity to the AgNP surface though the functional groups such as $-\text{COO}$, $-\text{SH}$, and $-\text{OH}$ groups on the protein surface. Proteins are nanometer-sized, and they can form a few nanometer thick coatings on the metallic NPs. Since apoTrf coated the AgNPs at its relatively higher concentrations, Lys could not approach to the surface of the AgNPs. Therefore, the collected spectra resemble more to that of only apoTrf.

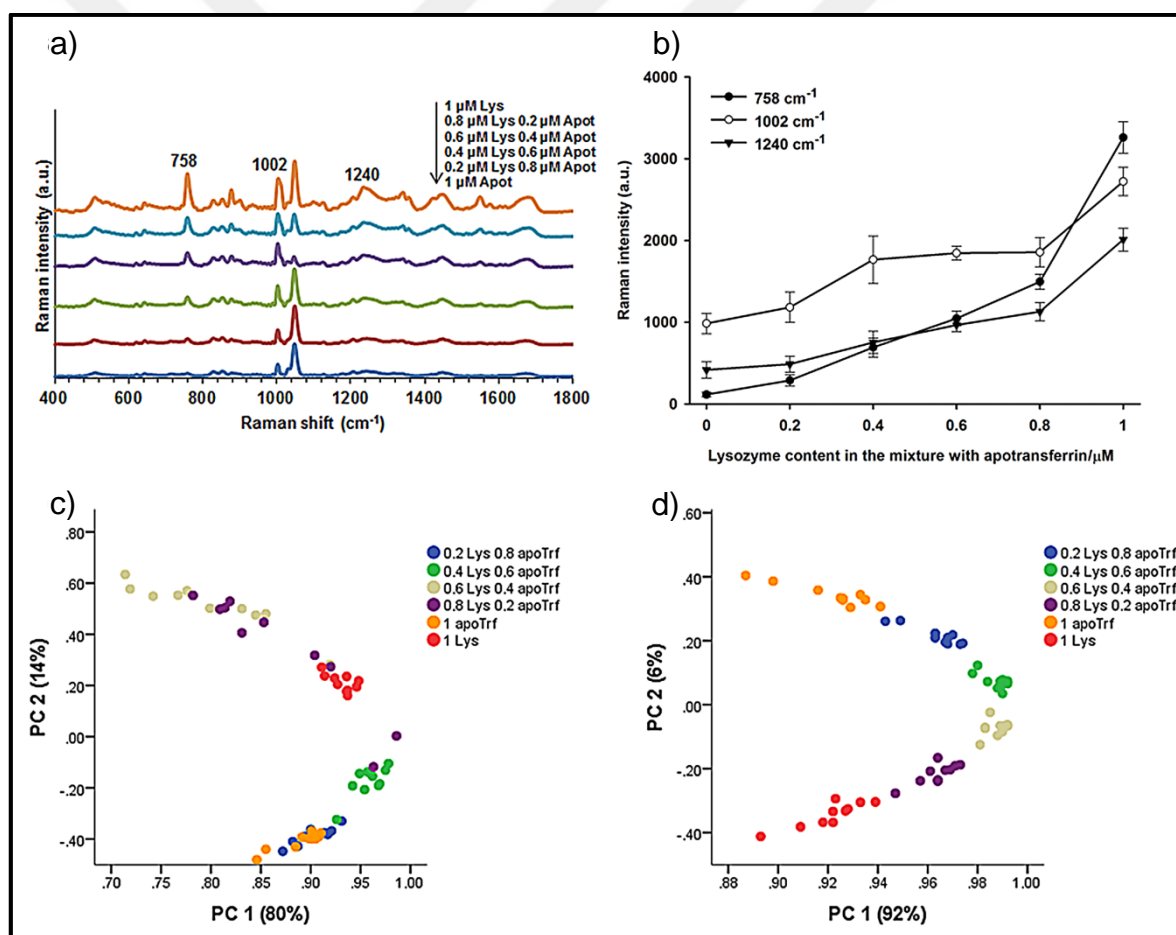


Figure 4.8. (a) SERS spectra for mixtures of Lys and apoTrf with different relative concentrations. (b) Peak intensities at 758, 1002, and 1240 cm^{-1} . (c) PCA analysis of SERS spectra of the mixtures. (d) PCA analysis of the mixed spectra data sets constructed using weighted sums of the spectra of individual proteins.

Multivariate analysis of the spectra further verified the concentration-dependent contribution to the SERS spectra of the mixtures. PCA scores plotted for each mixture are shown in Figure 4.8 (c). First principal component (PC1) represented 80 percent of the explained variance, and PC2 of 20 percent. Both PC1 and PC2 contributed to the discrimination of each mixture. Since the scores of each mixture were located in the positive part of the scores plot with respect to PC1, scores of mixtures having higher Lys concentration and scores of mixtures having higher apoTrf concentration were located in the opposite parts (positive and negative part) of the plot with respect to PC2. In addition, scores of 0.6 μM Lys-0.4 μM apoTrf and 0.8 μM Lys-0.2 μM apoTrf were overlapped, and scores of one μM apoTrf and 0.2 μM Lys-0.8 μM apoTrf were also mixed, meaning, in these two sets, spectra closely resembled each other. Normally, at the two extremes in the plot with respect to PC2, the scores of one μM apoTrf and one μM Lys should have located due to the least similarity, but in our findings this was not the case. The scores of one μM Lys were closer to the scores of the mixtures having relatively higher concentrations of apoTrf than any other mixture containing less amounts of apoTrf. With a close inspection of the spectra on Figure 4.8 (a), the reason was found for this interesting situation to be the band centered around 1050 cm^{-1} , which is attributed to nitrate ions. As the remnants of the colloid synthesis, nitrate ions also co-adsorb on the surface of AgNPs along with proteins. On the other hand, protein composition of the mixture may change quantity of nitrate adsorption; therefore the intensity of the peak at 1050 cm^{-1} may change in different protein compositions. Similar findings were also reported by Zhou *et al.* [118] In their study, binary mixtures of myoglobin (Mb) and apomyoglobin with relatively different concentrations did not change the intensity of the nitrate peak. On the other hand, intensity of the peak varied with binary mixtures of cytochrome c and HSA. To confirm the effect of the 1050 cm^{-1} peak on the distribution of the scores, mixed spectra data sets were constructed using weighted sums of the spectra of individual proteins (Figure 4.8 (d)). Binary mixtures of Lys and apoTrf in different amounts were well separated, and scores of the only Lys and only apoTrf were in the extremes with respect to PC2.

The other binary mixture was of Cyt c and Mb. Figure 4.9 (a) shows the spectra of Cyt c and Hb mixtures with different relative concentrations, and Figure 4.9 (b) shows intensities of the peaks at $756\text{ (}\nu_{15}\text{B}_{1g}\text{)}$ [120], $1125\text{ (}\nu_{22}\text{A}_{2g}\text{)}$ [121], and $1370\text{ (}\nu_4\text{)}$ [122]. Both proteins possess heme group. On the other hand, since Cyt c is positively and Hb is negatively

charged in the mixture with AgNPs, Cyt c makes stronger interactions with AgNPs than Hb. Therefore, the peaks of heme group became more intense when it is in the structure of Cyt c. In addition, intensity of the peaks increased and spectra resembled more to the spectrum of Cyt c, as the concentration of Cyt c in the mixture increased.

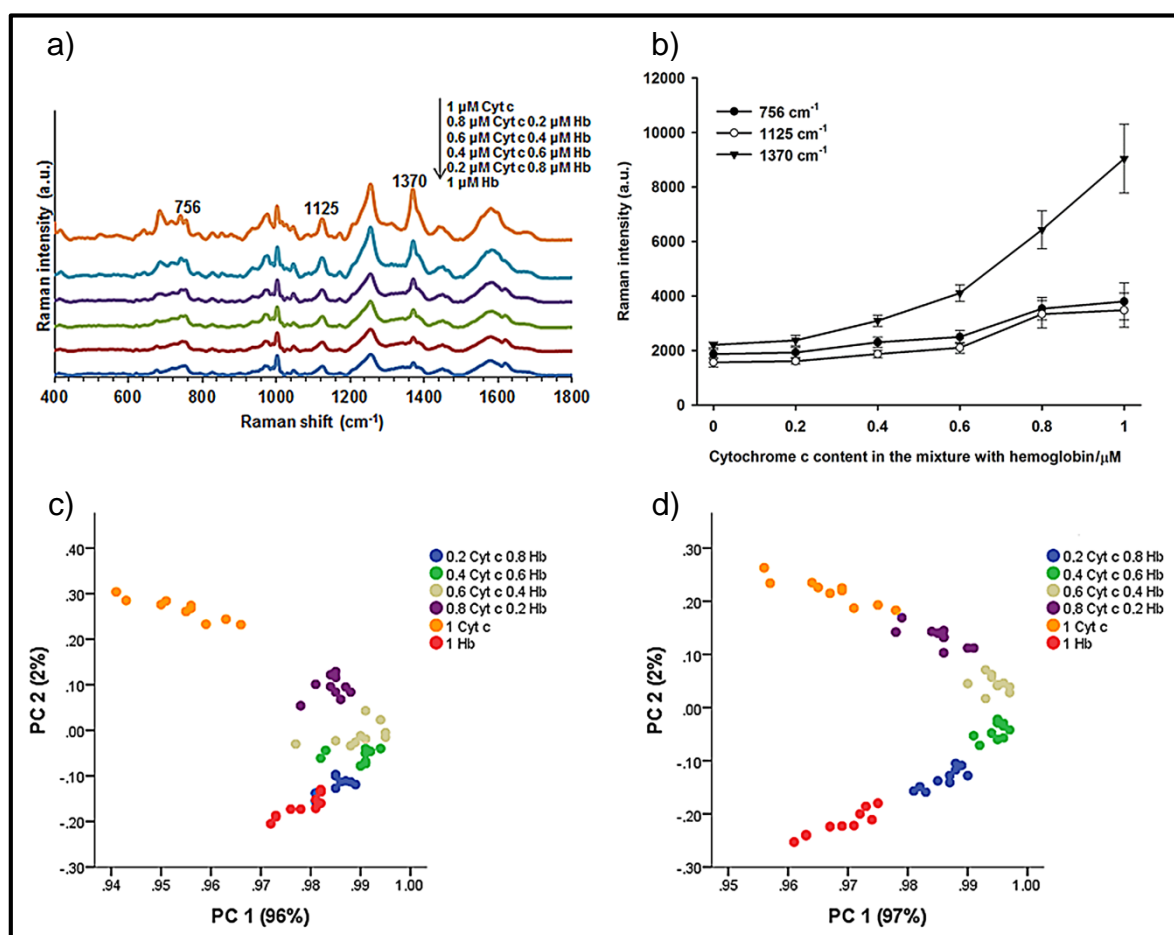


Figure 4.9. (a) SERS spectra for mixtures of Cyt c and Hb with different relative concentrations. (b) Peak intensities at 756, 1125, and 1370 cm⁻¹. (c) PCA analysis of SERS spectra of the mixtures. (d) PCA analysis of the mixed spectra data sets constructed using weighted sums of the spectra of individual proteins.

Regarding the PCA scores plot of the mixtures, it was observed that each cluster representing different mixtures was well discriminated as seen in Figure 4.9 (c). PC1 described 96 percent of the observed variance, and PC2 of 2 percent. Each mixture was located in the positive part of the scores plot with respect to PC1. The mixtures containing only individual proteins resided at the both extremes with respect to PC2. The mixtures

containing relatively higher amount of Cyt c were positioned in the positive side along PC2 axis, whereas the mixtures containing higher amount of Hb were positioned in the negative side. Mixed spectra data sets were also constructed using weighted sums of the spectra of individual proteins as shown in Figure 4.9 (d). Each mixture was successfully differentiated. When both PCA plots were compared, it was obvious that distribution patterns of the mixtures according to their content on both plots were more or less similar. Therefore, it could be stated that PCA was a useful tool for proper discrimination of the mixtures of Cyt c and Hb with respect to their relative concentrations in the mixture.

Thus far, the studies for binary mixtures of small and mid-sized proteins and the implications of these patterns on PCA of the mixtures were demonstrated. First, mixtures of Lys and apoTrf were analyzed. Both SERS spectra analysis and PCA revealed that spectra of the mixtures were dominated by the protein having relatively higher concentration, and intensity of the characteristic peaks of Lys gradually increased as its concentration is increased. On the PCA plot, due to close similarity of the spectra and due to effects of nitrate peak on variance, some mixtures of two proteins could not be differentiated efficiently. On the other hand, PCA results of the other protein mixtures (Cyt c and Hb) were quite good. Clusters of each mixture were located in different positions and the order of the clusters with respect to PC2 was the same with increase in or decrease in the concentrations of both proteins. Those four proteins were small or mid-sized, and in order to test identification and discrimination ability of SERS analysis and efficiency of PCA with larger proteins, the study was preceded with binary mixtures of HSA-Fb and IgG-IgA.

HSA has a hydrodynamic radius of four nm; on the other hand Fb is an elongated protein having length of 45 nm, much larger than HSA. In addition, both of them are negatively charged in the mixture with AgNPs. When the diameter of the AgNPs is considered (50 nm), in similar concentrations of both proteins and when concentration of Fb is higher, Fb surrounds the AgNPs due to its huge size and HSA cannot find enough room to come near AgNPs. Therefore, prior to the experiment, it was assumed that spectral patterns were the dominance of the peaks of Fb when the concentrations of the proteins were close and when the concentration of Fb was higher than that of HSA. The results verified my assumptions. As demonstrated in Figure 4.10 (a), in three out of four different HSA-Fb mixtures (spectra

of the individual proteins are omitted), spectra were dominated by the bands of Fb, and spectra were similar to the spectrum of Fb. Intensity of the peaks at 760 cm^{-1} (Trp), 1002 cm^{-1} (Phe), and 1449 cm^{-1} (CH_2) [50] with respect to the HSA concentration presented a bell shaped curve (Figure 4.10 (b)) and maximum intensity was of the mixture containing $0.6\text{ }\mu\text{M}$ HSA. A possible reason for this situation might have been the change of aggregation status of AgNPs. While Fb contributed more to the spectra of the mixtures, HSA at $0.6\text{ }\mu\text{M}$ might have changed aggregation status of the AgNPs and more hot spots were created, and this led to intensity increase of Fb bands. That is to say, change in the aggregation status of AgNPs at $0.6\text{ }\mu\text{M}$ HSA concentration made a synergistic contribution to the SERS bands of Fb.

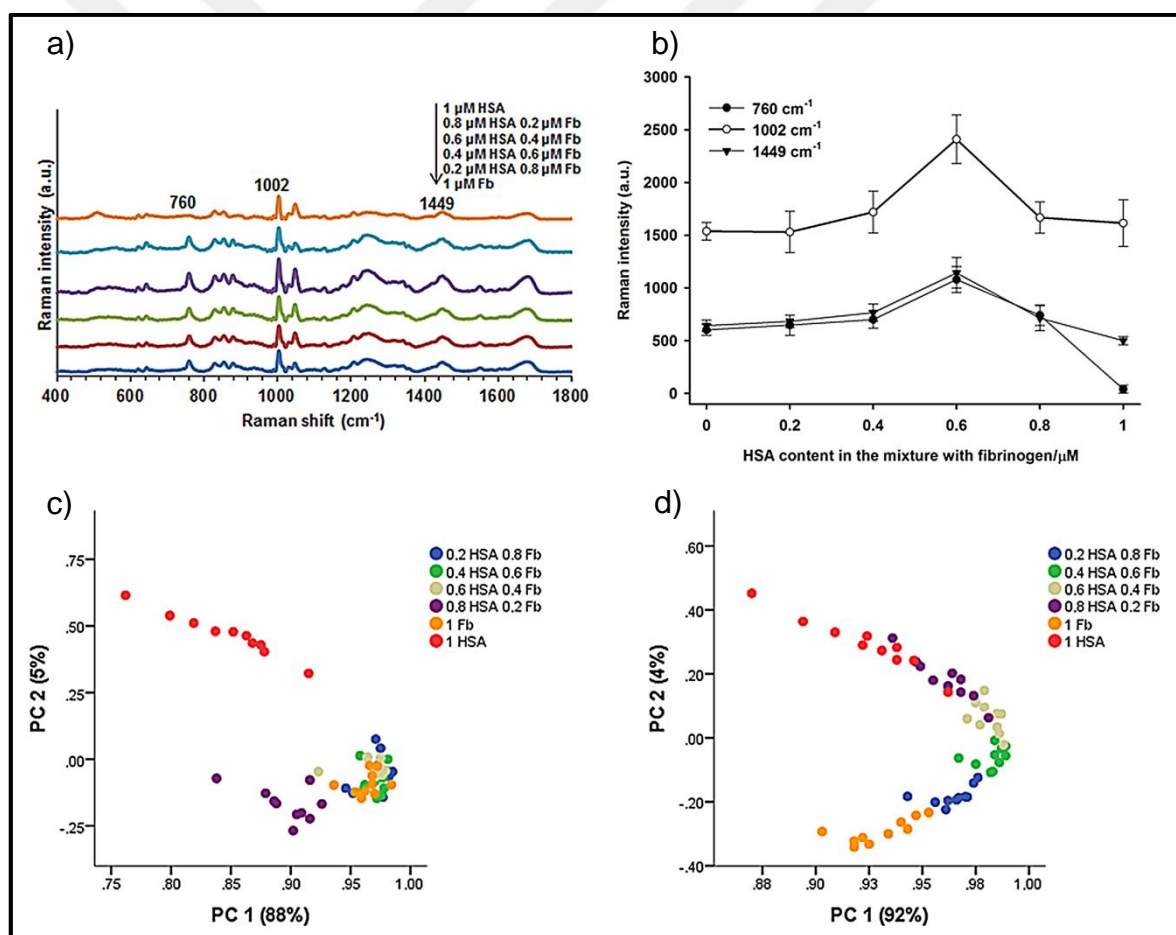


Figure 4.10. (a) SERS spectra for mixtures of HSA and Fb with different relative concentrations. (b) Peak intensities at 760, 1002, and 1449 cm^{-1} . (c) PCA analysis of SERS spectra of the mixtures. (d) PCA analysis of the mixed spectra data sets constructed using weighted sums of the spectra of individual proteins.

PCA scores plot of the mixtures are presented in Figure 4.10 (c). The only differentiated clusters were of 1 μ M HSA, and of the mixture of 0.8 μ M HSA and 0.2 μ M Fb. Due to close similarity of the spectra, scores of the all the other mixtures overlapped. Results showed that PCA was incapable of differentiation when small sized and much bigger sized proteins were mixed. On the other hand, the PCA plot constructed by using mixed spectra data sets formed by using weighted sums of the spectra of individual proteins showed differentiation of all of the mixtures (Figure 4.10 (d)). This also demonstrates that spectra of individual HSA and Fb were quite dissimilar according to algorithms of PCA.

The final binary mixture was of IgG and IgA. They are larger proteins than the other proteins used in the study except Fb. As shown in Figure 4.11 (a), the spectra of some mixtures contained intense nitrate peak, and some of them did not, and this made PCA plots more complicated (Figure 4.11 (c)). Although PCA differentiated IgA and IgG, due to spectral similarity, the mixtures of IgG and IgA could not be differentiated efficiently. The PCA plot in Figure 4.11 (d) constructed by using mixed spectra data sets formed by using weighted sums of the spectra of them was also complicated and hard to interpret. The intensity of the peaks at 760, 1002, and 1449 cm^{-1} presented bell shaped variation (Figure 4.11 (b)). The reason for this might have been the same reason for HSA-Fb mixtures, that is, the change in the aggregation status of the AgNPs. The results showed that the PCA could not efficiently differentiate the binary mixtures of larger proteins under the experimental conditions used in this study. The presence or absence of an intense nitrate peak in spectrum of each mixture contributed to the total variance and this directly affected the outcomes of PCA.

The proteins investigated as large sized were IgG, IgA, and Fb and as medium sized was HSA in this study. In addition to the size, the molecular flexibility of the protein might have an effect on their effective interaction with the AgNPs. When the nature of the protein-AgNP interactions is considered, unless the interaction is covalent through -SH or -NH₂ moieties on the protein surface, the larger and more rigid protein molecules may not adhere to the AgNP surfaces through the weaker ionic interactions.

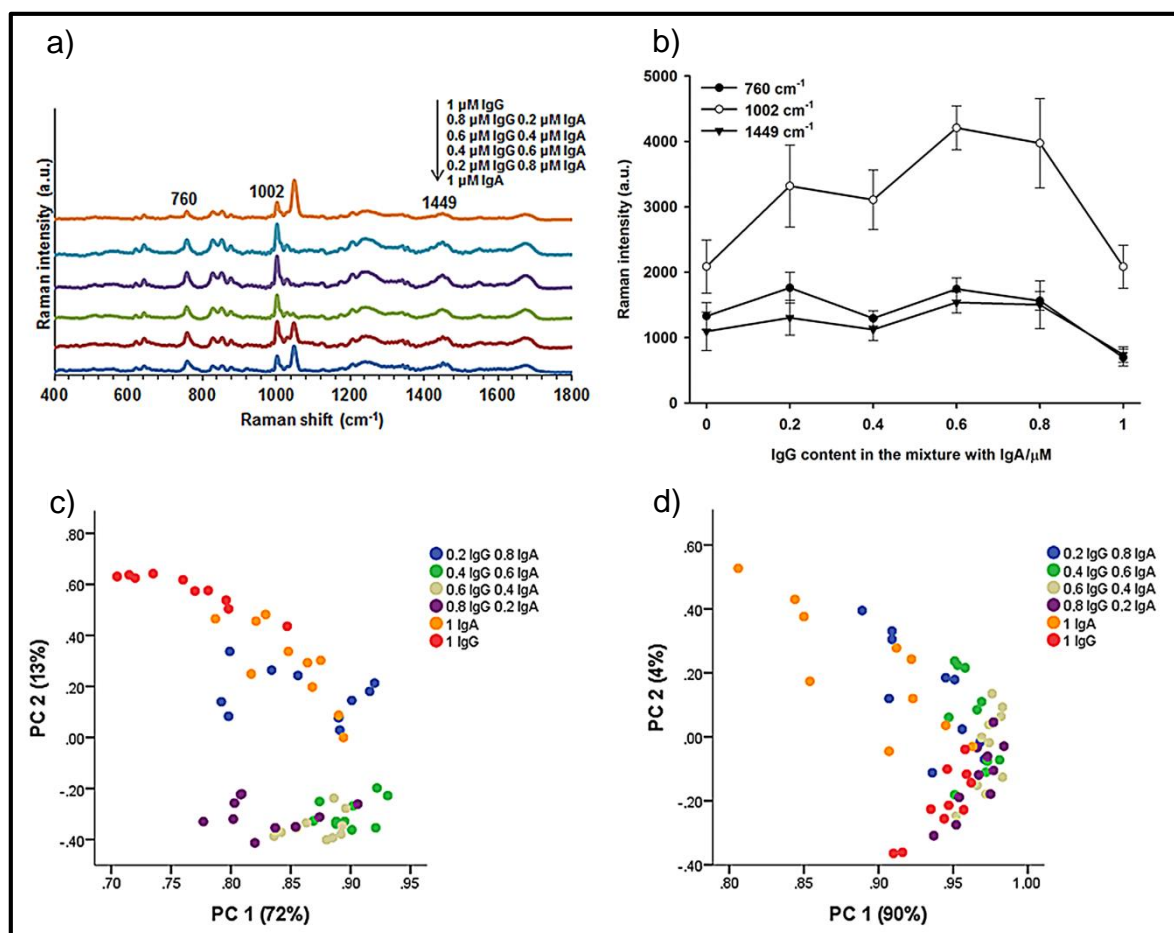


Figure 4.11. (a) SERS spectra for mixtures of IgG and IgA with different relative concentrations. (b) Peak intensities at 760, 1002, and 1449 cm⁻¹. (c) PCA analysis of SERS spectra of the mixtures. (d) PCA analysis of the mixed spectra data sets constructed using weighted sums of the spectra of individual proteins.

In addition, the interaction kinetics may play a role for the stronger interactions of larger proteins. A slower interaction due to slower diffusion of proteins to the AgNP surface because of their larger size may not provide enough time for the protein molecules to orient themselves on the AgNP surface for a proper attachment during the drying process of a suspension droplet.

After PCA analysis of the SERS spectra of the binary mixtures of proteins, a different multivariate analysis method, Partial least squares-discriminant analysis (PLS-DA) was applied for differentiation of the spectra. PLS-DA is a supervised analysis method which tries to find latent variables (which are like principal components (PCs) in PCA)) with a

maximum covariance with Y -variables [123]. In this study, X -variables were the SERS spectra of proteins and Y -variables were the class assignments of each spectrum. A total of 60 protein SERS spectra (10 for each protein) was analyzed using PLS-DA. Leave-one-out cross validation was used for validation of class assignments. Root mean square errors of cross validations (RMSECV) were calculated as a function of found latent variables and demonstrated in Figure 4.12. Since 10 latent variables correspondent to a minimum in the RMSECV, this number of latent variables were used to create PLS-DA model.

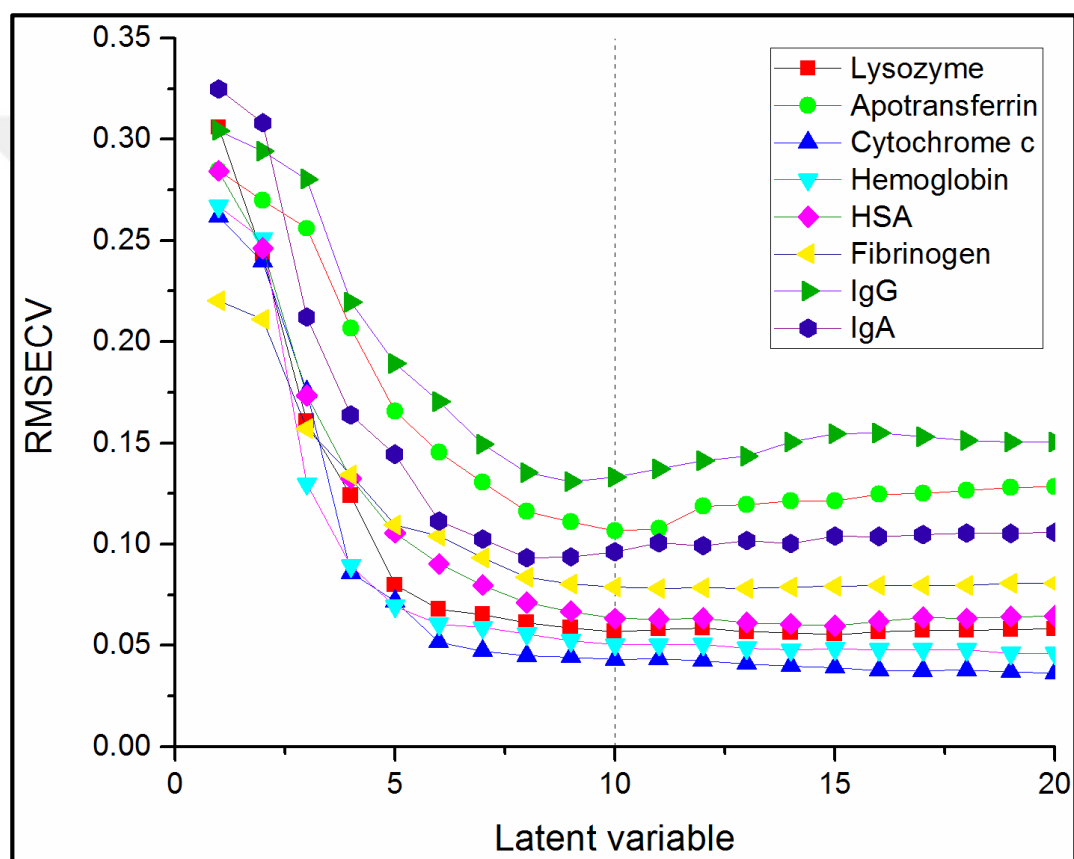


Figure 4.12. Plot of RMSECV results for different latent variable numbers.

Using PLS-DA model with 10 latent variables, classification of each protein was done separately. Classification results are shown in Figure 4.13. Dashed red line in each panel shows threshold values for classification. Table 2 shows confusion table results for the cross validation model. All proteins were classified correctly; therefore average sensitivity and average specificity were 100 percent.

Since eight different proteins had distinct spectral patterns, good PLS-DA classification results were not surprising. Next step was to see performance of PLS-DA method for binary mixtures of proteins. First protein couple was Lys and apoTrf mixture. RMSECV values were calculated as a function of found latent variables and demonstrated in Figure 4.14. Since 16 latent variables correspondent to a minimum in the RMSECV, this number of latent variables were used to create PLS-DA model.

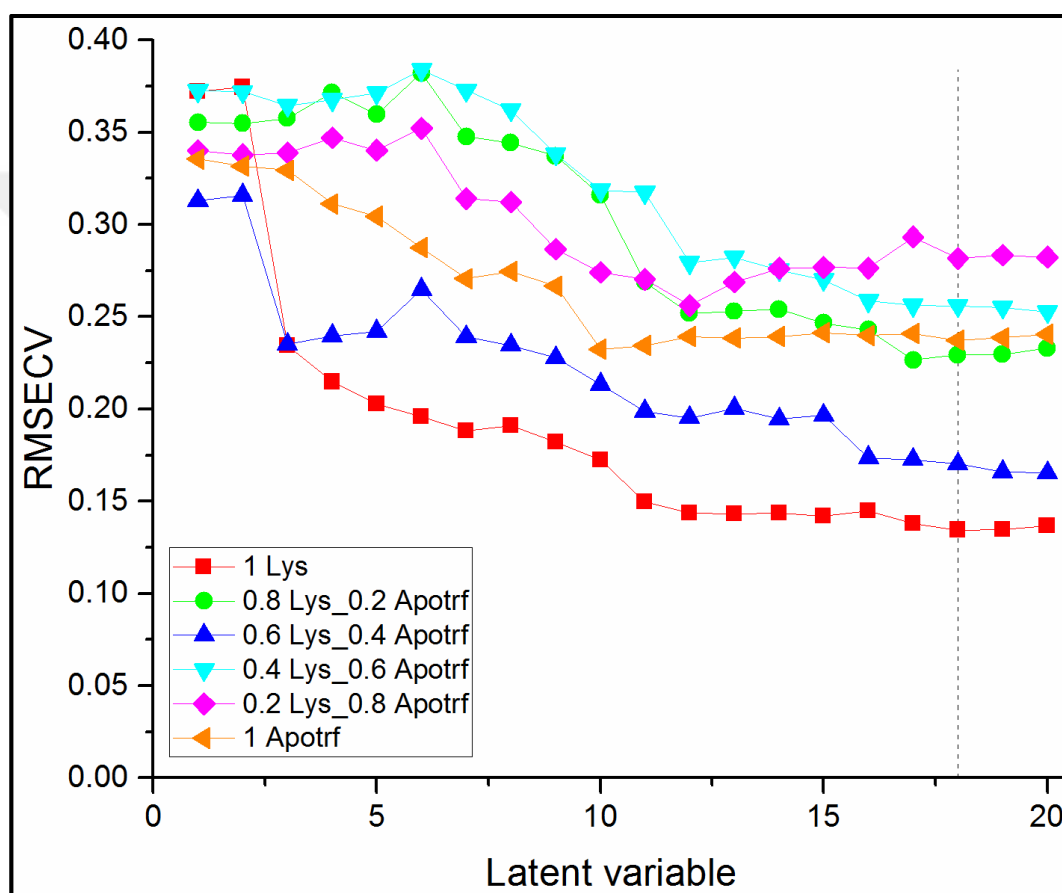


Figure 4.14. RMSECV results of Lys and apoTrf mixtures as a function of the number of latent variable numbers.

Classification results are shown in Figure 4.15. Table 4.3 shows confusion table results for the cross validation model. As seen in Table 4.4, average sensitivity, average specificity, and average accuracy of PLS-DA results were higher than 90 percent. Compared to PCA, PLS-DA was better for discrimination of binary mixtures of Lys and apoTrf.

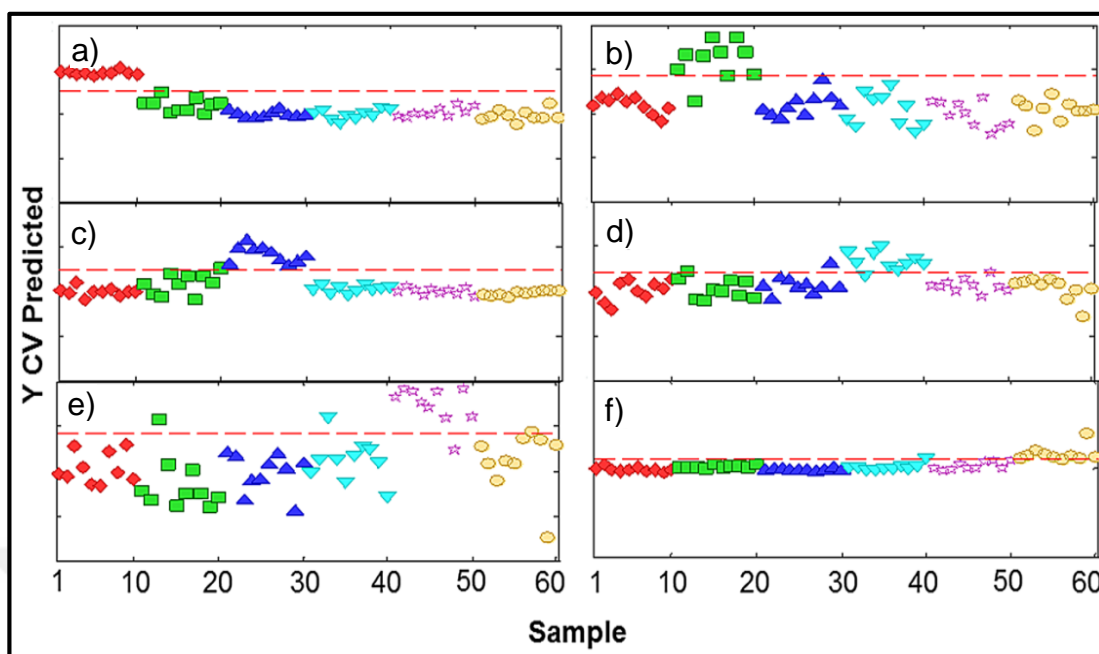


Figure 4.15. Cross-validated PLS-DA classification results of the SERS spectra of (a) Lys (one μM), (b) Lys (0.8 μM)+apoTrf (0.2 μM), (c) Lys (0.6 μM)+apoTrf (0.4 μM), (d) Lys (0.4 μM)+apoTrf (0.6 μM), (e) Lys (0.2 μM)+apoTrf (0.8 μM), (f) apoTrf (one μM) proteins. The horizontal dashed red line is the threshold for classification membership for each protein.

Table 4.3. Confusion table results for the PLS-DA cross validation model of Lys and apoTrf mixtures. (1) Lys (one μM), (2) Lys (0.8 μM)+apoTrf (0.2 μM), (3) Lys (0.6 μM)+apoTrf (0.4 μM), (4) Lys (0.4 μM)+apoTrf (0.6 μM), (5) Lys (0.2 μM)+apoTrf (0.8 μM), (6) apoTrf (one μM).

		Actual					
		1	2	3	4	5	6
Predicted	1	10	1	0	0	0	0
	2	0	8	0	0	0	0
	3	0	0	9	0	0	0
	4	0	0	1	9	1	0
	5	0	1	0	1	9	0
	6	0	0	0	0	0	10

Table 4.4. Sensitivity and specificity results for classification of Lys and apoTrf mixtures.

Class	Sensitivity (%)	Specificity (%)	Accuracy (%)
Lys (1 μ M)	100	98	98
Lys (0.8 μ M)+apoTrf (0.2 μ M)	80	100	97
Lys (0.6 μ M)+apoTrf (0.4 μ M)	90	100	98
Lys (0.4 μ M)+apoTrf (0.6 μ M)	90	96	95
Lys (0.2 μ M)+apoTrf (0.8 μ M)	90	96	95
apoTrf (1 μ M)	100	100	100
Average	92	98	97

The other binary protein mixtures were of Cyt c and Hb. RMSECV values were calculated as a function of found latent variables and demonstrated in Figure 4.16. Since 15 latent variables correspondent to a minimum in the RMSECV, this number of latent variables were used to create PLS-DA model.

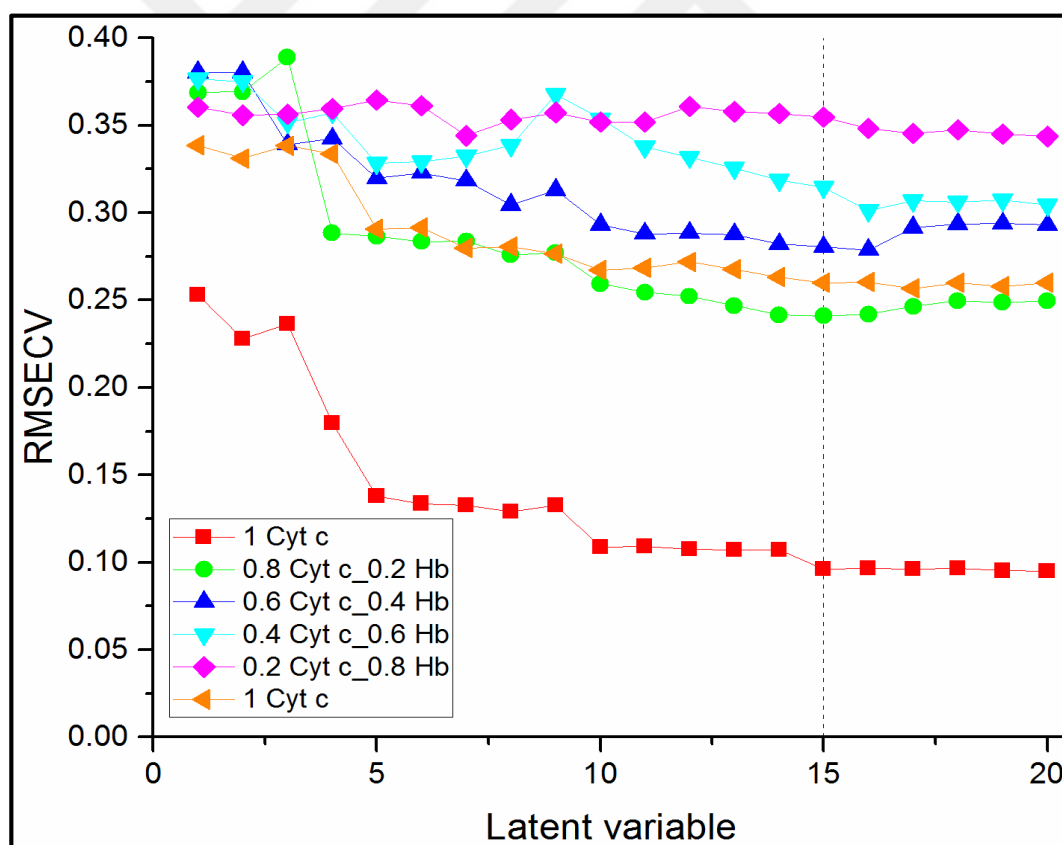


Figure 4.16. RMSECV results of Cyt c and Hb mixtures as a function of the number of latent variable numbers.

Classification results are shown in Figure 4.17. Table 4.5 shows confusion table results for the cross validation model. As seen in Table 4.6, average sensitivity was 80 percent, average specificity was 96 percent, and average accuracy of PLS-DA was 93 percent.

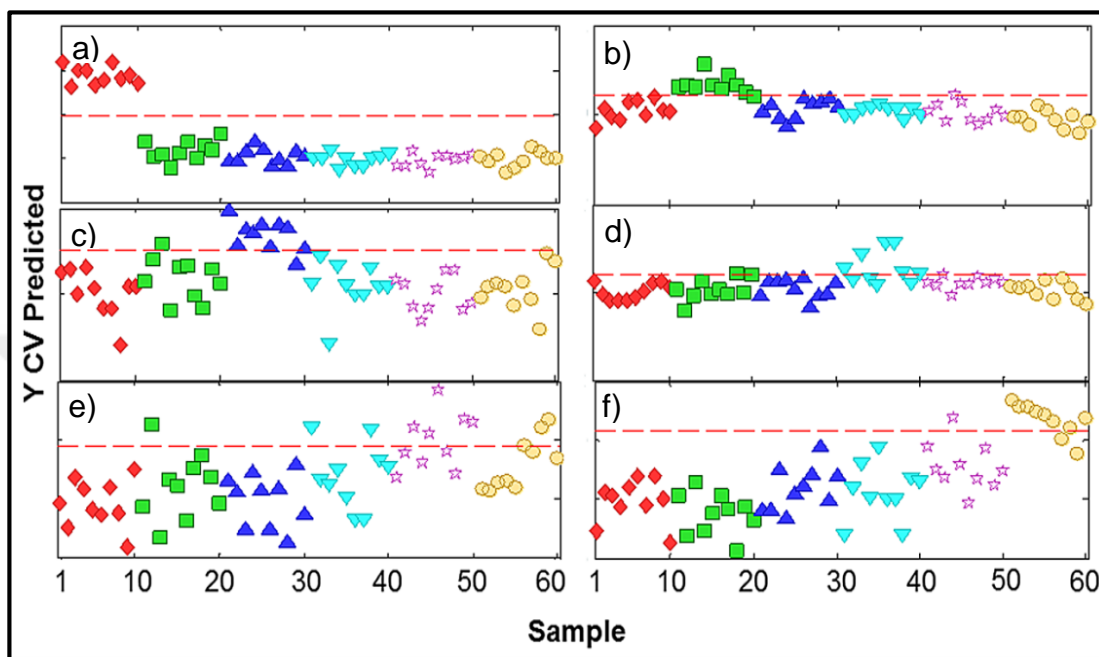


Figure 4.17. Cross-validated PLS-DA classification results of the SERS spectra of (a) Cyt c (one μM), (b) Cyt c (0.8 μM)+Hb (0.2 μM), (c) Cyt c (0.6 μM)+Hb (0.4 μM), (d) Cyt c (0.4 μM)+Hb (0.6 μM), (e) Cyt c (0.2 μM)+Hb (0.8 μM), (f) Hb (one μM) proteins. The horizontal dashed red line is the threshold for classification membership for each protein.

Table 4.5. Confusion table results for the PLS-DA cross validation model of Cyt c and Hb mixtures. (1) Cyt c (one μM), (2) Cyt c (0.8 μM)+Hb (0.2 μM), (3) Cyt c (0.6 μM)+Hb (0.4 μM), (4) Cyt c (0.4 μM) Hb (0.6 μM), (5) Cyt c (0.2 μM)+Hb (0.8 μM), (6) Hb (one μM).

		Actual					
		1	2	3	4	5	6
Predicted	1	10	0	0	0	0	0
	2	0	9	1	0	0	0
	3	0	0	9	0	0	0
	4	0	1	0	6	1	0
	5	0	0	0	3	6	2
	6	0	0	0	1	3	8

Table 4.6. Sensitivity and specificity results for classification of Cyt c and Hb mixtures.

Class	Sensitivity (%)	Specificity (%)	Accuracy (%)
Cyt c (1 μM)	100	100	100
Cyt c (0.8 μM)+Hb (0.2 μM)	90	98	97
Cyt c (0.6 μM)+Hb (0.4 μM)	90	100	98
Cyt c (0.4 μM) Hb (0.6 μM)	60	96	90
Cyt c (0.2 μM)+Hb (0.8 μM)	60	90	85
Hb (1 μM)	80	92	90
Average	80	96	93

The other binary protein mixtures were of HSA and Fb. RMSECV values were calculated as a function of found latent variables and demonstrated in Figure 4.18. Since 15 latent variables correspond to a minimum in the RMSECV, this number of latent variables were used to create PLS-DA model.

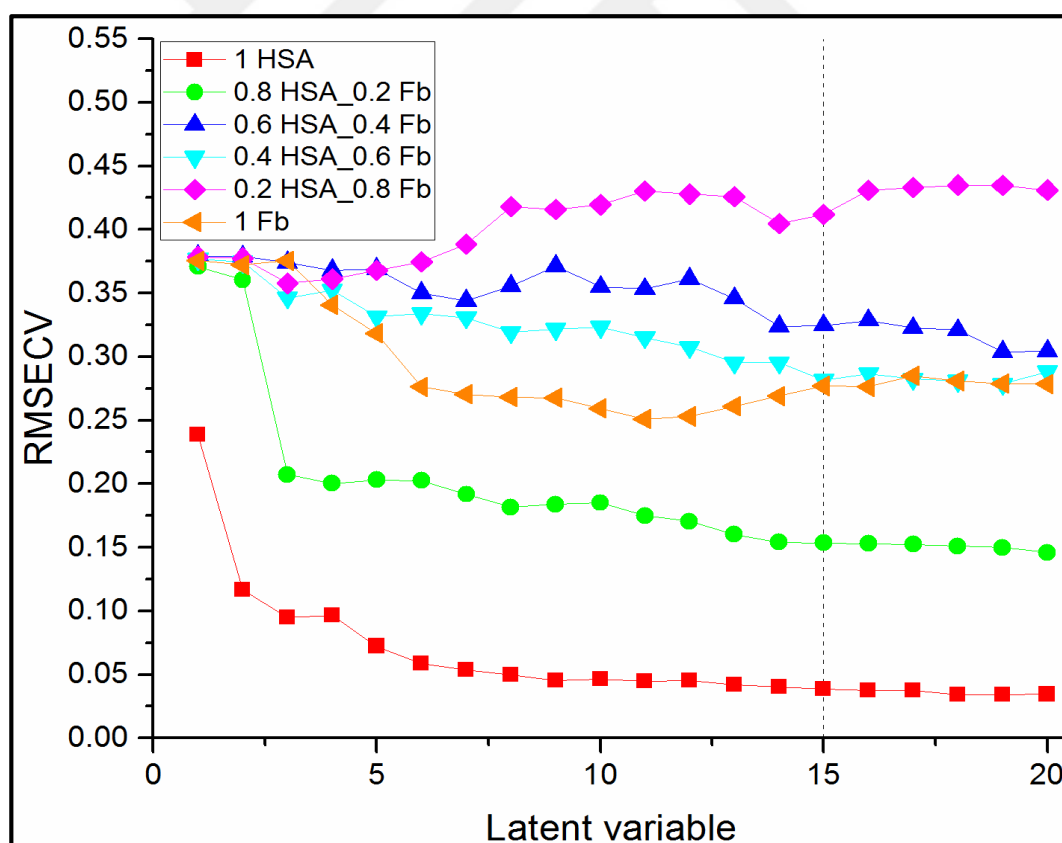


Figure 4.18. RMSECV results of HSA and Fb mixtures as a function of the number of latent variable numbers.

Classification results are shown in Figure 4.19. Table 4.7 shows confusion table results for the cross validation model. As seen in Table 4.8, average sensitivity was 82 percent, average specificity was 96 percent, and average accuracy of PLS-DA was 94 percent. Compared to PCA, PLS-DA was a lot better for discrimination of binary mixtures of HSA and Fb.

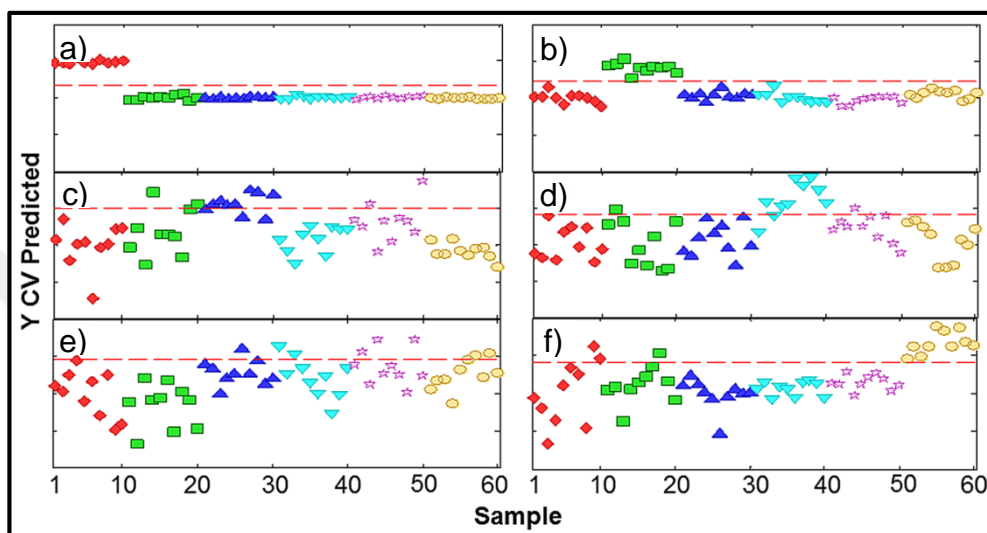


Figure 4.19. Cross-validated PLS-DA classification results of the SERS spectra of (a) HSA (1 μM), (b) HSA (0.8 μM)+Fb (0.2 μM), (c) HSA (0.6 μM)+Fb (0.4 μM), (d) HSA (0.4 μM)+Fb (0.6 μM), (e) HSA (0.2 μM)+Fb (0.8 μM), (f) Fb (1 μM) proteins. The horizontal dashed red line is the threshold for classification membership for each protein.

Table 4.7. Confusion table results for the PLS-DA cross validation model of HSA and Fb mixtures. (1) HSA (one μM), (2) HSA (0.8 μM)+Fb (0.2 μM), (3) HSA (0.6 μM)+Fb (0.4 μM), (4) HSA (0.4 μM)+Fb (0.6 μM), (5) HSA (0.2 μM)+Fb (0.8 μM), (6) Fb (one μM).

		Actual					
		1	2	3	4	5	6
Predicted	1	10	0	0	0	0	0
	2	0	9	0	0	0	0
	3	0	1	8	0	2	0
	4	0	0	1	8	3	0
	5	0	0	1	2	4	0
	6	0	0	0	0	1	10

Table 4.8. Sensitivity and specificity results for classification of HSA and Fb mixtures.

Class	Sensitivity (%)	Specificity (%)	Accuracy (%)
HSA (1 μM)	100	100	100
HSA (0.8 μM)+Fb (0.2 μM)	90	100	98
HSA (0.6 μM)+Fb (0.4 μM)	80	94	92
HSA (0.4 μM) Fb (0.6 μM)	80	92	90
HSA (0.2 μM)+Fb (0.8 μM)	40	94	85
Fb (1 μM)	100	98	98
Average	82	96	94

The last binary protein mixtures were of IgG and IgA. RMSECV values were calculated as a function of found latent variables and demonstrated in Figure 4.20. Since 16 latent variables correspondent to a minimum in the RMSECV, this number of latent variables were used to create PLS-DA model.

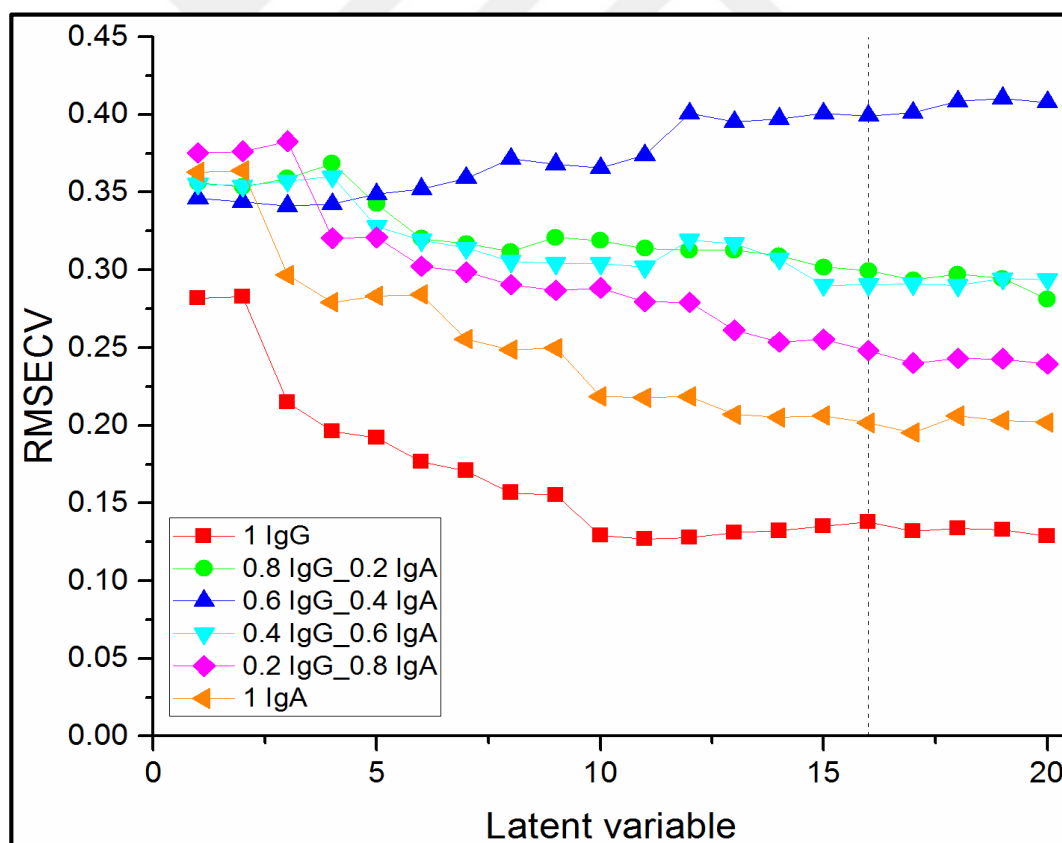


Figure 4.20. RMSECV results of IgG and IgA mixtures as a function of the number of latent variable numbers.

Classification results are shown in Figure 4.21. Table 4.9 shows confusion table results for the cross validation model. As seen in Table 4.10, average sensitivity was 82 percent, average specificity was 96 percent, and average accuracy of PLS-DA was 94 percent. Compared to PCA, PLS-DA was a lot better for discrimination of binary mixtures of IgG and IgA.

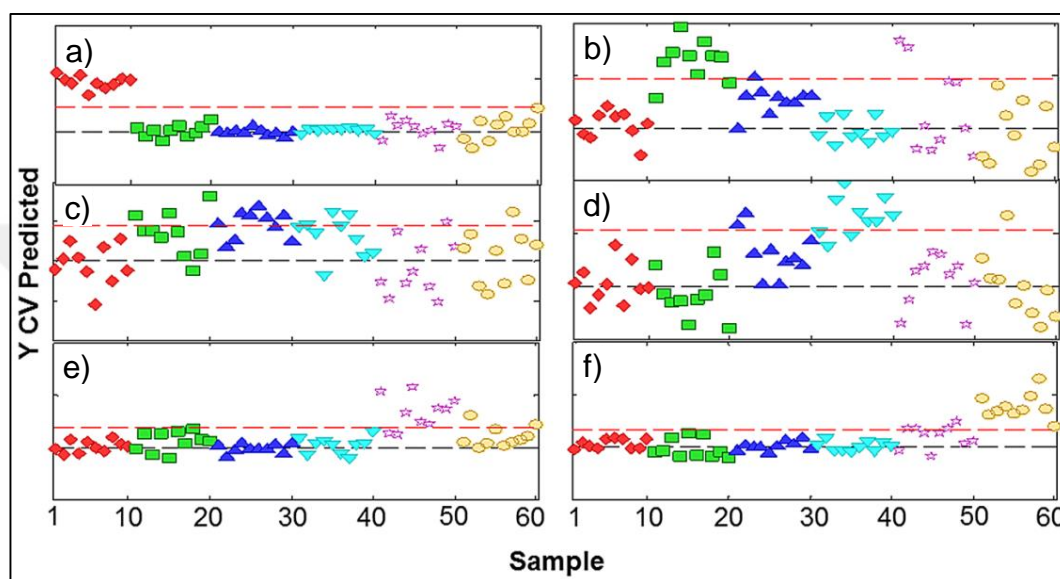


Figure 4.21. Cross-validated PLS-DA classification results of the SERS spectra of (a) IgG (one μM), (b) IgG (0.8 μM)+ IgA (0.2 μM), (c) IgG (0.6 μM)+ IgA (0.4 μM), (d) IgG (0.4 μM)+ IgA (0.6 μM), (e) IgG (0.2 μM)+ IgA (0.8 μM), (f) IgA (one μM) proteins. The horizontal dashed red line is the threshold for classification membership for each protein.

Table 4.9. Confusion table results for the PLS-DA cross validation model of IgG and IgA mixtures. (1) IgG (one μM), (2) IgG (0.8 μM)+IgA (0.2 μM), (3) IgG (0.6 μM)+IgA (0.4 μM), (4) IgG (0.4 μM)+IgA (0.6 μM), (5) IgG (0.2 μM)+IgA (0.8 μM), (6) IgA (one μM).

		Actual					
		1	2	3	4	5	6
Predicted	1	10	0	0	0	0	0
	2	0	8	1	0	2	0
	3	0	2	7	3	0	0
	4	0	0	2	7	0	0
	5	0	0	0	0	7	0
	6	0	0	0	0	1	10

Table 4.10. Sensitivity and specificity results for classification of IgG and IgA mixtures.

Class	Sensitivity (%)	Specificity (%)	Accuracy (%)
IgG (1 μ M)	100	100	100
IgG (0.8 μ M)+IgA (0.2 μ M)	80	94	92
IgG (0.6 μ M)+IgA (0.4 μ M)	70	90	87
IgG (0.4 μ M)+IgA (0.6 μ M)	70	96	92
IgG (0.2 μ M)+IgA (0.8 μ M)	70	100	95
IgA (1 μ M)	100	98	98
Average	82	96	94

As the all PLS-DA results were analyzed, it was observed that PLS-DA performance for discrimination of binary mixtures of proteins was better than PCA.

4.3. LABEL-FREE SURFACE-ENHANCED RAMAN SCATTERING FOR CANCER DETECTION

4.3.1. Reproducibility of the SERS Spectra of Filtered and Unfiltered Serum

It is well known that reproducibility is the most fundamental issue in a SERS experiment. High protein content of serum prevents AgNP aggregation and causes low intensity signals [124]. Uneven distribution of AgNP aggregates in a dried droplet decreases reproducibility. Therefore sufficient amount of AgNPs must be used to obtain reproducible and quality SERS signals of serum. In order to investigate the effects of AgNP concentration on serum SERS spectrum, 64x, 32x, 16x, 8x, 4x, 2x, and 1x AgNP colloids were mixed with whole (unfiltered) commercial serum and ten spectra were acquired from the middle region of three dried droplets for each AgNP concentration. Results are shown in Figure 4.22 and 4.23. Please note that final AgNP concentrations were decreased by a factor of two due to serum mixing (i.e., 64x to 32x, and so forth) and these final concentration values are mentioned starting from this part of the report. The use of final 32x and 16x AgNP colloids resulted in obtaining reproducible spectra. On the other hand, intensity of the SERS spectra dropped a bit with the latter one due to AgNP concentration decrease. With 8x AgNP colloid, intensity of the spectra decreased further and intensity differences among the spectra collected from different dried droplets were observed. On the other hand, spectral patterns were the same in all spectra. Starting with 4x

concentration, further AgNP concentration decreases (i.e., 4x to 0.5x) lowered the intensity and reproducibility of the collected spectra significantly, and increased the noise of the spectra. Further confirmation of the protein effects on the SERS spectra of serum was provided by doing the same procedures for filtered serum. Serum was filtered with membrane with three kDa cut-off. As seen in Figure 4.24 and 4.25, from 32x AgNP to 0.5x AgNP concentration, intensity of the acquired spectra decreased by 50 percent only and spectra did not become noisy.

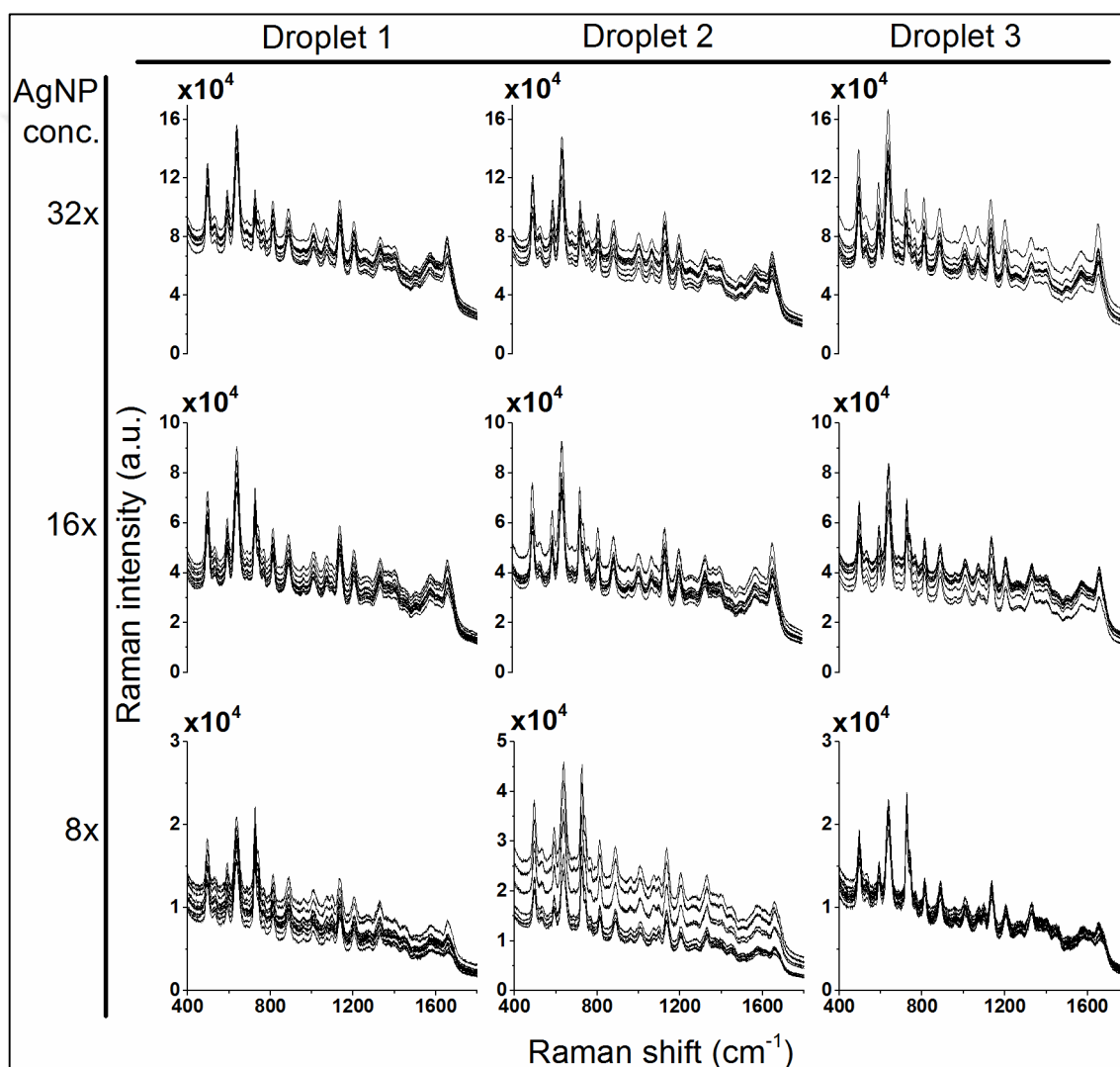


Figure 4.22. Raw SERS spectra of three dried droplets of whole serum samples with different AgNP concentrations (32x, 16x, 8x).

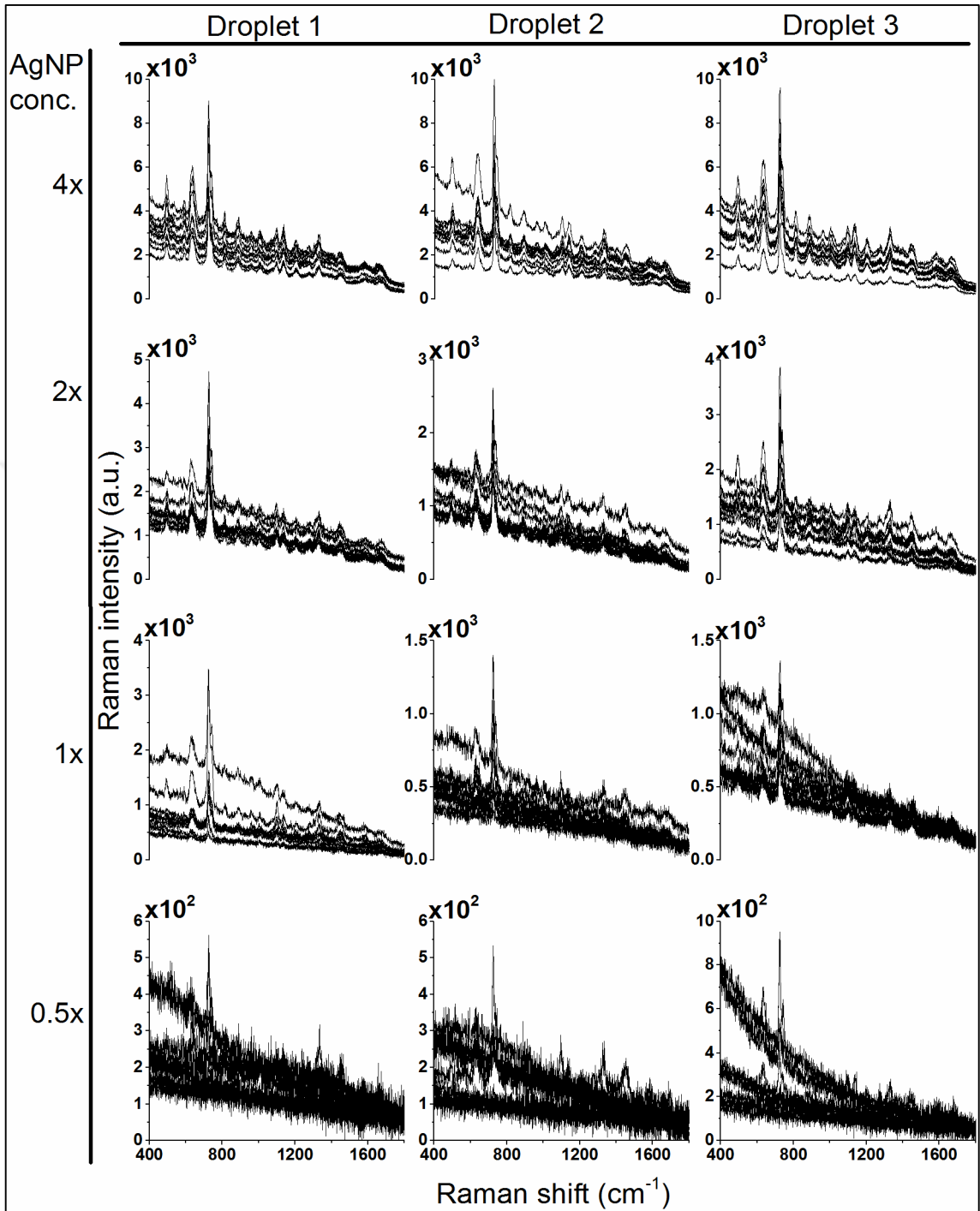


Figure 4.23. Raw SERS spectra of three dried droplets of whole serum samples with different AgNP concentrations (4x, 2x, 1x, 0.5x).

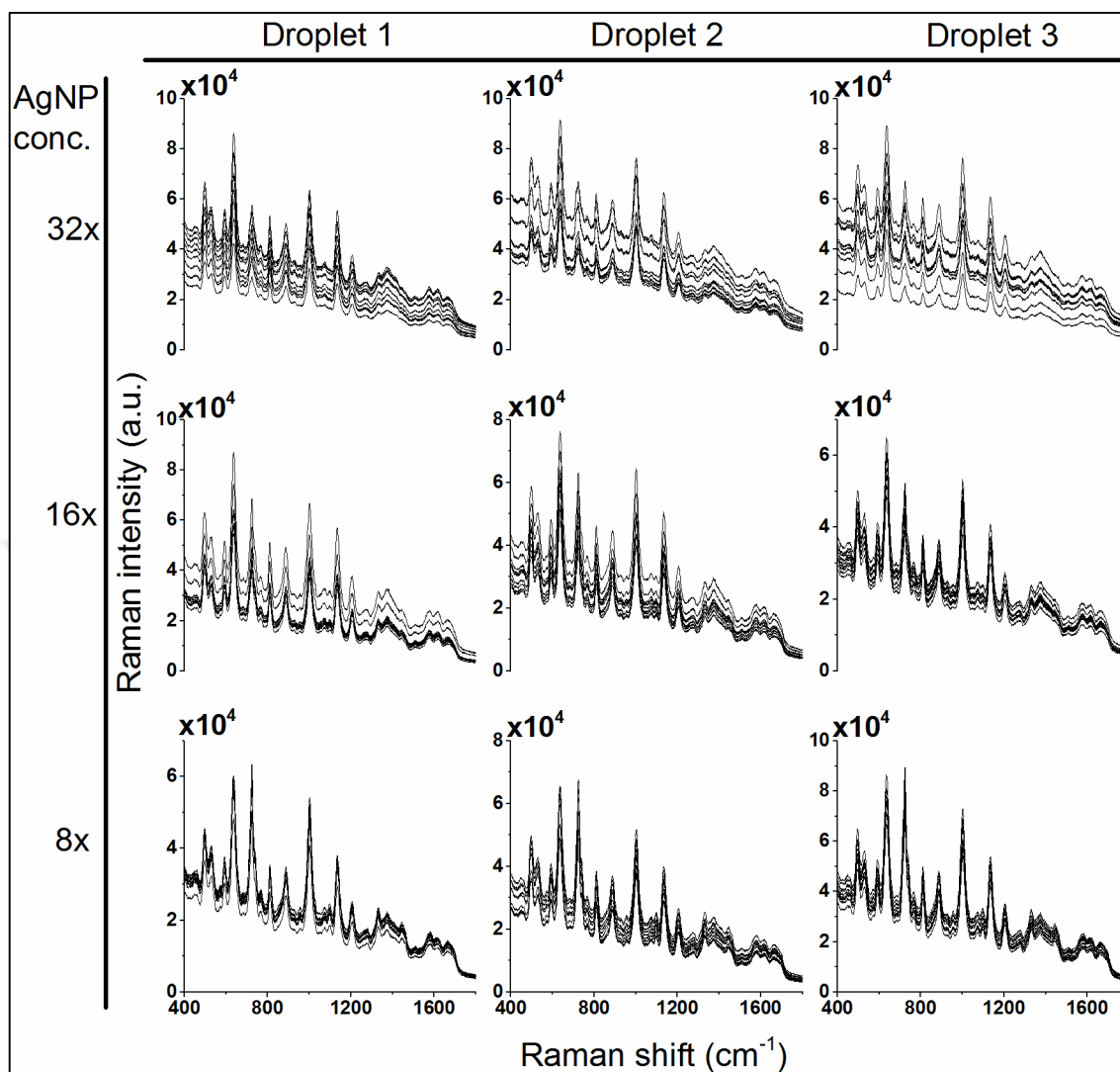


Figure 4.24. Raw SERS spectra of three dried droplets of filtered serum samples with different AgNP concentrations (32x, 16x, 8x).

Reproducibility experiments showed that 32x and 8x AgNP concentrations could be used for whole serum-SERS studies. In order to reach a final decision, intensity distributions within the dried droplets of the mixtures with the two AgNP concentrations were analyzed (Figure 4.26). Deposits had a doughnut shape due to protein content swept to the peripheries during drying. 600 μm X 600 μm regions in the middle region of the droplets were mapped with 5 μm step sizes and intensity distribution of 638 cm^{-1} peak was shown as heat maps. It is seen in the figure that intensity distributions were fairly uniform for the mixtures containing 32x and 8x AgNP colloid.

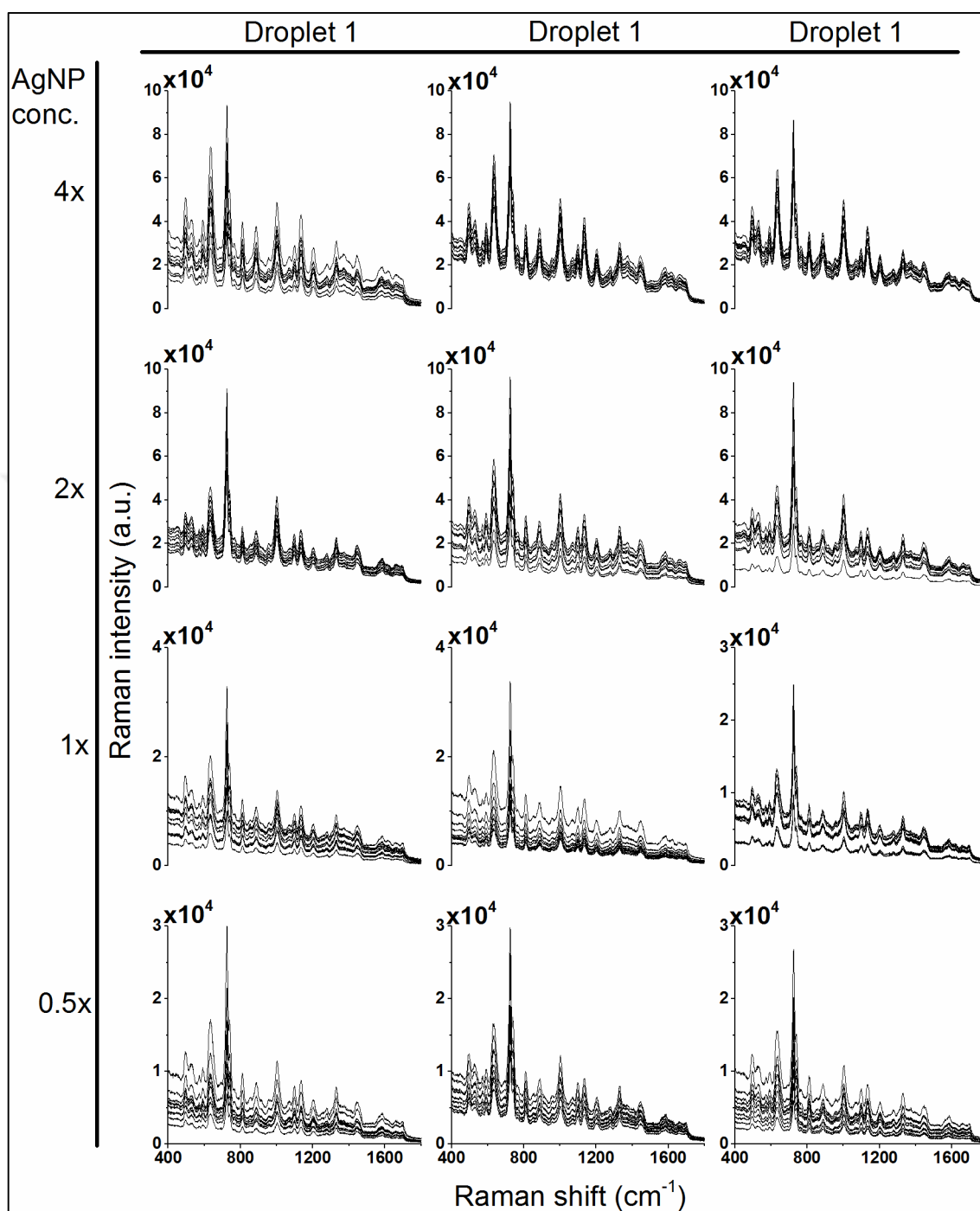


Figure 4.25. Raw SERS spectra of three dried droplets of filtered serum samples with different AgNP concentrations (4x, 2x, 1x, 0.5x).

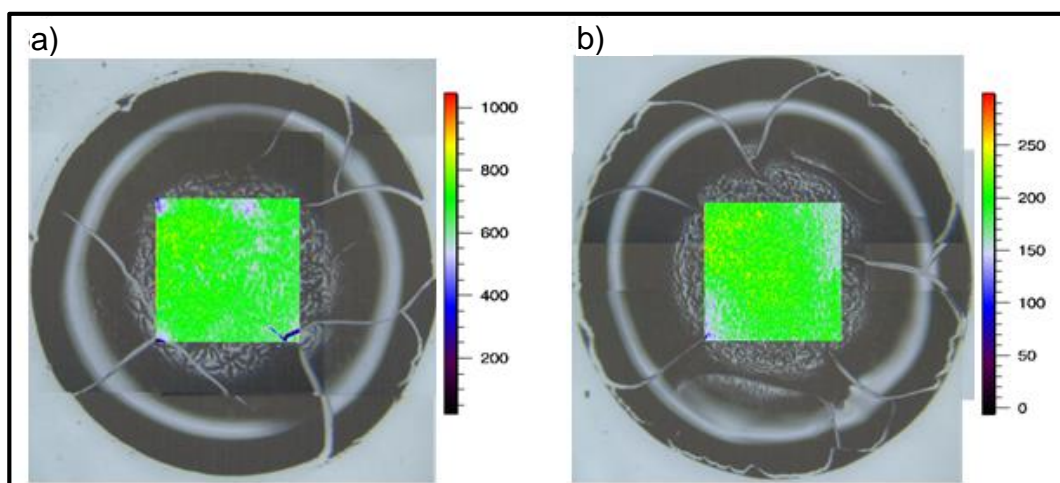


Figure 4.26. Mapping the middle of dried droplets of mixtures of protein and (a) 32x AgNP, (b) 8x AgNP. Heat map of the intensity of 638 cm^{-1} .

Apart from the reproducibility evaluations of the spectra of samples obtained by simple mixing of AgNP colloid with unfiltered and filtered serum, SERS spectra of the serum samples obtained after extraction of proteins with methanol were also acquired and compared to that of unfiltered and filtered serum. Figure 4.27 shows the effects of serum to methanol ratio (v/v) for extraction on the final shape of the SERS spectra of serum. Final AgNP colloid concentrations in the dried droplets were 16x. SERS intensity of the spectrum of the sample obtained with 1:1 serum to methanol extraction was low because of the protein presence. On the other hand, SERS spectral patterns of the other samples were about the same.

In Figure 4.28, SERS spectra of whole serum, filtered serum, and serum after methanol extraction (1:4 serum to methanol ratio) were compared. Although they have common bands, spectral patterns were different due to ingredient loss after filtration and methanol extraction. Filtration is expensive (price of a 0.5 ml filters with three kDa cut-off is around 5€) and methanol extraction brings additional procedures. Therefore, simple mixing of serum with AgNPs and drying on a CaF_2 slide for SERS acquisition was preferred as the method for discrimination of serum samples of cancer patients from that of healthy people.

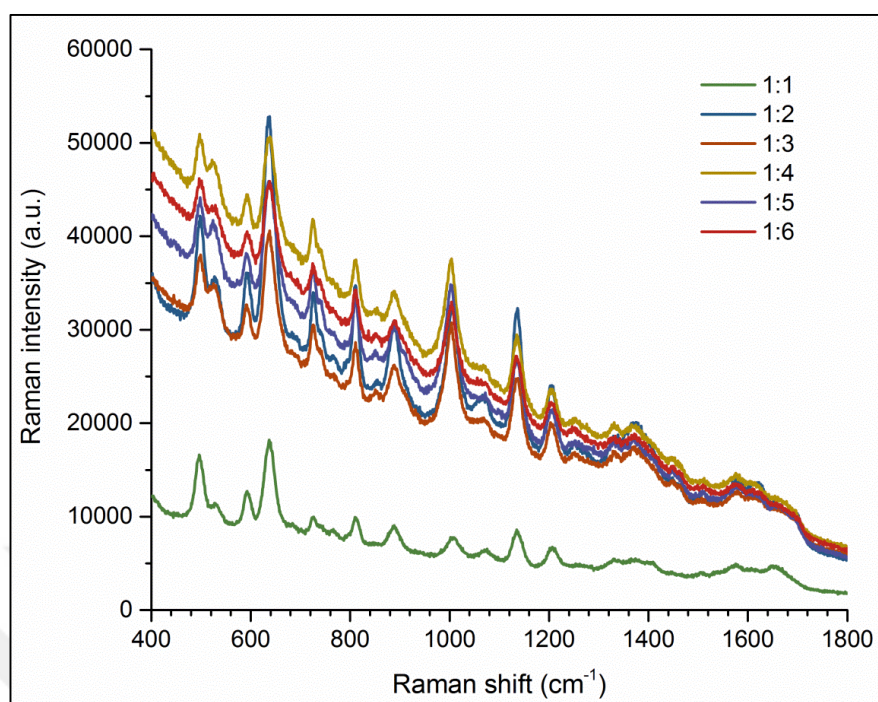


Figure 4.27. SERS spectra of serum after methanol extraction with different serum to methanol ratios (v/v).

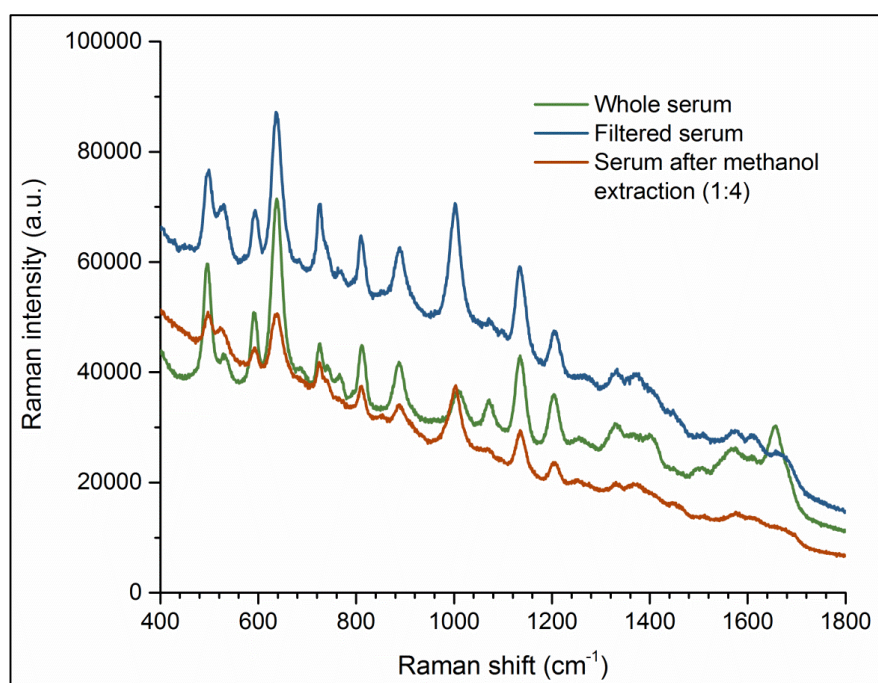


Figure 4.28. Comparison of the SERS spectra of whole serum, filtered serum, and serum after methanol extraction.

4.3.2. On the Origins of Serum SERS Spectra

When I checked the published articles about SERS spectra of blood serum, I realized that SERS band assignments for both serum and plasma mostly rely on earlier Raman spectra reports of tumor tissues and biological molecules. On the other hand, it is well-known among SERS community that Raman spectra and SERS spectra of biological structures are different. Therefore, band assignment for SERS spectra of any material of interest should be done by SERS acquisition of the molecules in that material. Thus far, only one article has discussed weight of the bands of two molecules (i.e., uric acid and hypoxanthine) on serum SERS spectra [95]. In order to fill this gap, SERS spectra of some molecules reported in literature which are thought to have influence on spectral shape of serum were acquired first (Figure 4.29). In addition, SERS spectra of some purine derivatives such as adenine, xanthine, and guanine were also obtained. Final concentration of the molecules was one mM after mixing with 64x AgNP, which is much higher value than their physiological concentrations in serum. It is clearly seen in Figure 4.29 that only tyrosine, tryptophan, and phenylalanine could be able to change spectral shape among amino acids samples. Histidine could make partial contribution but most of the bands were still of the citrate molecules on the surface of AgNPs. Urea and mannose could not make any significant change on the spectral shape. For urea, the only difference was the emergence of band around 1000 cm^{-1} . On the other hand, nucleobases (adenine, thymine, cytosine, and guanine) completely showed their SERS bands, along with purine derivatives xanthine and hypoxanthine. Considering these results, it was inferred that if a molecule at this high concentration could not show its SERS bands when it was mixed with AgNPs, then, it was very unlikely that it could contribute to spectral shape of serum. In order to prove this, the same molecules were spiked into commercial human serum at the same concentration (one mM) and their spectra were acquired (Figure 4.30). This time, none of the amino acids could make any change on the spectral shape of whole serum. Urea and mannose also could not make contributions as expected. In most of the articles, mannose has been reported as the reason for 1095 cm^{-1} and 1135 cm^{-1} bands, but it was shown here that it was not probable. Among nucleobases, cytosine and guanine added some bands to the serum spectra, and which means that they could contribute to the serum spectrum if their concentration in blood changes significantly. Effects of the xanthine presence were more

evident than cytosine and guanine. Lastly, it can be said that hypoxanthine and adenine completely changes spectral shape of serum.

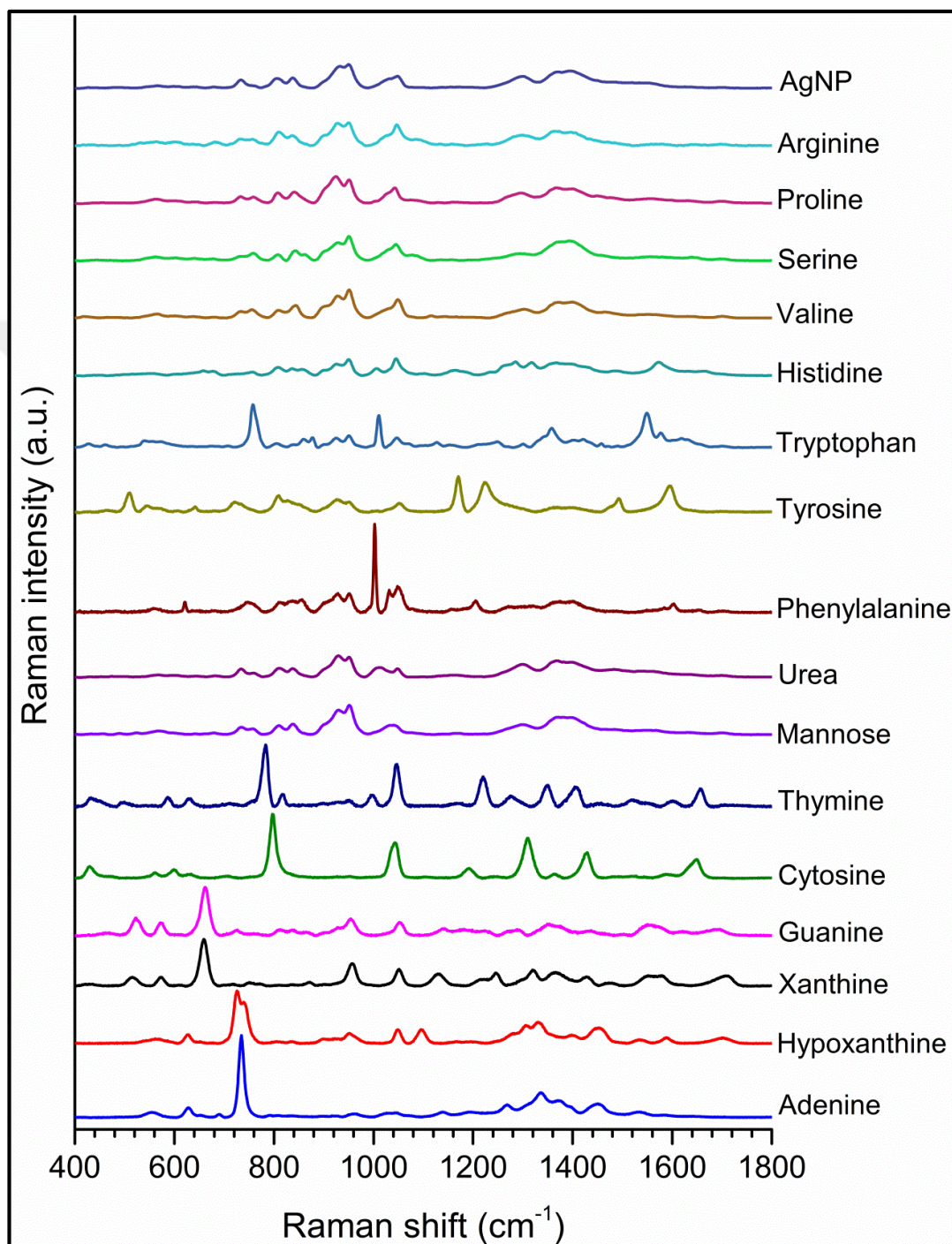


Figure 4.29. SERS spectra of some molecules found in blood serum and SERS spectrum of AgNP.

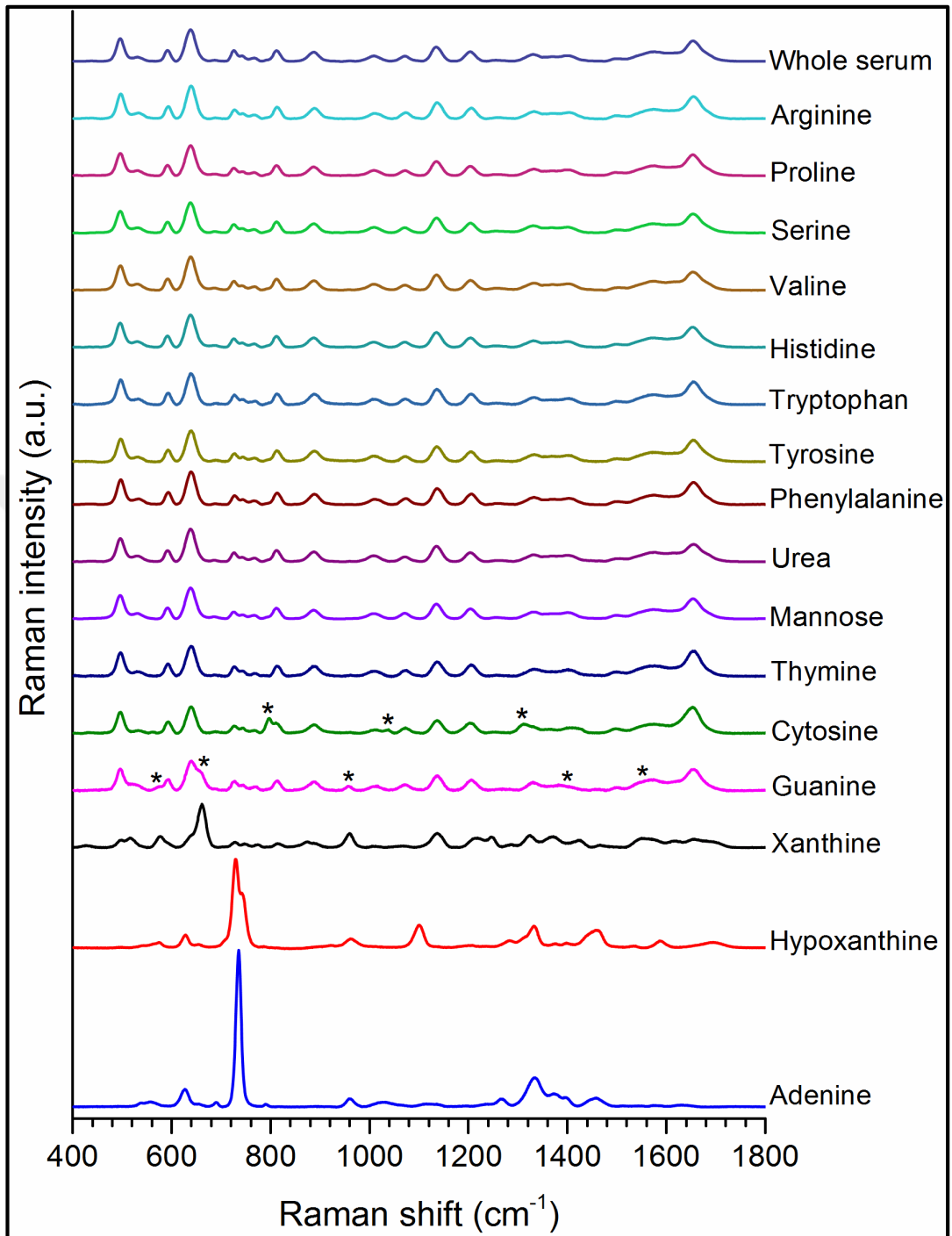


Figure 4.30. SERS spectra of whole serum after spiking some molecules found in blood serum. Star symbol indicates the bands contributed to the serum SERS spectrum by the spiked metabolites.

According to the Serum Metabolome Database (<http://www.serummetabolome.ca/>) and a related article [125], there are at least 4651 small molecule metabolites in serum. Regarding proteins, as of 2014, plasma levels of more than one hundred proteins have been estimated [126]. As the numbers are considered, it is obvious that many metabolites and proteins possessing affinity to the silver compete with each other to interact with AgNP surface after serum and AgNP colloid mixing. At low AgNP concentrations, molecules possessing higher affinity bind to AgNP surface. Other molecules gain opportunity to bind as the AgNP concentration is increased. Therefore, at each AgNP concentration, the number and type of molecules under impinging laser changes, resulting in different spectral outcomes. Monitoring changes in spectral shape can be extremely useful to be able to elucidate the origins of SERS spectra of complex biofluids. Comparing intensity and patterns of the SERS bands at different AgNP concentrations, better band assignments can be done. To the best of our knowledge, this kind of approach to this matter will be the first time in literature. Figure 4.31 shows SERS spectra of whole serum (WS) and filtered serum (FS) at four different AgNP concentrations. Uric acid and hypoxanthine spectra were also added to the figure because they have some common bands with serum. At first glance, it was seen that there were dramatic pattern differences among spectra collected using different AgNP concentrations. For example, intensity of the band at 638 cm^{-1} increased but intensity of the 725 cm^{-1} band decreased with each two fold AgNP concentration increase for both WS and FS. Along with the increase in 638 cm^{-1} peak, intensity of 495 cm^{-1} , 530 cm^{-1} , 1134 cm^{-1} and 1204 cm^{-1} bands increased slightly. On the contrary, intensity of 1330 cm^{-1} and 1452 cm^{-1} decreased. Comparing these changes to the spectra of uric acid and hypoxanthine, it could be said that uric acid features replaced hypoxanthine features with AgNP concentration increase. On the other hand, differences in other bands between serum and these two purine derivatives (1008 cm^{-1} , 1370 cm^{-1} , 1670 cm^{-1}) let us conclude that they were major determinants but not the only determinants in the final shape of the serum spectrum. Moreover, the width of 638 cm^{-1} band was different in uric acid spectrum than serum spectra, and this revealed the effects of some unknown molecules to the spectral shape. We can attribute 725 cm^{-1} band in serum spectrum to hypoxanthine, because of the presence of a shoulder centered at 744 cm^{-1} . Hypoxanthine has ketonic and enolic forms. At low pH values, it is in ketonic form, and therefore, only 725 cm^{-1} peak can be observed. On the other hand, at high pH values, hypoxanthine gets

enolic form and only 744 cm^{-1} is observable. At physiological pH values, both forms coexist, and we see both bands.

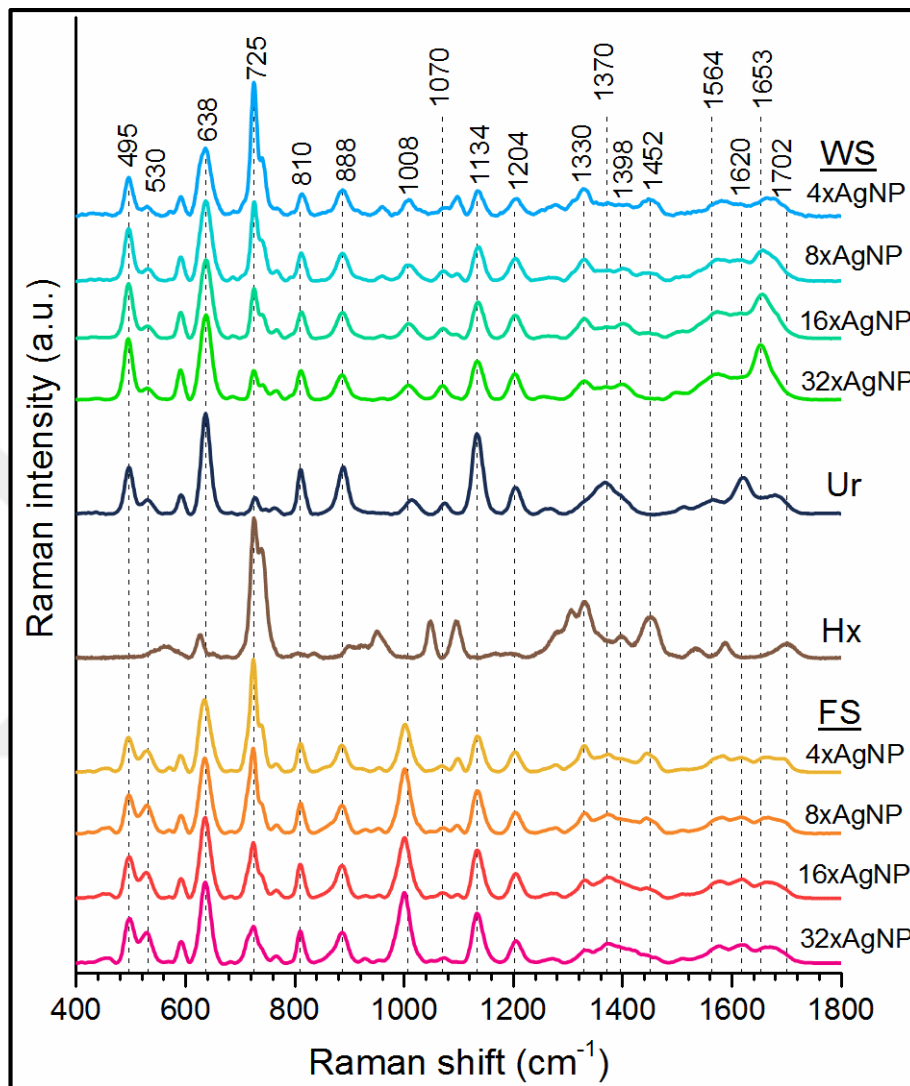


Figure 4.31. Comparison of the SERS spectra of uric acid (Ur), hypoxanthine (Hx), and whole serum (WS) and filtered serum (FS) with different AgNP concentrations.

Further examination of Figure 4.31 shows the spectral differences between WS and FS. Differences in the ratio of 495 cm^{-1} and 530 cm^{-1} bands, intensity of 1008 cm^{-1} band, and shape of $1250\text{--}1500\text{ cm}^{-1}$ and $1500\text{--}1750\text{ cm}^{-1}$ regions can be seen at first sight. In addition, 1008 cm^{-1} band was shifted to 1001 cm^{-1} . These differences show the importance of proteins on the final shape of whole serum spectrum. Proteins create molecular crowding on AgNP surface and can cause orientation changes of molecules on AgNP surface.

In addition some proteins bind to AgNP surface and increase the level of competition for AgNPs.

The effects of proteins on serum SERS spectra were studied further by using three different model proteins (Figure 4.32). Human serum albumin (HSA) is the most abundant protein and transferrin (Trf) is the third abundant protein in blood serum. Lysozyme (Lys) has overall positive charge at physiological pH (pI:11.3), therefore it was chosen to be a model for positively charged proteins in serum. Total protein concentration in serum is in the range of 60-85 mg/ml. In order to mimic this concentration value and to be able to monitor spectral changes due to protein concentration change, proteins were spiked at a maximum of 40 mg/ml concentration to filtered serum (Please note that this value lowers to 20 mg/ml upon mixing with 64x AgNPs as shown in the figure). When the spiked protein concentrations were 1 mg/ml, spectra were similar to FS. A five-fold increase in protein concentrations resulted in significant spectral changes. On the other hand, there were some small differences among HSA, Trf, and Lys spiked serum spectra reflecting effects of protein type. After a further four-fold increase, spectra of protein spiked filtered serum samples became extremely similar to spectrum of whole serum acquired using 32x AgNP (final concentration) regardless of protein type.

4.3.3. SERS Study of Purines and Purine Derivatives

In the previous section, it was stated that purines and purine derivatives had effects on the final shape of the SERS spectrum of serum. Therefore, in this section, more detailed analysis was performed on the SERS spectra of purines and purine derivatives. When Figure 4.31 is reviewed, it is observed that serum spectrum has features of uric acid spectrum. Therefore, uric acid was the first molecule to study. Powder form of uric acid was dissolved in one molar of NaOH to make a stock solution and diluted in phosphate buffered saline (PBS). pH of the solution was adjusted with HCl. PBS is widely used buffer for cell culture applications. Its osmolarity is the same with osmolarity of the human body. Therefore, to mimic aqueous part of serum (i.e., water plus some ions in serum), PBS was wanted to be used for SERS studies of purines and purine derivatives. On the other hand, SERS spectrum of dried droplet of uric acid (350 μ M -average concentration of uric acid in human serum-) could not be acquired at physiological pH.

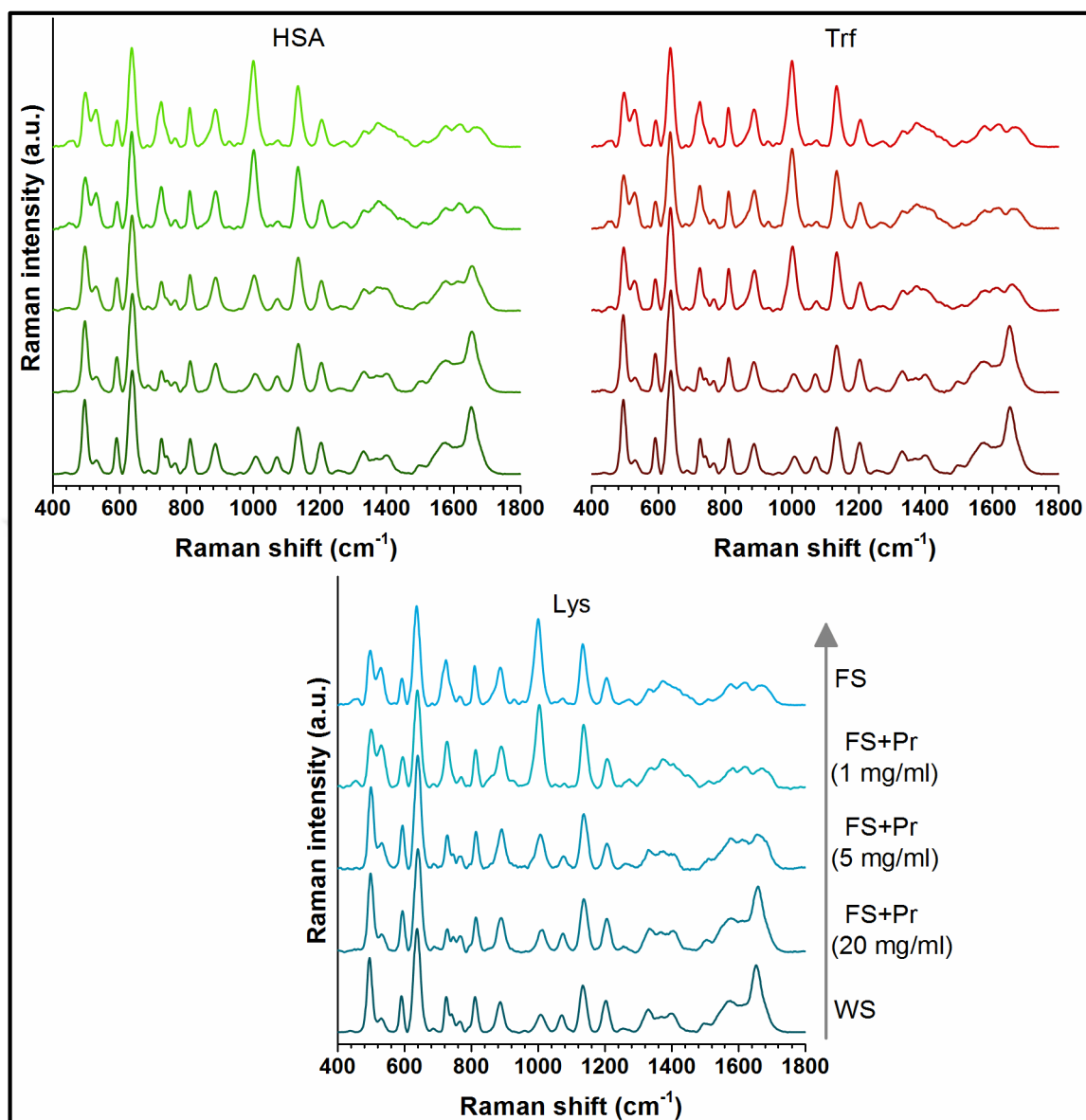


Figure 4.32. Changes in SERS spectrum of free serum (FS) when different concentrations of human serum albumin (HSA), transferrin, and lysozyme (Lys) are spiked. Pr denotes protein. FS+Pr (1 mg/ml) denotes free serum containing protein at 1 mg/ml concentration after mixing with AgNP colloid. Final concentration of AgNP colloid in the mixtures is

32x.

The reasons for this could be uric acid solubility and its poor interaction with AgNPs or phosphate buffer or saline in the buffer. The use of phosphate buffer without saline did not result in acquisition of an informative, quality spectrum. Therefore, it was concluded that phosphate buffer was not a suitable buffer for SERS study of dried droplets of uric

acid. Pure water was also used to dilute stock uric acid solution, and HCl was used to adjust pH. That time, again, good quality spectrum could not be obtained. Then, the experiment was continued with acquisition of SERS spectrum of uric acid from droplets without any drying procedure. Figure 4.33 shows that saline was required to obtain a quality spectrum of uric acid when pH was 12. Salt triggers nanoparticle aggregation leading to formation of hot spots (the more the hot spots are present in laser illuminated area, the stronger the SERS signals are acquired). SERS spectra of uric acid in PBS at different pH values were also acquired. It was observed that SERS spectrum of uric acid became weaker as the pH lowers (Figure 4.34). As a consequence, it was concluded that phosphate buffer was not a suitable buffer for SERS study of liquid droplets of uric acid at physiological pH.

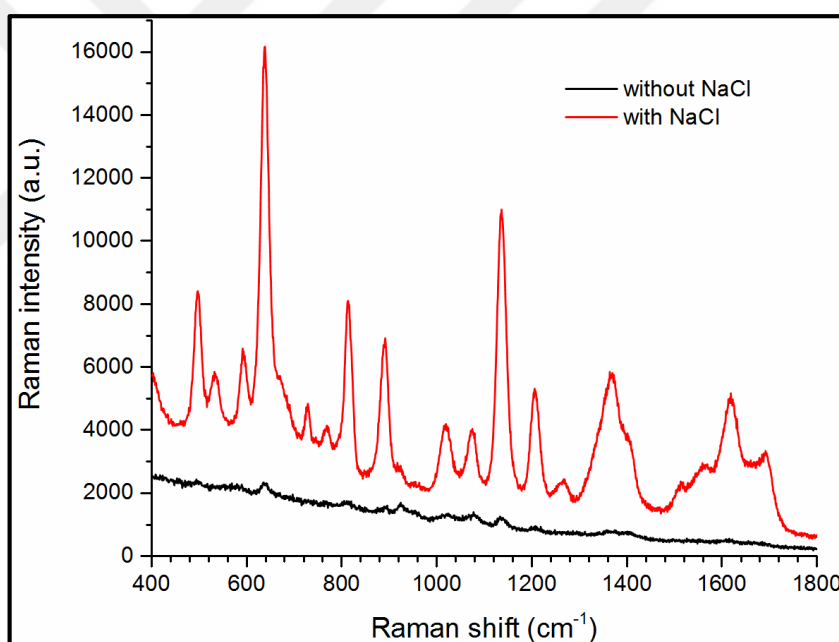


Figure 4.33. SERS spectra of uric acid in phosphate buffer (pH 12, without NaCl) with and without NaCl.

Instead of PBS buffer, borate buffer at pH 8.4 was used. The results can be seen in Figure 4.35. With the addition of NaCl, intense spectrum of uric acid could be obtained. In order to understand borate buffer interference to the spectra, SERS spectra of borate buffer at different concentrations were acquired (Figure 4.36). There was not any spectral difference, meaning, there was not any borate buffer interference. Next time, NaCl was

added in order to be sure about buffer interference issue. Addition of NaCl did not cause any signals stemming from borate buffer (Figure 4.37).

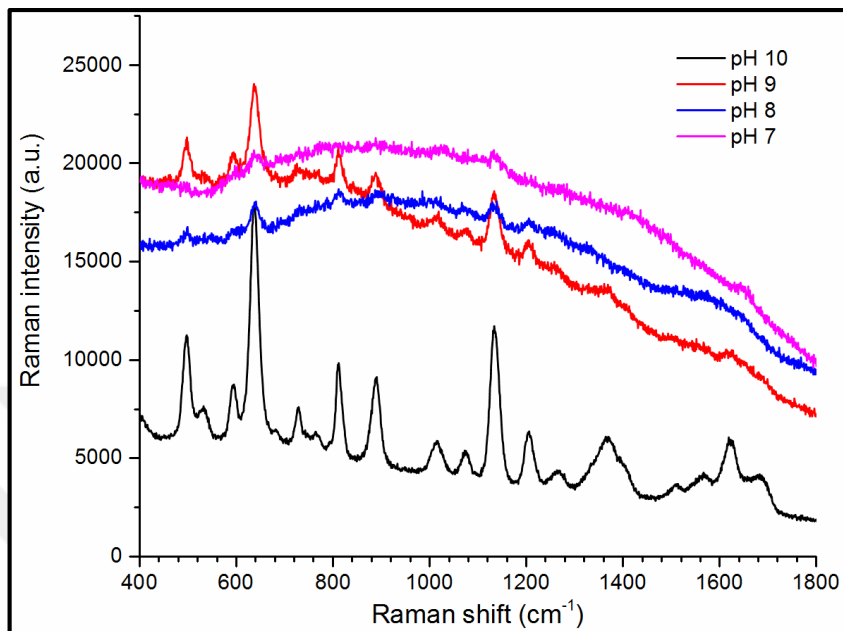


Figure 4.34. SERS spectra of uric acid in PBS at different pH values.

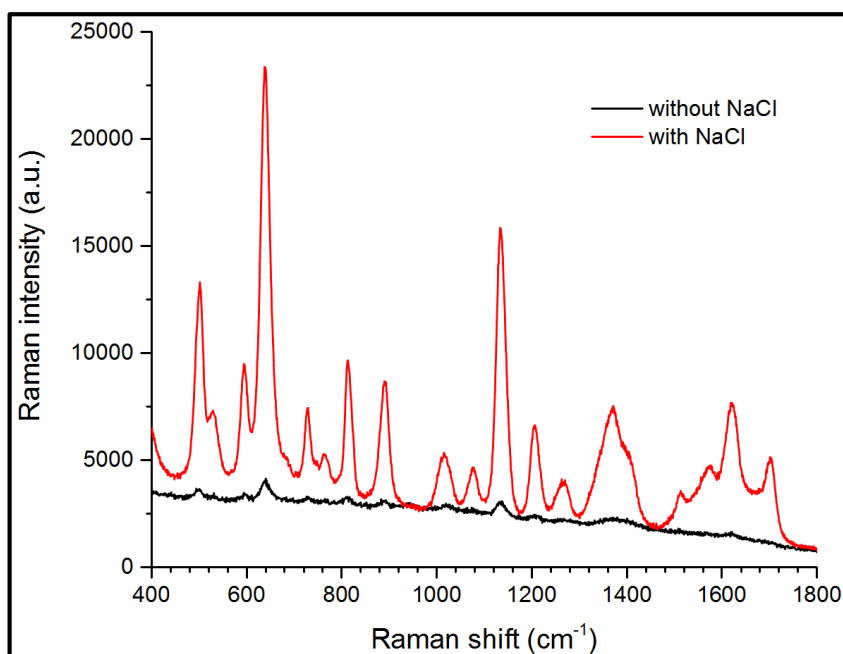


Figure 4.35. SERS spectra of uric acid in 10 mM borate buffer (pH 8.5) with and without NaCl.

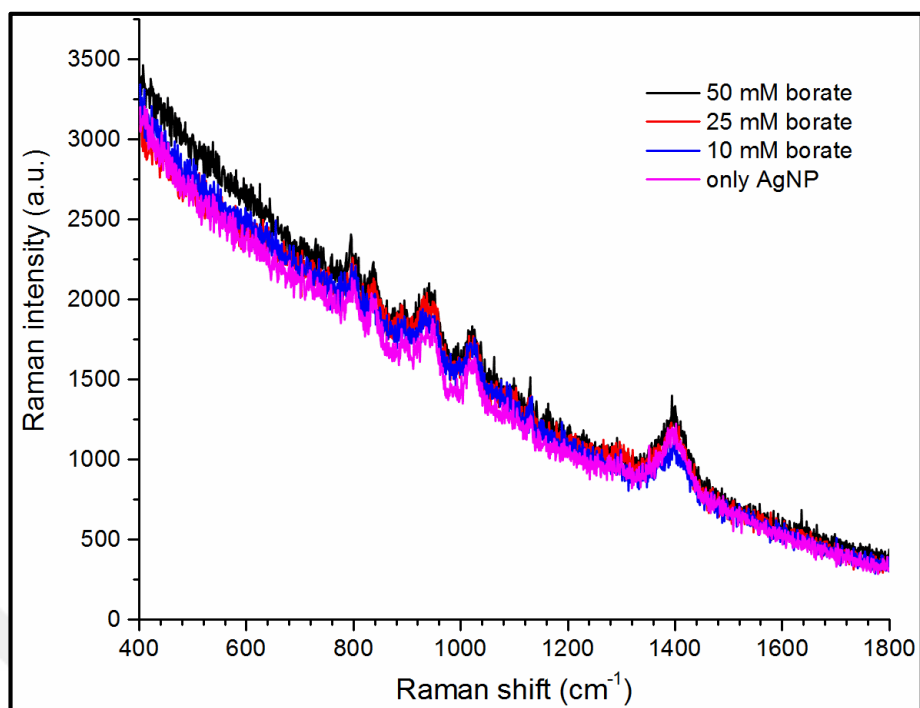


Figure 4.36. SERS spectra of borate buffer at different borate concentrations.

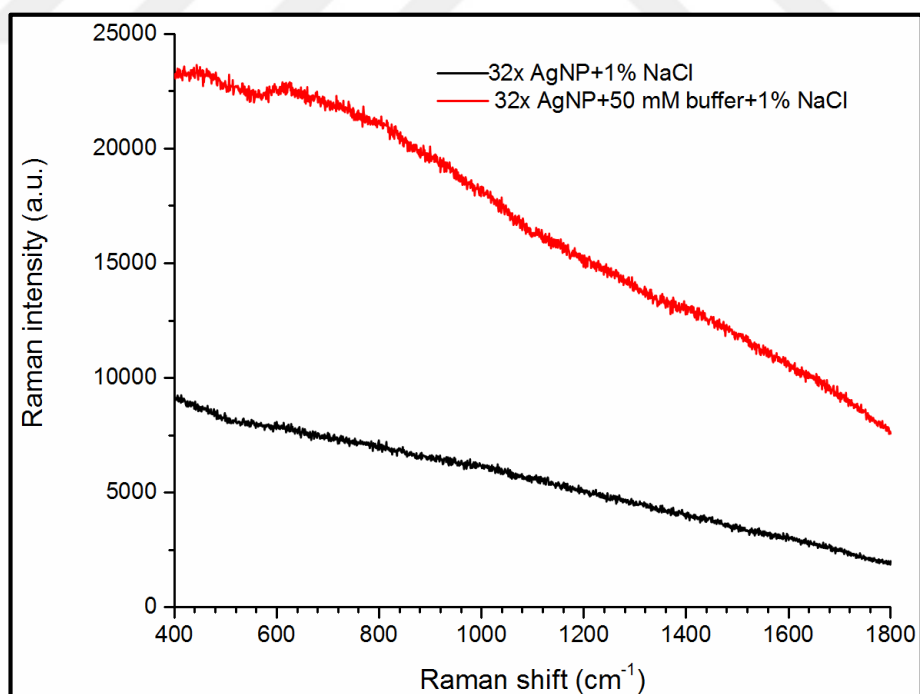


Figure 4.37. SERS spectra of AgNPs in the presence of one percent NaCl and 50 mM borate buffer plus one percent NaCl.

After uric acid study, SERS spectra some blood purines and purine derivatives were examined (Figure 4.38-47). SERS spectra of these molecules were studied at two different AgNP concentration in order to understand the effects of AgNP concentration on their SERS spectra. In addition SERS spectra of binary mixtures of these molecules were also studied in order to understand molecule's relative SERS spectral dominance in the presence of the other molecule, and to understand the effect of AgNP concentration on this issue. When the figures are examined, it is seen that the spectra of single molecules are slightly changed due to AgNP concentration. This could be explained as orientation difference of molecules on silver surfaces due to AgNP concentration difference. SERS spectra of adenine and guanine mixture were dominated by adenine at two AgNP concentrations (Figure 4.38). Slight differences can be explained by either orientation difference and competition of both molecules for silver surface.

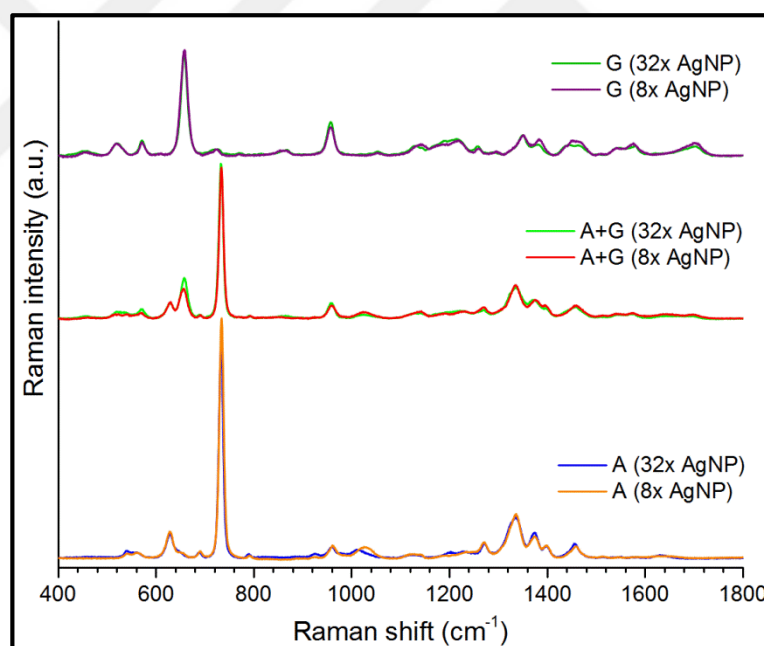


Figure 4.38. SERS spectra of adenine, guanine and their mixtures at 8x and 32x AgNP concentrations.

SERS spectra of adenine and hypoxanthine mixture were dominated by adenine at two AgNP concentrations (Figure 4.39). Slight differences can be explained by either orientation difference and competition of both molecules for silver surface.

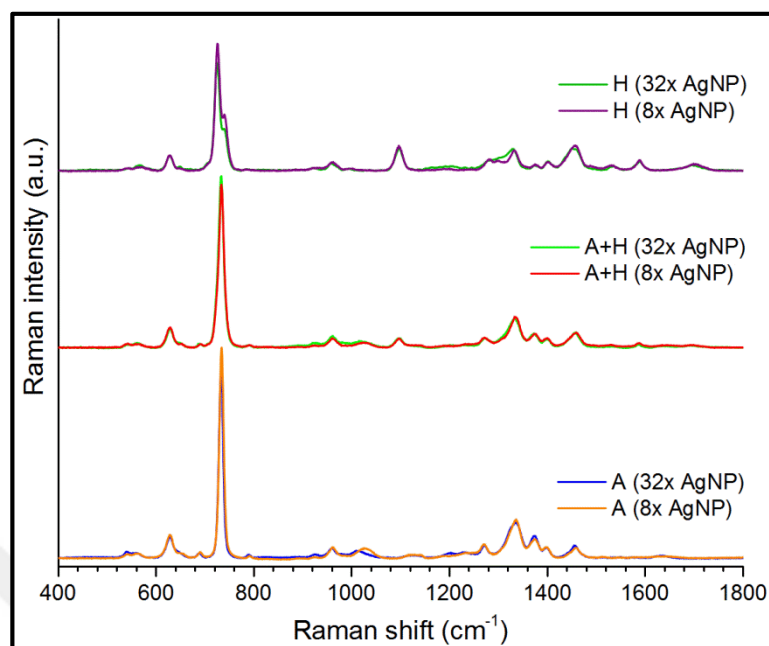


Figure 4.39. SERS spectra of adenine, hypoxanthine and their mixtures at 8x and 32x AgNP concentrations.

SERS spectra of adenine and uric acid mixture were dominated by adenine at two AgNP concentrations (Figure 4.40). Slight differences can be explained by either orientation difference and competition of both molecules for silver surface. The similar phenomenon occurred with adenine and xanthine mixture. SERS spectra of adenine and xanthine mixture were dominated by adenine at two AgNP concentrations (Figure 4.41). Slight differences can be explained by either orientation difference and competition of both molecules for silver surface.

SERS spectra of guanine and uric acid mixture at two AgNP concentrations were different (Figure 4.42). With 8x AgNP, spectrum was more guanine like. When AgNP concentration was increased, spectrum became a mixture of the spectra of each two molecules. Guanine interacts better than uric acid with AgNPs. At low AgNP concentration, silver surface was mostly covered by guanine. When AgNP concentration was increased, uric acid could cover the extra nanoparticle surface. SERS spectra of guanine and xanthine mixture was a mixture of the SERS spectra of each molecules at two AgNP concentrations (Figure 4.43). Slight differences can be explained by either orientation difference and competition of both molecules for silver surface.

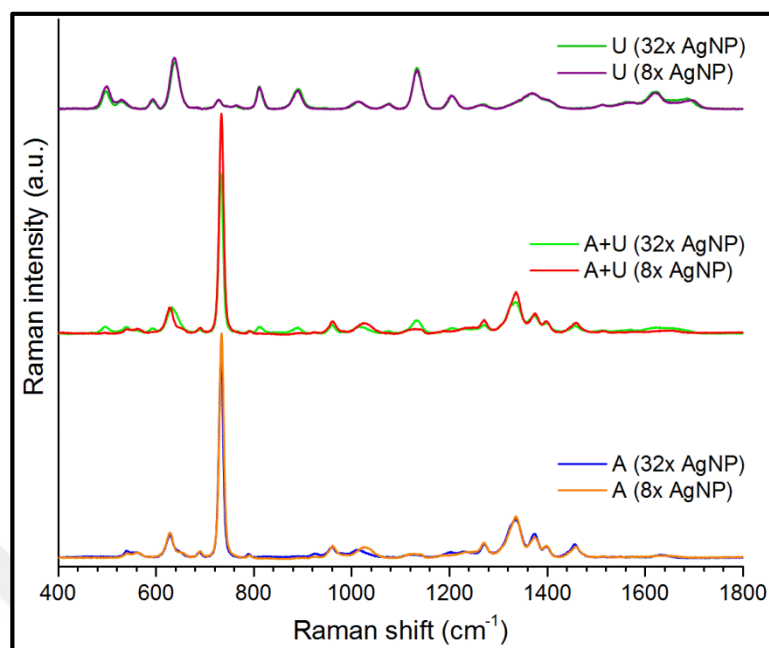


Figure 4.40. SERS spectra of adenine, uric acid and their mixtures at 8x and 32x AgNP concentrations.

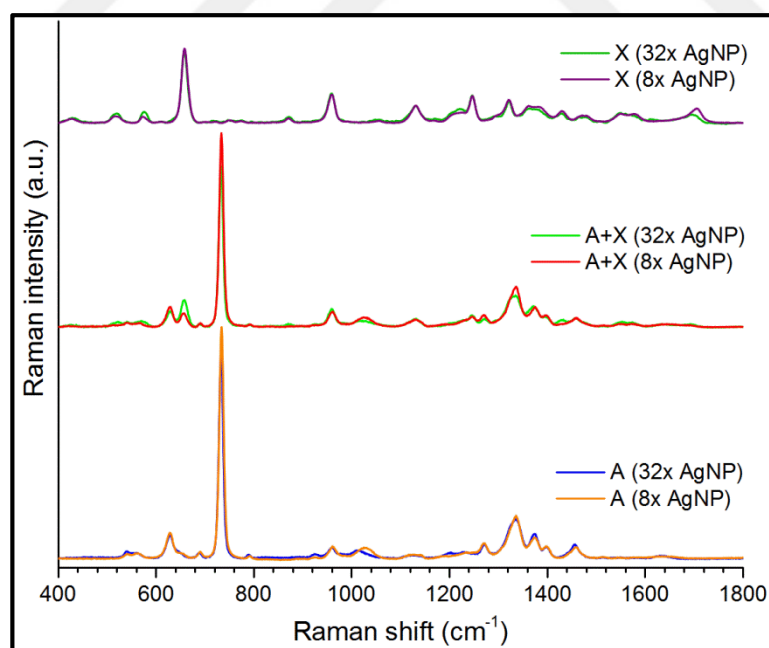


Figure 4.41. SERS spectra of adenine, xanthine and their mixtures at 8x and 32x AgNP concentrations.

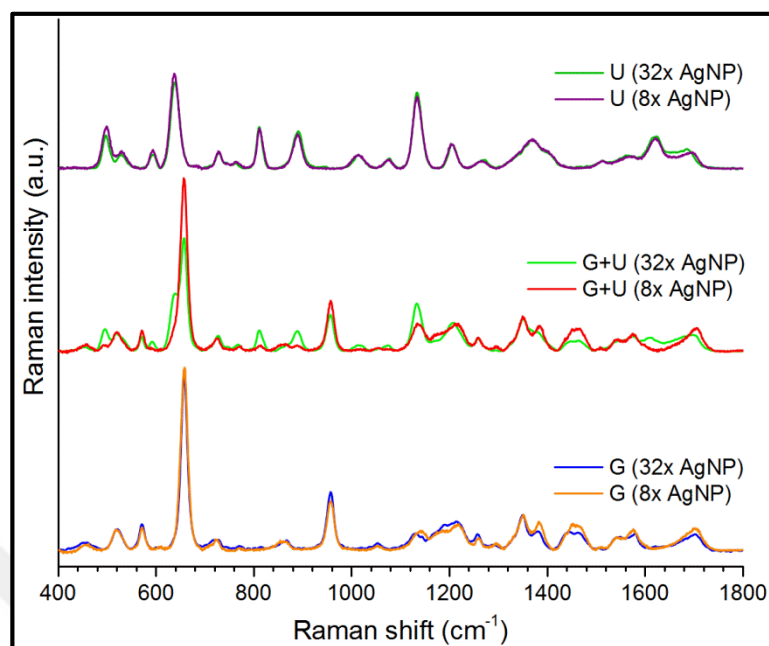


Figure 4.42. SERS spectra of uric acid, guanine and their mixtures at 8x and 32x AgNP concentrations.

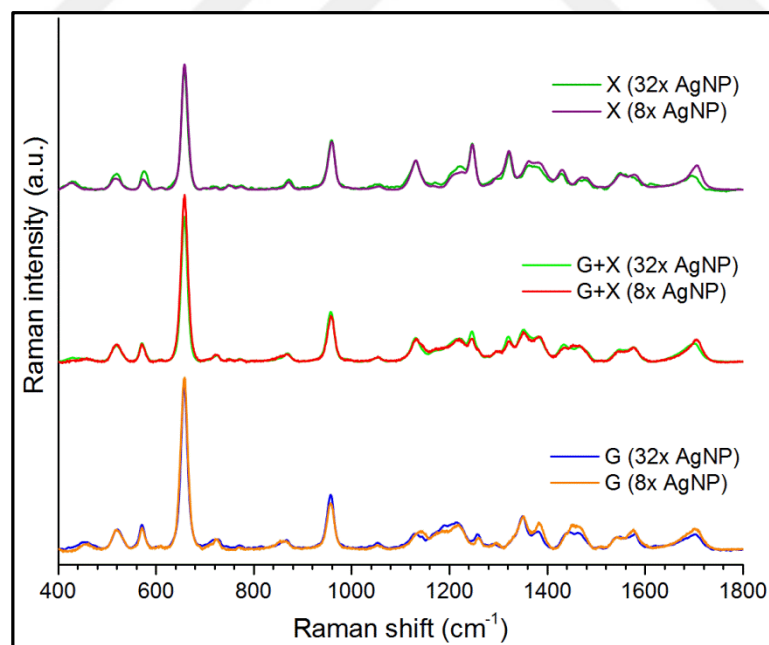


Figure 4.43. SERS spectra of guanine, xanthine and their mixtures at 8x and 32x AgNP concentrations.

SERS spectra of guanine and hypoxanthine mixture at two AgNP concentrations were similar (Figure 4.44). Both spectra contained SERS bands of both molecules.

SERS spectra of hypoxanthine and uric acid mixture at two AgNP concentrations were different (Figure 4.45). With 8x AgNP, spectrum was more hypoxanthine like. When AgNP concentration was increased, spectrum became a mixture of the spectra of each two molecules. Hypoxanthine interacts better than uric acid with AgNPs.

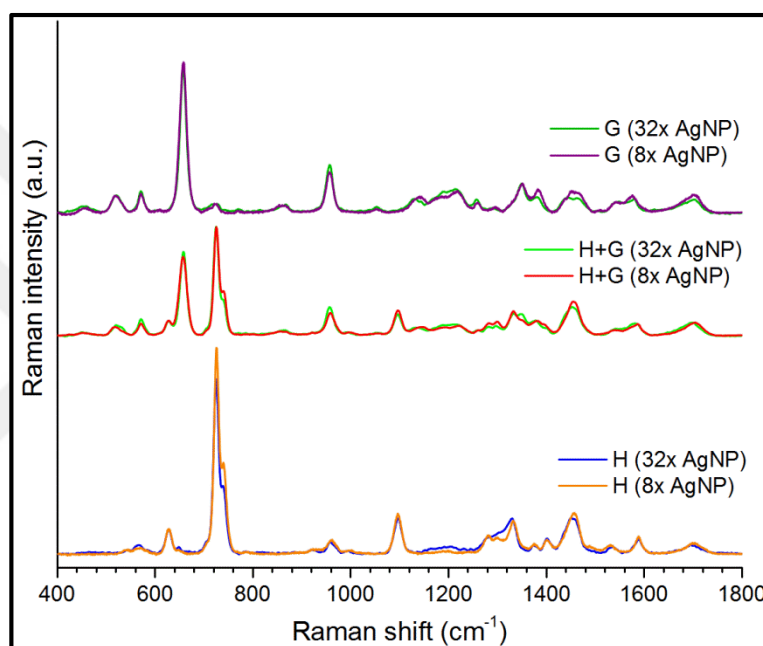


Figure 4.44. SERS spectra of guanine, hypoxanthine and their mixtures at 8x and 32x AgNP concentrations.

SERS spectra of xanthine and hypoxanthine mixture at two AgNP concentrations were similar (Figure 4.46). Spectral shape contained SERS bands of both molecules. Slight differences can be explained by either orientation difference and competition of both molecules for silver surface.

SERS spectra of xanthine and uric acid mixture at two AgNP concentrations were different (Figure 4.47). With 8x AgNP, spectrum was more xanthine like. When AgNP concentration was increased, spectrum became a mixture of the spectra of each two molecules. Xanthine interacts better than uric acid with AgNPs.

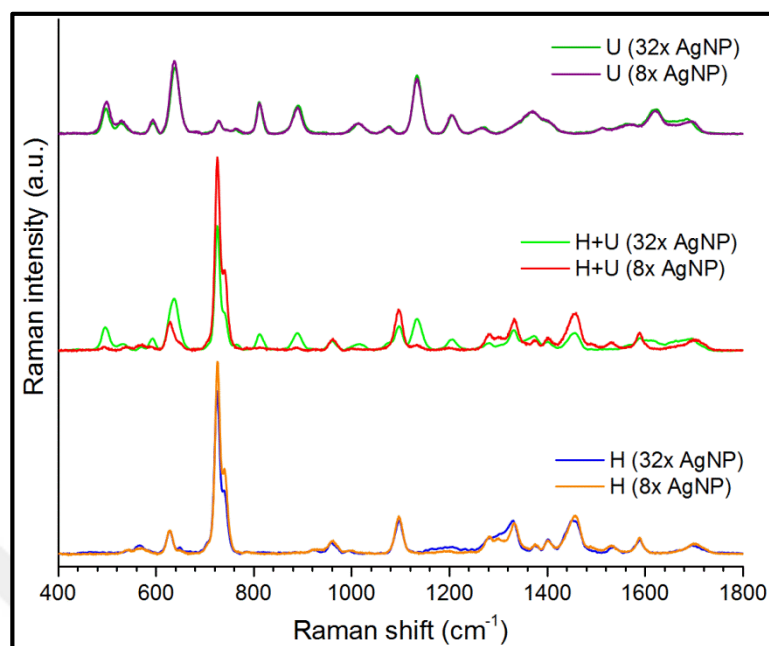


Figure 4.45. SERS spectra of uric acid, hypoxanthine and their mixtures at 8x and 32x AgNP concentrations.

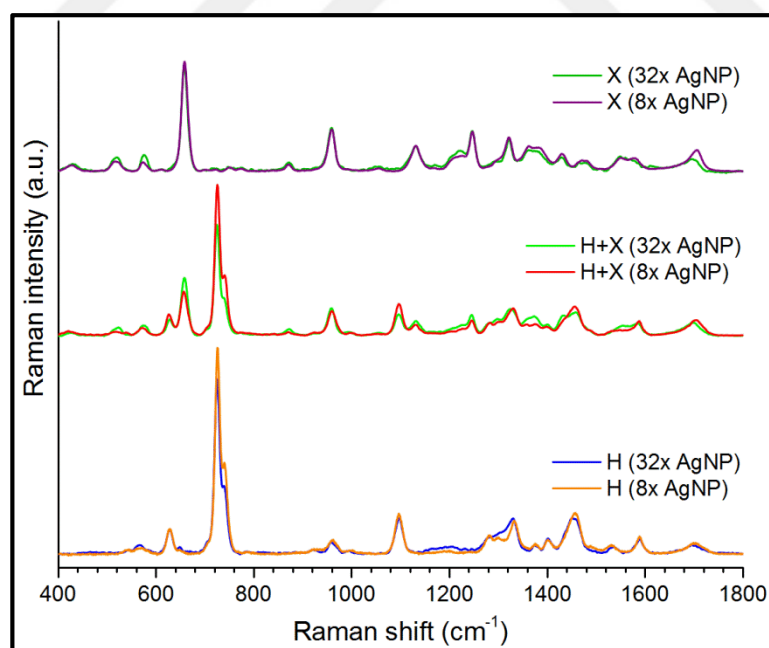


Figure 4.46. SERS spectra of xanthine, hypoxanthine and their mixtures at 8x and 32x AgNP concentrations.

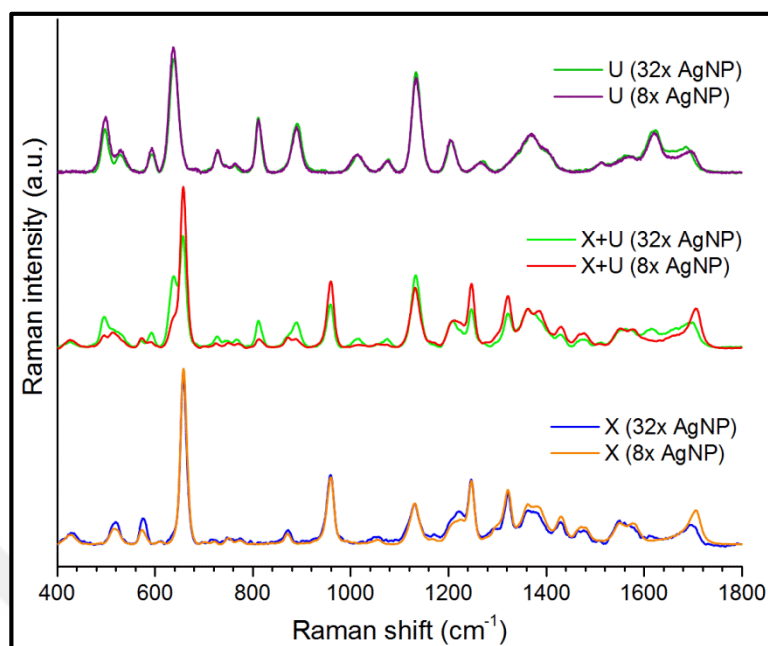


Figure 4.47. SERS spectra of xanthine, uric acid and their mixtures at 8x and 32x AgNP concentrations.

4.3.4. Discrimination of Cancer and Chronic Diseases Using SERS

In the section 4.3.1, it was shown that use of three different AgNP concentrations gave reproducible spectra. On the other hand, in this section, only two AgNP concentrations (32x and 8x) were used because this was sufficient to show the power of SERS for discrimination of cancer group and chronic diseases group and control group. General workflow of this section was like this: After acquisition of the SERS spectra, average spectra of the three groups with their standard deviations were compared. Difference spectra which were obtained subtracting the average control group spectrum from the average cancer group spectrum and chronic disease group spectrum were analyzed. Some SERS bands, of which intensities among three groups may differ, were compared to add depth to the investigation. Then, PLS-DA was performed as multivariate analysis of the collected spectra for classification discrimination of three groups. Finally, permutation tests were performed to be sure that there were not any over-fitting during PLS-DA analysis.

Firstly, SERS spectra of serum samples of 30 cancer patients, 15 patients with chronic disease, and 30 healthy people (as control group) were acquired using 32 times concentrated AgNP colloid (Figure 4.48).

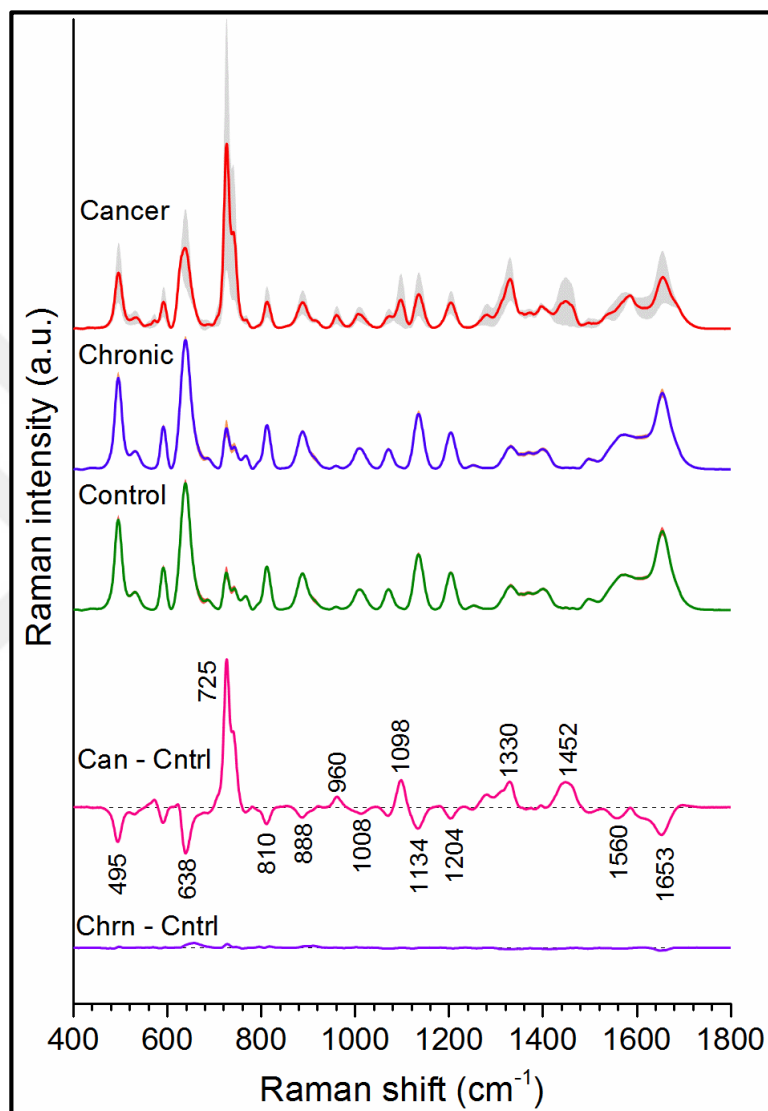


Figure 4.48. Average SERS spectra of serum samples of cancer and chronic disease afflicted patients and healthy subjects obtained using 32x AgNP. Shaded areas around the spectra represent the standard deviations. Bottom two spectra are the difference spectra (Can-Cntrl: Cancer-Control, Chrn-Control: Chronic-Control).

Average spectra had similar features with commercial WS spectra presented in Figure 4.31. Spectra of the control group and chronic disease group were similar to the WS spectrum obtained using 32x AgNP, whereas spectrum of the cancer group was similar to

the WS spectrum obtained using 4x AgNP. It was evident from eight times less AgNP concentration that relative concentrations of the metabolites possessing higher affinity to AgNP surface and of the metabolites possessing larger Raman cross section were higher in the serum of cancer patients. By observing the bands at 725 cm^{-1} , 1330 cm^{-1} , and 1452 cm^{-1} in the difference spectra of cancer and control groups, it could be said that one of these metabolites was hypoxanthine. On the other hand, the decrease in the intensities of the bands at 495 cm^{-1} , 638 cm^{-1} , and 830 cm^{-1} showed the decrease in uric acid concentration relative to the other metabolites in the case of cancer disease. Difference between chronic disease group and control group was small and barely discernible by naked eye at many band positions. Standard deviation of the control group spectra was very low and barely discernible, and so was for chronic disease group. On the other hand, standard deviation of the cancer group spectrum was high. This means that for healthy people and for the chronic diseases studied in this thesis, relative concentrations of the metabolites having impact on serum SERS spectrum was about the same, but for cancer patients, relative concentrations of the serum constituents were quite variable. Detailed comparison of SERS spectra of the three groups was performed by statistical analysis on the intensity values of the eight different SERS bands (Figure 4.49). Firstly, Shapiro-Wilk test was applied to check for normality, and found that intensity distributions of the eight bands of cancer group were not normally distributed. Therefore, Kruskal-Wallis test and Dunn's post hoc test with Bonferroni correction were applied to check whether differences in intensity distributions of the three groups were statistically significant. For the all eight SERS bands, the differences between cancer group and chronic disease group and the differences between cancer group and control group were statistically significant ($p < 0.05$). On the other hand, the differences between chronic disease group and control group were not statistically significant. Of course, since only eight SERS bands does not totally represent whole spectrum, these results did not mean that there was not any difference between the SERS spectra of the control group and the chronic disease group.

Multivariate analyses tools detect subtle differences and variations among spectra, and therefore very useful for discrimination purposes. PLS-DA analysis of SERS spectra of cancer patients and control patients was performed with leave-one-out cross validation, and scores plot were drawn (Figure 4.50). In the figure, y-axis was named as "Y CV Predicted" which means PLS-DA scores of each spectrum after cross validation.

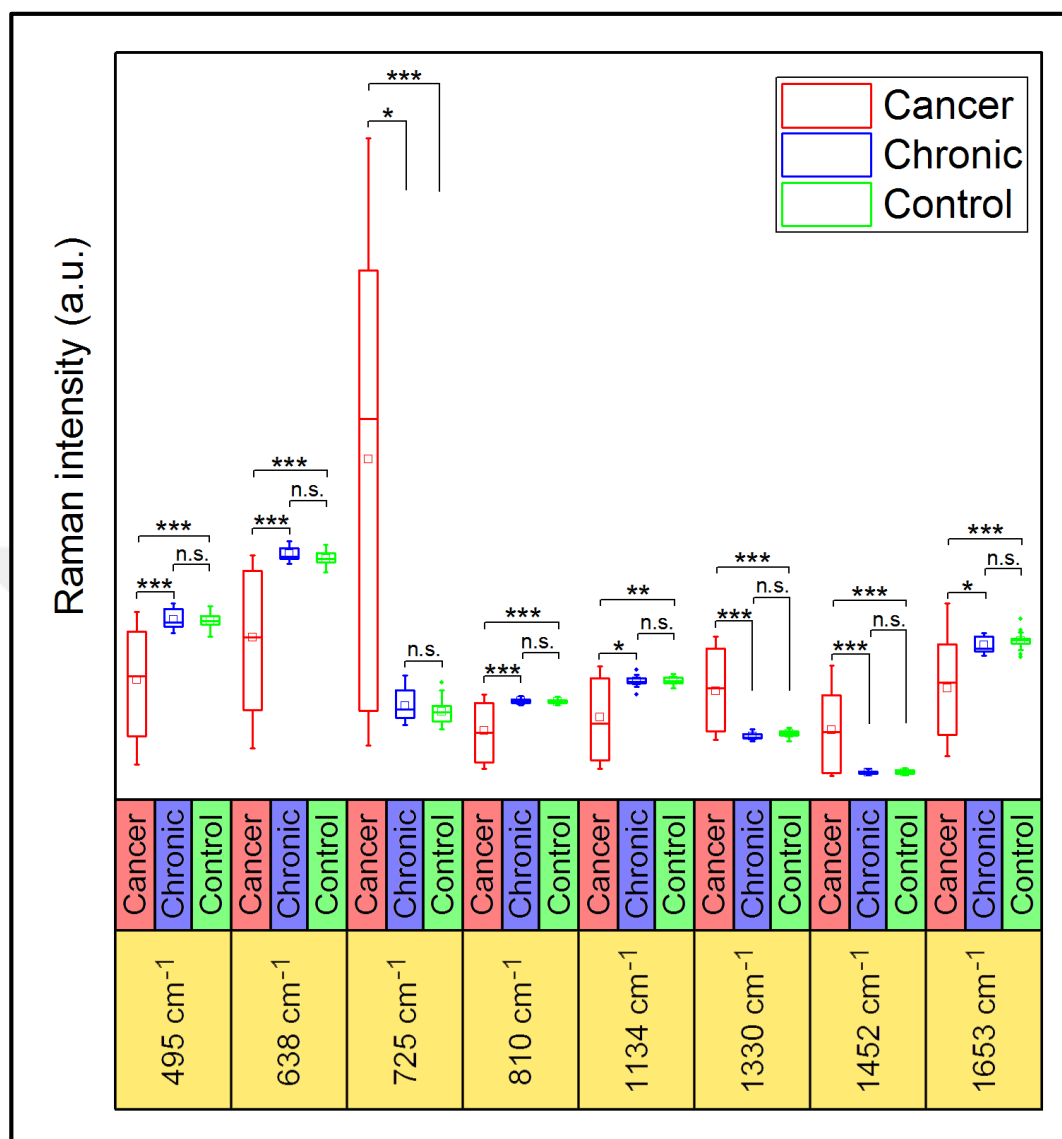


Figure 4.49. Box plots of the intensity values of the eight SERS bands (* $p < 0.05$, ** $p < 0.01$, *** $p < 0.001$, n.s.: not significant). The lines and the squares within each box represent median and mean, respectively. Whiskers represent the 1.5 fold interquartile range.

The horizontal red dashed line is the threshold for classification membership for each spectrum. As seen in the figure, three spectra of the cancer group were below the threshold line meaning that they were classified in the control group after PLS-DA analysis. In the case of control group, two spectra were above the threshold line meaning that they were classified in the cancer group. As a result, 27 out of 30 spectra were correctly classified as cancer. This means 90 percent sensitivity. Twenty eight out of 30 spectra were correctly

classified as cancer achieving 93 percent specificity. Overall diagnostic accuracy was 92 percent. All found classification values were shown in the table below the figure (Table 4.11).

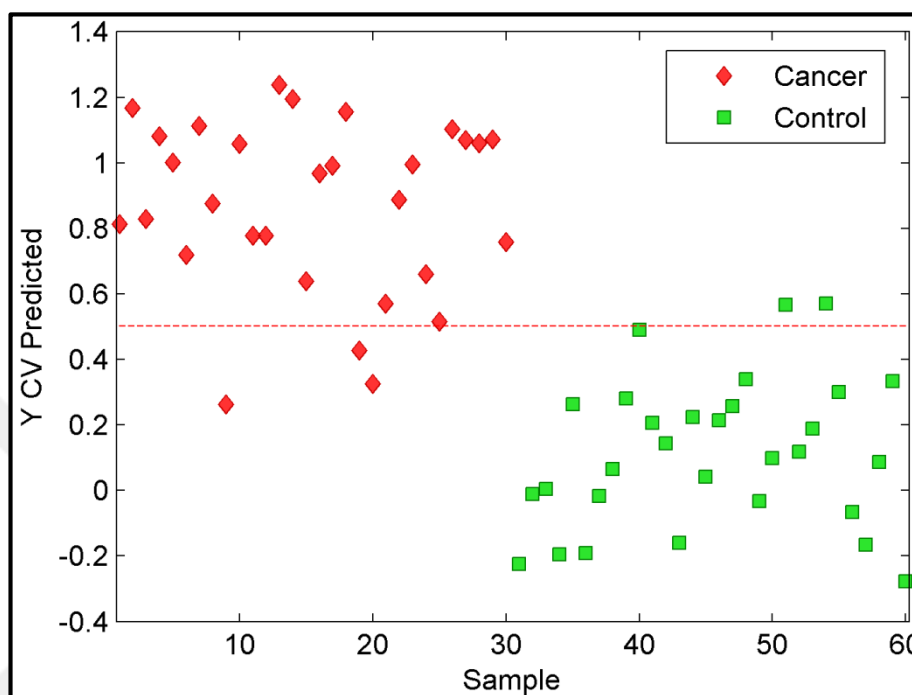


Figure 4.50. PLS-DA scores plot of cancer and control group (32x AgNP).

Table 4.11. Classification results of SERS spectra of the cancer and the control group obtained using 32x AgNP.

	Cancer vs. Control
Sensitivity	90% (27/30)
Specificity	93% (28/30)
Accuracy	92% (55/60)

Receiver operating characteristic curve, i.e. ROC curve, analysis is a method to quantify accuracy of diagnostic tests, in which different true positive rate (sensitivity) vs. false positive rate (1-specificity) values are calculated and plotted using more than one threshold (cut-off) values for separation of two groups. The area under the curve (AUC) defines the validity of diagnostic tests. When AUC is equal to one, diagnostic test is perfect and totally differentiates two groups (i.e., diseased and healthy). As the AUC value decreases,

discriminative ability of the test decreases. AUC=0.5 value shows a complete overlap between two groups, and means failure of the test. In our case, ROC curve for PLS-DA analysis was found as 0.9789 (Figure 4.51) which means nearly perfect separation of cancer and control groups.

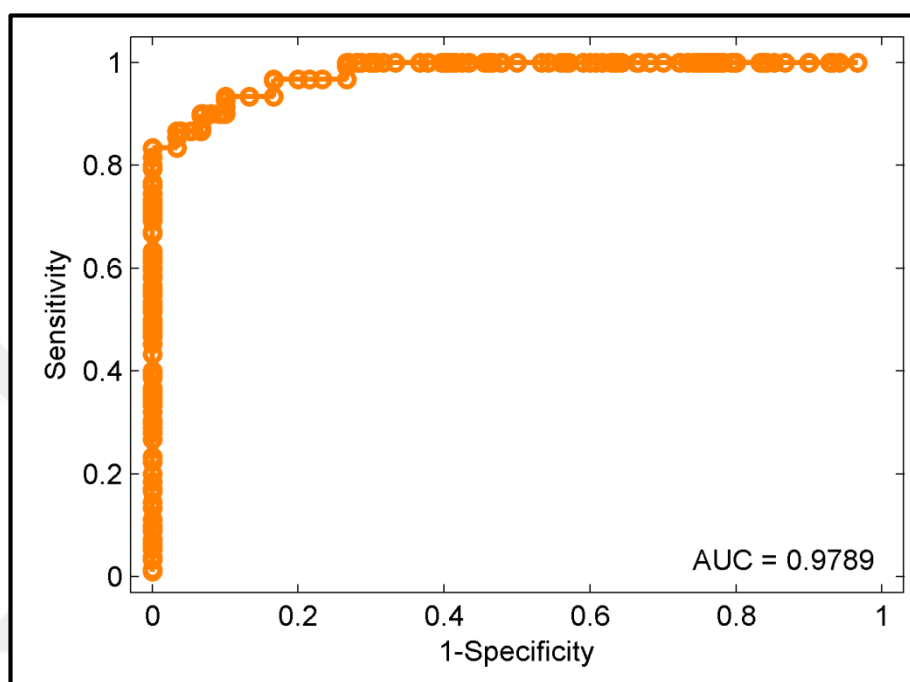


Figure 4.51. ROC curve for cancer and control group (32x AgNP).

As seen Figure 4.50, PLS-DA analysis discriminated well the two group. On the other hand, like many multivariate analysis methods, PLS-DA may also suffer from overfitting. Briefly, in the case of overfitting, PLS-DA model finds a way to separate two classes very well, but it fails to predict the class of external dataset or fails when class labels (i.e., cancer or control) of each X values (i.e., SERS spectra) are shuffled. Since, there is not any external dataset to predict their class using the PLS-model in this thesis. The second approach was performed. It is called permutation test. In this test, class labels of all spectra are shuffled and permuted. New PLS-DA analyses are done for each case, and R^2 values of values of all PLS-DA regressions and Q^2 values (i.e., R^2 after cross validation) of all PLS-DA regressions are used for the permutation test plot. Calculated R^2 and Q^2 values are centered and standardized automatically by the used program (PLS toolbox (Eigenvector Research, Inc.)) so that their Y values in the plot mean their standard deviations. Figure 4.52 shows permutation test results for cancer group vs. control group. One hundred

permutation tests were done to create this plot. In the plot, R^2 and Q^2 values for original class memberships (non-permuted y-block) are demonstrated on the far right side of the plot. X axis is the similarity of the permuted classes to the non-permuted class in terms of correlation coefficient. The further away the R^2 and Q^2 values (in terms of standard deviation) of models created using permuted classes along y-axis, the more unlikely it is the non-permuted (original) model is overfit. In Figure 4.52, it is seen that R^2 and Q^2 values of the original PLS-model are away from the permuted ones. This means that created PLS-model was not overfit and could “indeed” discriminate cancer and control group with 92 percent accuracy.

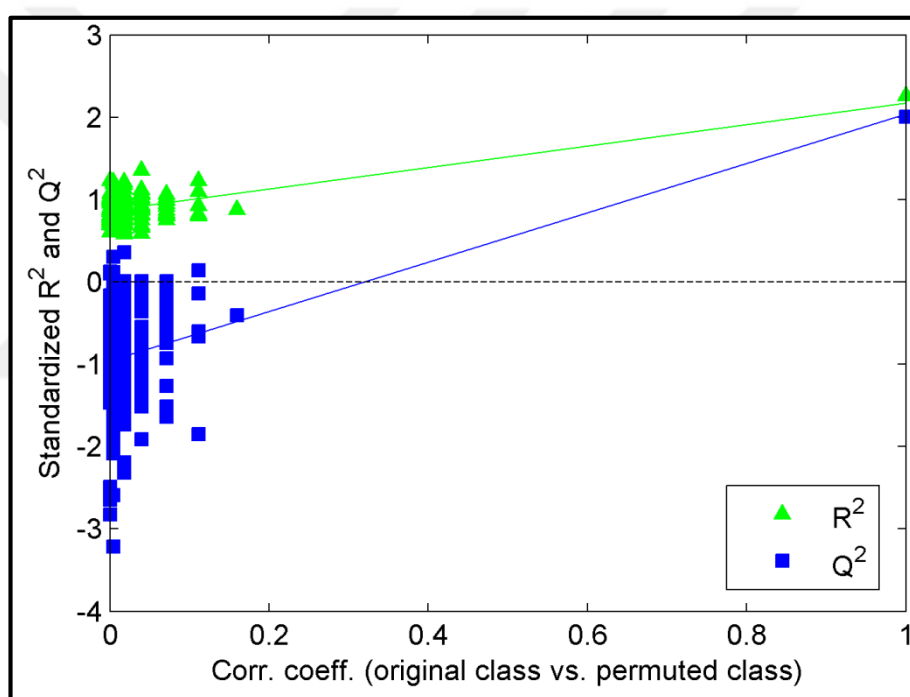


Figure 4.52. Permutation test of cancer vs. control groups (32x AgNP).

In order to obtain better diagnostic accuracy values, genetic algorithms were performed. In this method, subset of the variables which are more helpful for better and more accurate regression model are identified. Using variable subsets, an initial population is set. Each individuals of the population are treated as chromosomes, and offspring of the next generation is produced by applying crossing overs and mutations among individuals. Then, PLS-DA analysis is performed using each progeny and their related RMSECV (root mean square error of cross validation, i.e., Q^2) are calculated. After that, the individuals that result in greater RMSECV values than the median RMSECV value are discarded, and

process continues with producing new offspring for the next generation. After a defined number of generations, selection process stops, and the individual (of the last generation) with lowest RMSECV is selected create PLS-DA model for discrimination of cancer group and control group.

Since instruments' spectral resolution is 0.816 cm^{-1} , a SERS spectrum between 400 cm^{-1} and 1800 cm^{-1} means 1715 variables in this Raman shift range. Before genetic algorithm calculations, adjacent variables are grouped and these group blocks are used for creation of individuals of initial population. The number of adjacent variables in a group is named as "window size". For genetic algorithm calculations of SERS spectra of cancer and control groups, a window size of 25 was used.

The following figure (Figure 4.53) shows the 34 different models produced at the end of genetic algorithm calculations using SERS spectra of cancer and control groups. The model with the lowest RMSECV value (shown with an arrow in the figure) was used discrimination of two groups. The model had 550 variables, meaning 550 different Raman shift values. Since window size was 25, there were 22 blocks of variables each containing 25 Raman shift values.

The chosen 550 variables highlighted in grey shaded areas are shown in Figure 4.54. Using the SERS intensity data of each group at these Raman shift values, new PLS-DA analysis was performed and the results are shown in Figure 4.55. Only one spectra of the cancer group was above the threshold and all spectra of the control group were below the threshold. A sensitivity of 97 percent, a selectivity of 100 percent, and an overall accuracy of 98 percent was achieved (Table 4.12). As compared to the previous results, application of genetic algorithms for PLS-DA analysis gave better diagnostic values. Furthermore, better performance was also observed in ROC curve analysis (Figure 4.56). AUC was 0.9989 which was higher than the previous result.

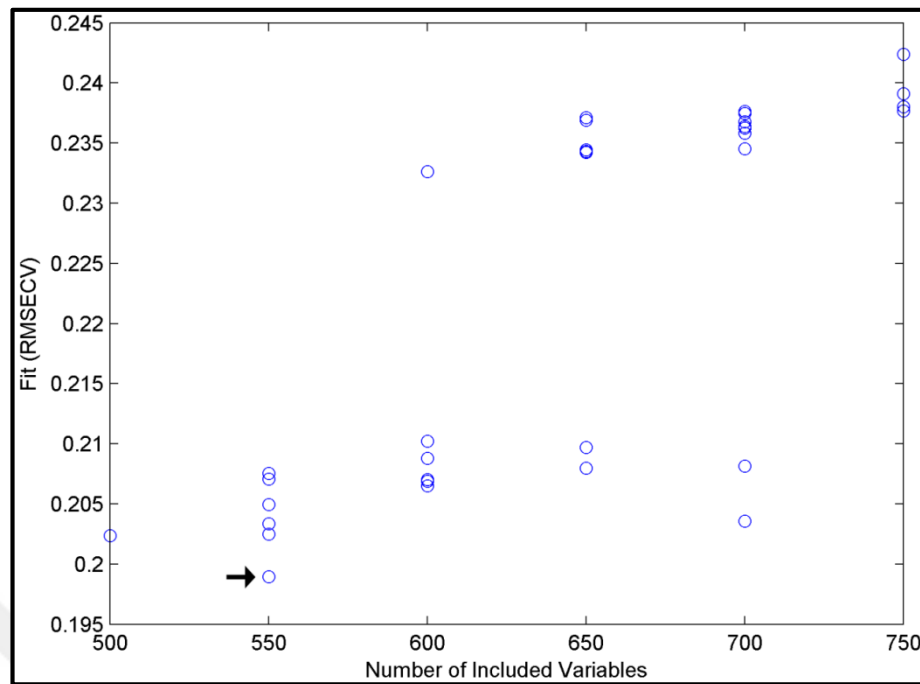


Figure 4.53. Frequency of window usage in models generated using genetic algorithms.
Arrow indicates the RMSECV value.

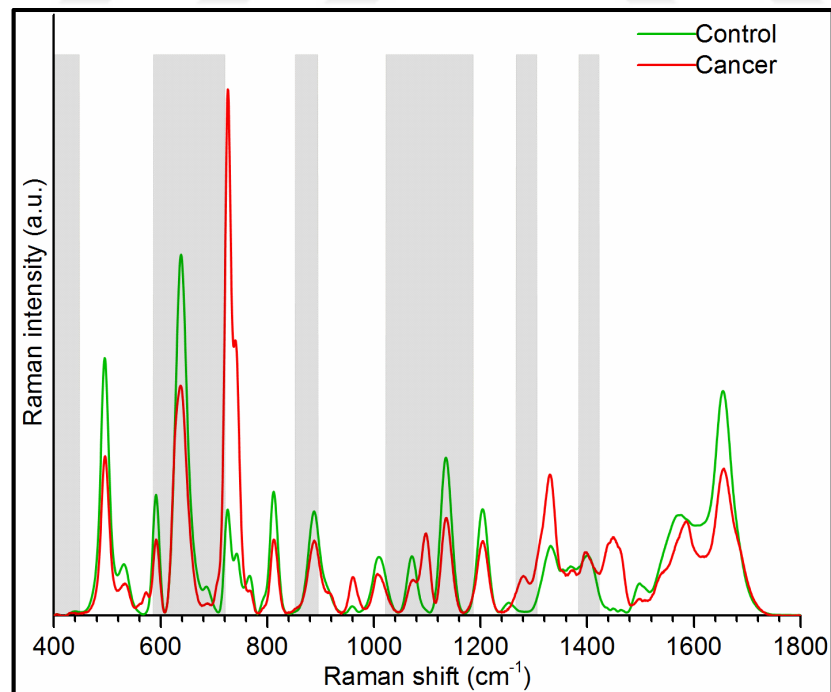


Figure 4.54. Shaded regions are the chosen shift regions with genetic algorithms (GA) for cancer vs. control study with 32x AgNP.

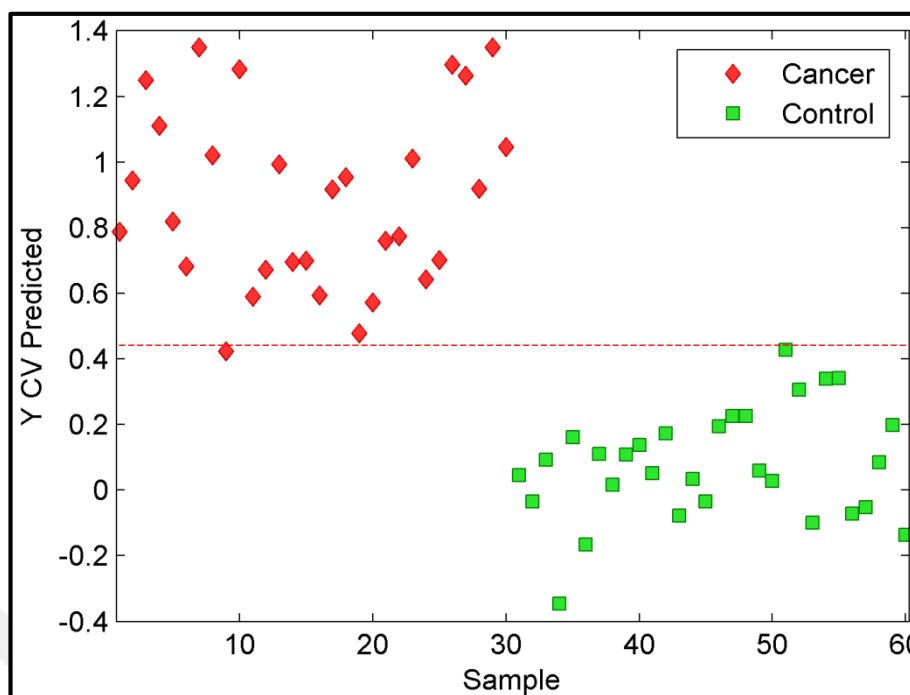


Figure 4.55. PLS-DA scores plot of cancer and control group (32x AgNP, with genetic algorithms (GA)).

Table 4.12. Classification results of SERS spectra of the cancer and the control group obtained using 32x AgNP (with GA)

	Cancer vs. Control
Sensitivity	97% (29/30)
Specificity	100% (30/30)
Accuracy	98% (59/60)

Permutation test was also applied to investigate any overfitting in the PLS-DA model (Figure 4.57). R^2 and Q^2 values of the original PLS-model were away from the permuted ones. Therefore, it could be stated that created PLS-DA model could discriminate SERS spectra of cancer patients and healthy subjects.

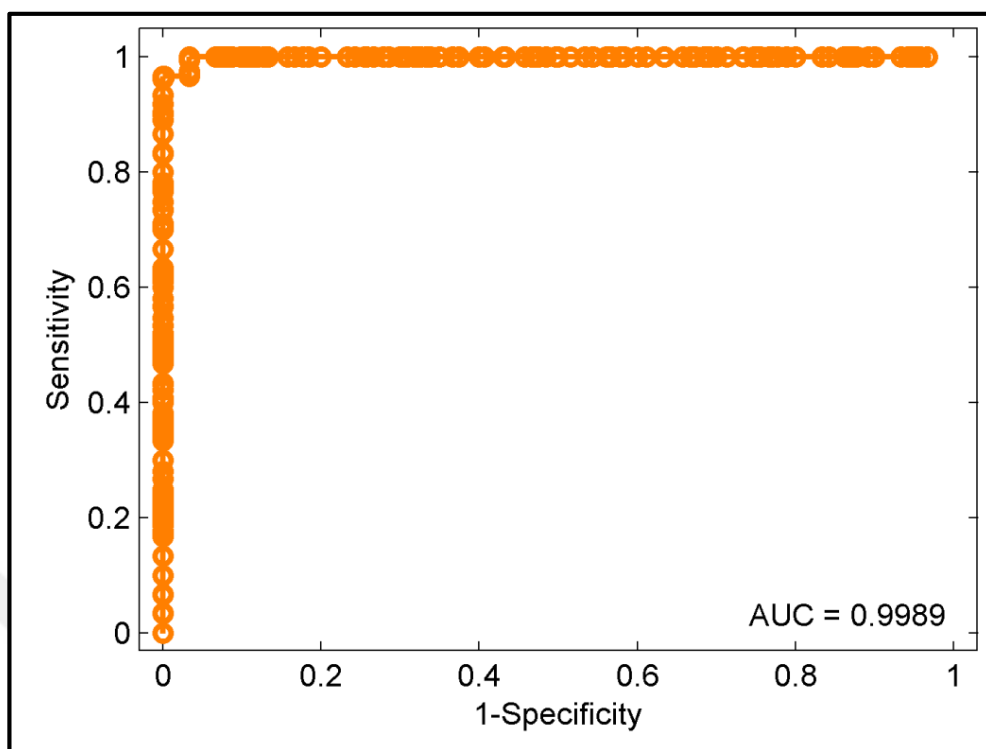


Figure 4.56. ROC curve for cancer and control group (32x AgNP, with GA).

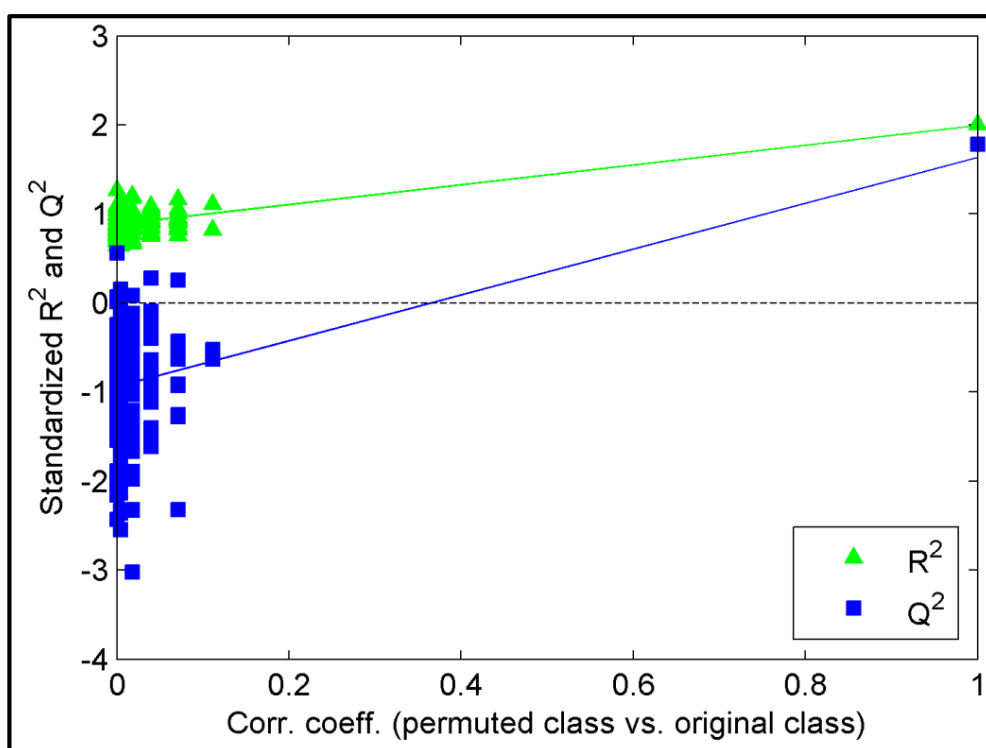


Figure 4.57. Permutation test of cancer vs. control groups (32x AgNP, with GA).

The use of 32x AgNP colloid for discrimination of the cancer group and the control group gave good results. The next group couples to differentiate were the chronic disease group and the cancer group. As seen in Figure 4.48, spectral patterns of the average spectrum of chronic disease group were quite similar to that of control group. Therefore, it would be expected that discrimination of the two groups would give the similar results with the discrimination of the cancer and the control group. Figure 4.58 shows the PLS-DA results of the differentiation attempt. One spectrum of the chronic diseases group was below the discrimination threshold, and four spectra of the cancer group was the above the threshold. As seen in the Table 4.13, diagnostic ability of the PLS-DA analysis was resulted in a sensitivity of 93 percent, a specificity of 87 percent with an overall accuracy of 89 percent. These values were slightly lower than the values for discrimination of the cancer and the control group, giving the hope that the control group and the chronic disease group could also be discriminated using PLS-DA analysis although there was spectral resemblance between the two groups.

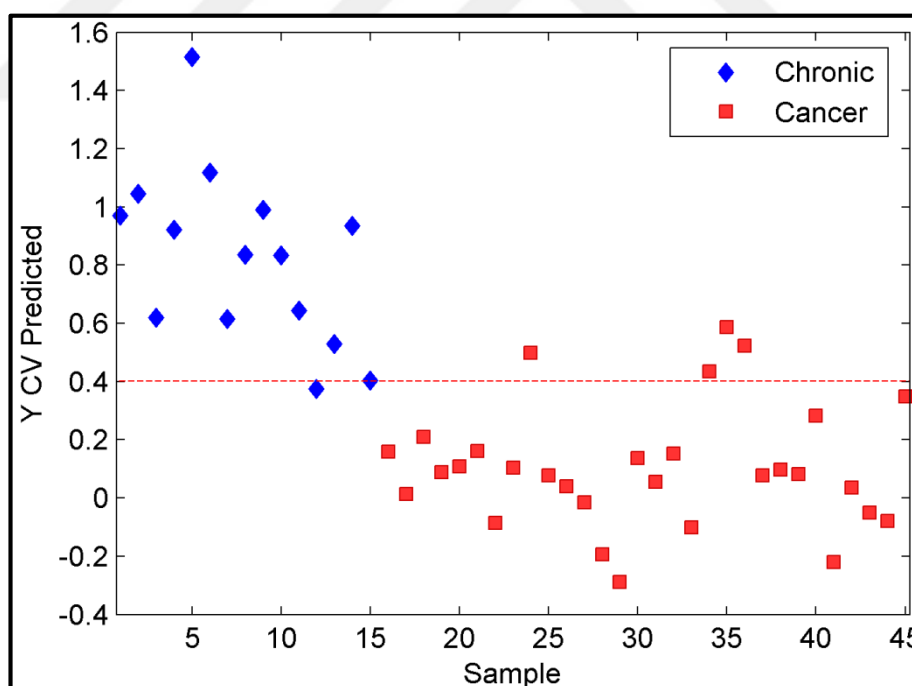


Figure 4.58. PLS-DA scores plot of chronic and cancer groups (32x AgNP).

Table 4.13. Classification results of SERS spectra of the chronic and the cancer group obtained using 32x AgNP.

	Chronic vs. Cancer
Sensitivity	93% (14/15)
Specificity	87% (26/30)
Accuracy	89% (40/45)

Next step was the ROC curve analysis (Figure 4.59). AUC value was found as 0.98 which meant near perfect difference between two groups. Permutation test was also performed doing 100 different permutations on class labels (Figure 4.60). Original class was well-above from the others along y-axis, meaning that there was not overfitting during PLS-DA analysis. Therefore, found sensitivity, specificity, and accuracy values were valid.

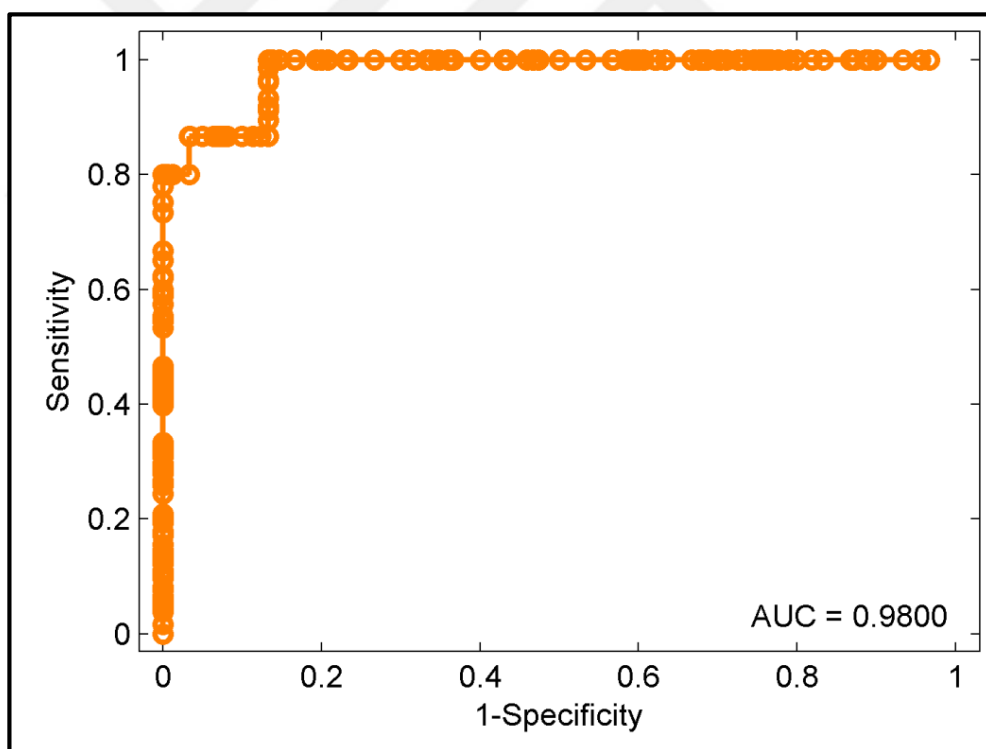


Figure 4.59. ROC curve for chronic and cancer group (32x AgNP).

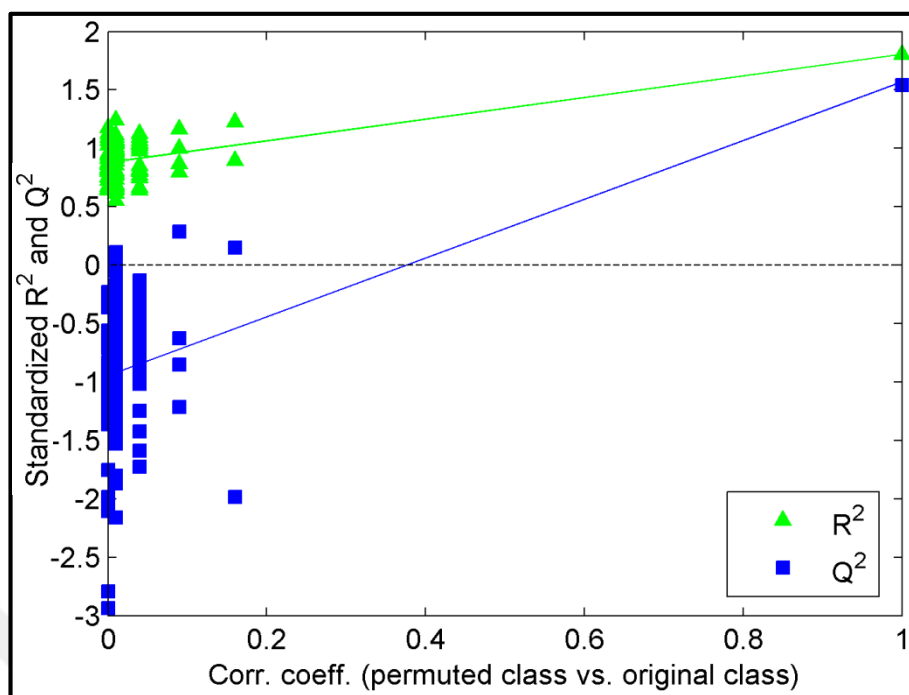


Figure 4.60. Permutation test of chronic vs. cancer groups (32x AgNP).

GA analysis was performed to search a better diagnostic differentiation between the two groups. Four hundred Raman bands were found by GA analysis. Chosen bands are shown as gray background in Figure 4.61. PLS-DA analysis after GA gave better results than without GA (Figure 4.62). One spectrum out of 15 spectra of the chronic disease group was below the discrimination threshold and one out of 30 spectra of the cancer group was above the threshold. The diagnostic sensitivity and specificity for discrimination of the cancer group from the chronic disease group were 93 percent and 97 percent, respectively (Table 4.14). Accuracy was 96 percent, which was seven percent higher than without the use of GA.

The area under ROC curve was 0.9956, showing that SERS spectra of serum can be used for differentiation of cancer and chronic diseases with high diagnostic accuracy (Figure 4.63). R^2 and Q^2 values of the original class were significantly different than the permuted ones as shown in Figure 4.64. Both AUC value and permutation test demonstrated that SERS spectra of the chronic disease group well discriminated from the SERS spectra of the cancer group.

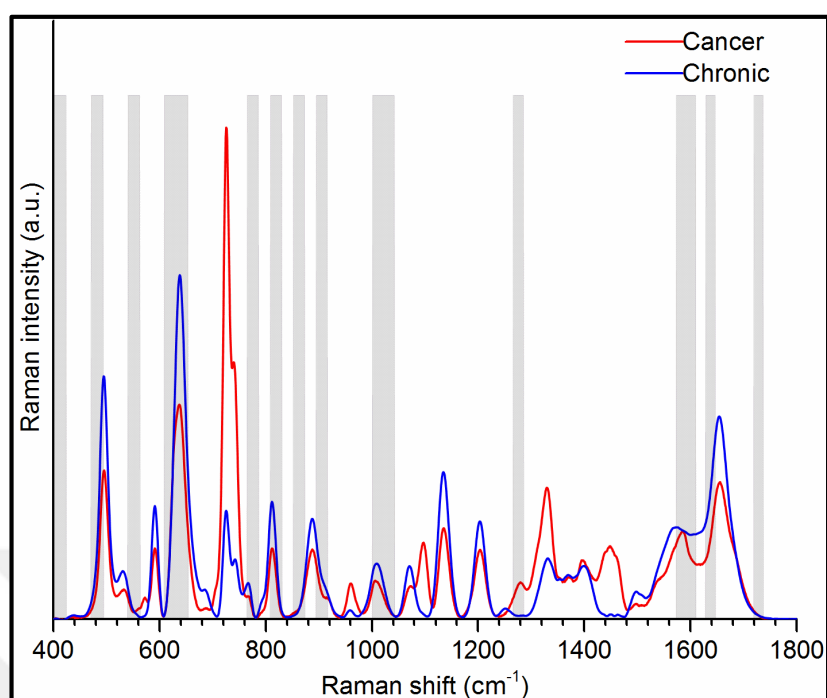


Figure 4.61. Shaded regions are the chosen shift regions with genetic algorithms (GA) for chronic vs. cancer study with 32x AgNP.

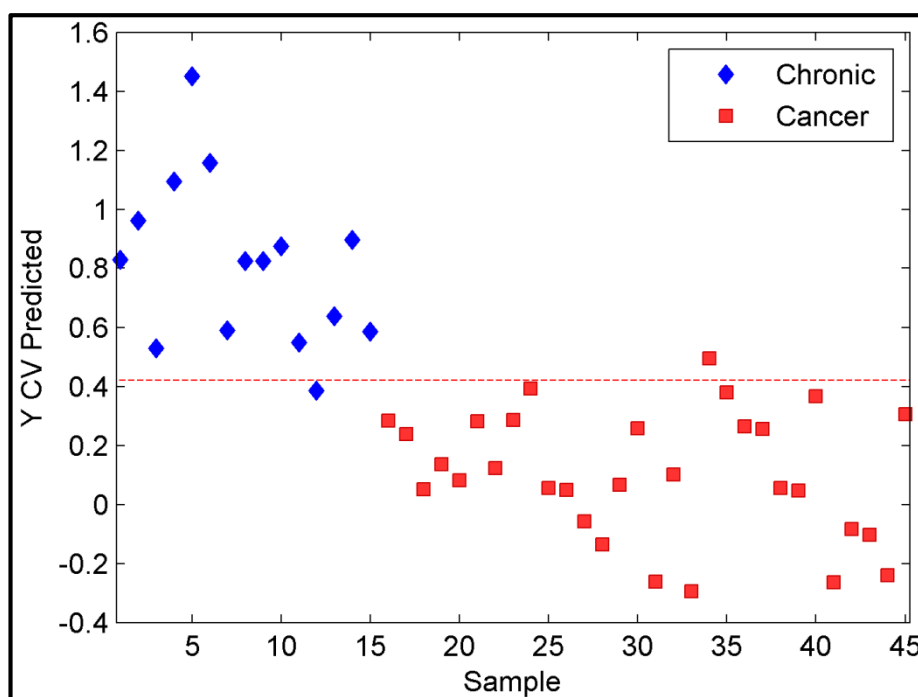


Figure 4.62. PLS-DA scores plot of chronic and cancer groups (32x AgNP, with GA).

Table 4.14. Classification results of SERS spectra of the chronic and the cancer group obtained using 32x AgNP (GA).

	Chronic vs. Cancer
Sensitivity	93% (14/15)
Specificity	97% (29/30)
Accuracy	96% (43/45)

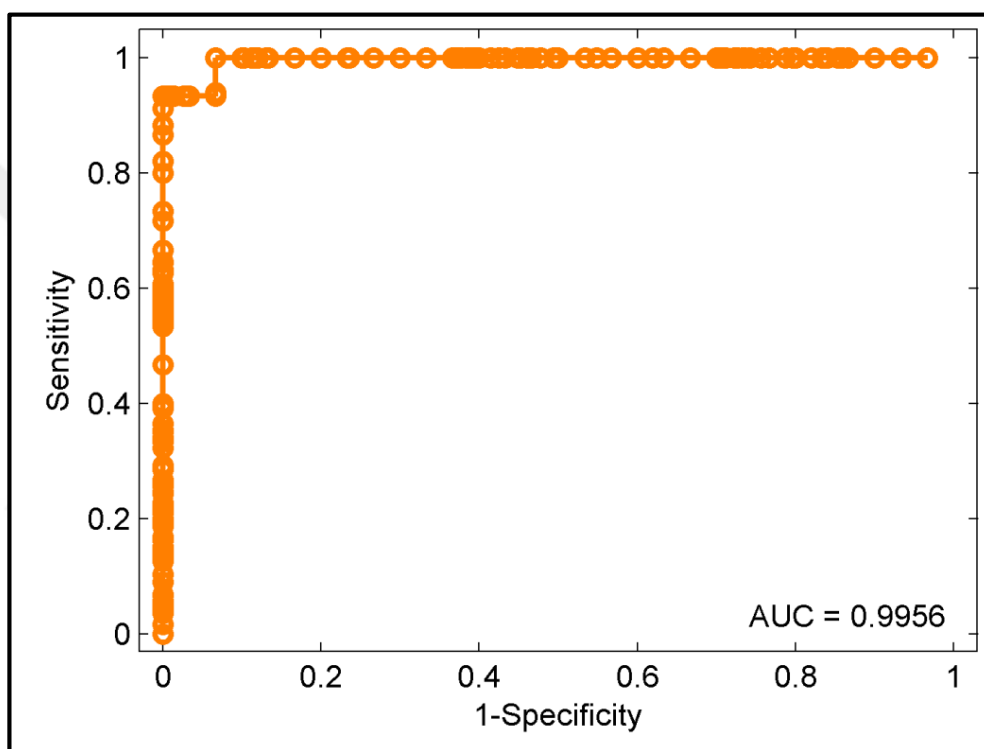


Figure 4.63. ROC curve for chronic and cancer group (32x AgNP, with GA).

Next couple to differentiate was the chronic disease group and the control group. Due close similarity of the spectra of the two groups, performance of PLS-DA was not as good as the previous analyses (Figure 4.65). Eight spectra of the chronic disease group were below the threshold, and nine spectra of the control group were above the threshold. The obtained sensitivity of the diagnostic analysis was 47 percent, specificity was 70 percent, and accuracy was 62 percent (Table 4.15). Area under the ROC curve found as 0.6745 (Figure 4.66). Since an AUC of 0.5 means that discrimination relies on pure chance (as the case of a coin flipping), diagnostic ability of the PLS-DA model was not good. This situation was

also demonstrated by performing a permutation test (Figure 4.67). R^2 and Q^2 values of the non-permuted class were not separated from the permuted ones.

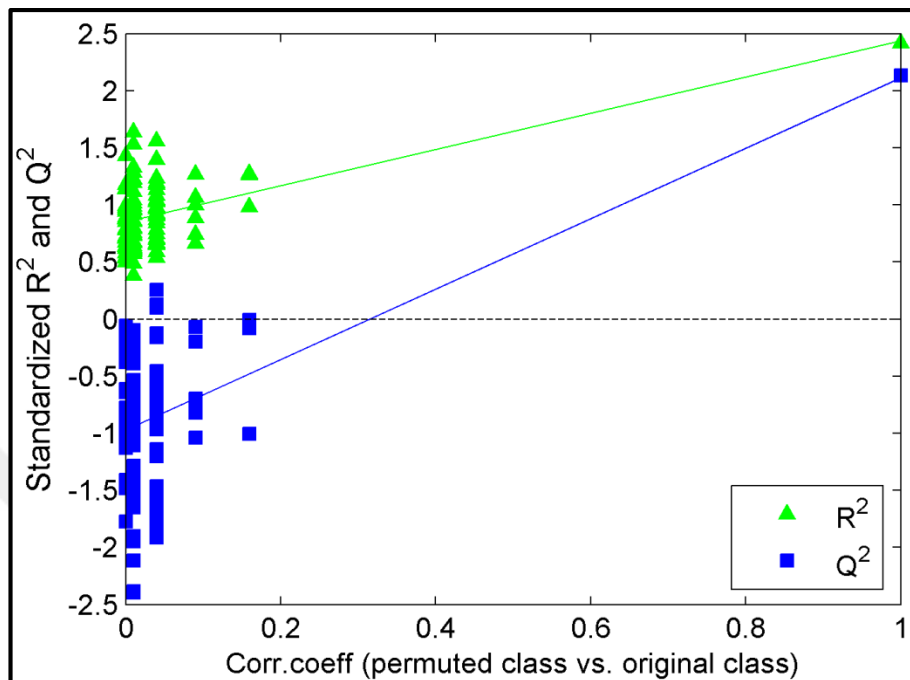


Figure 4.64. Permutation test of chronic vs. cancer groups (32x AgNP, with GA).

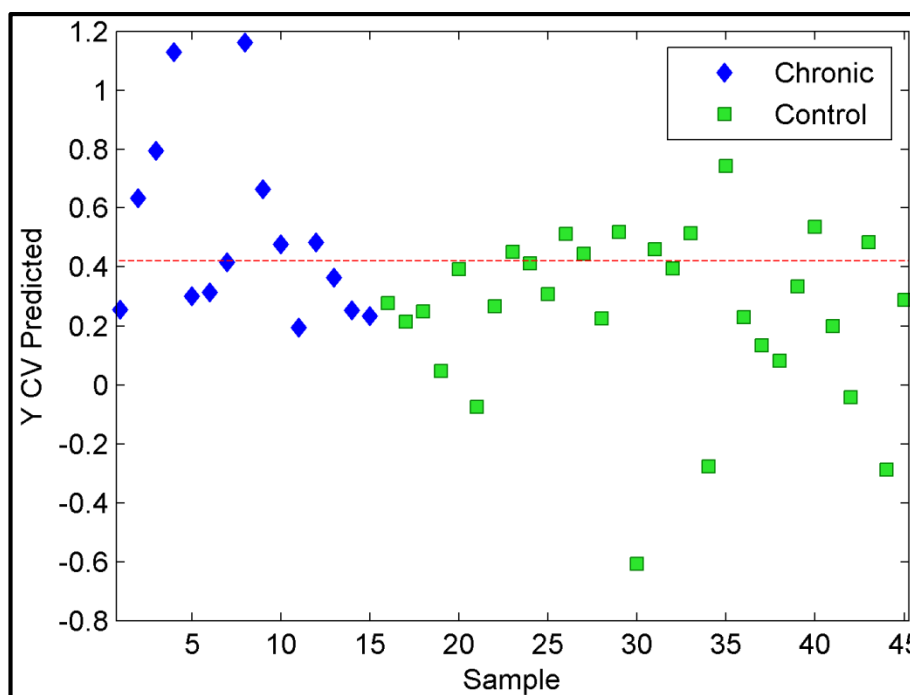


Figure 4.65. PLS-DA scores plot of chronic and control groups (32x AgNP).

Table 4.15. Classification results of SERS spectra of the chronic and the control group obtained using 32x AgNP.

	Chronic vs. Control
Sensitivity	47% (7/15)
Specificity	70% (21/30)
Accuracy	62% (28/45)

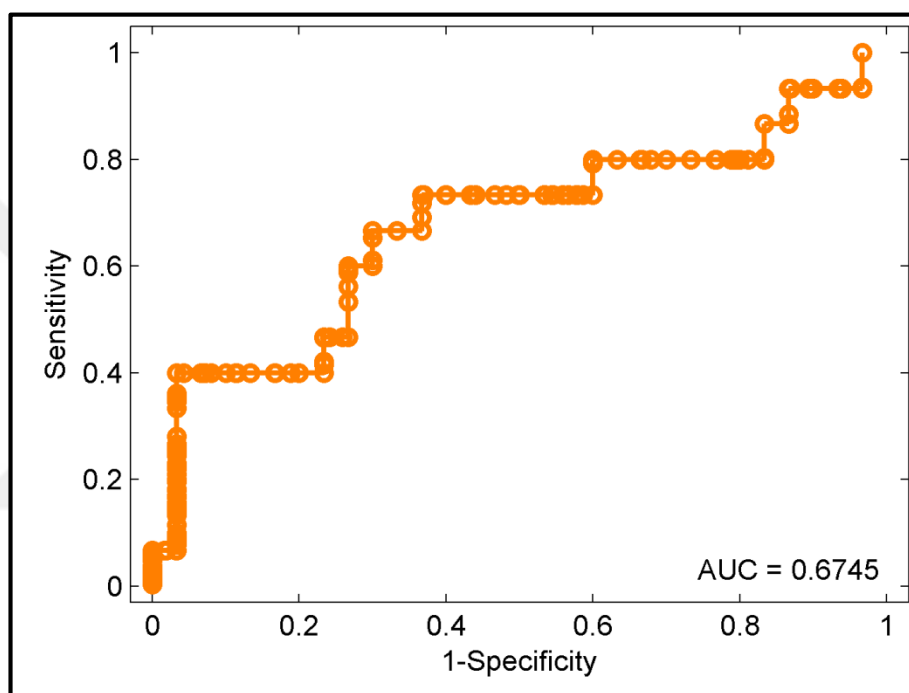


Figure 4.66. ROC curve for chronic and control group (32x AgNP).

The use of 240 Raman shift variables defined by GA (Figure 4.68) for PLS-DA resulted in a better discrimination by PLS-DA. Eleven spectra of the chronic disease group and 25 spectra of the control group were correctly classified (Figure 4.69). The acquired sensitivity was 73 percent, the specificity was 83 percent, and the accuracy was 80 percent (Table 4.16). The AUC value was also increased by 12 percent reaching the value of 0.7978 (Figure 4.70). R^2 and Q^2 values of the non-permuted class were slightly above the R^2 and Q^2 values of the permuted ones (Figure 4.71).

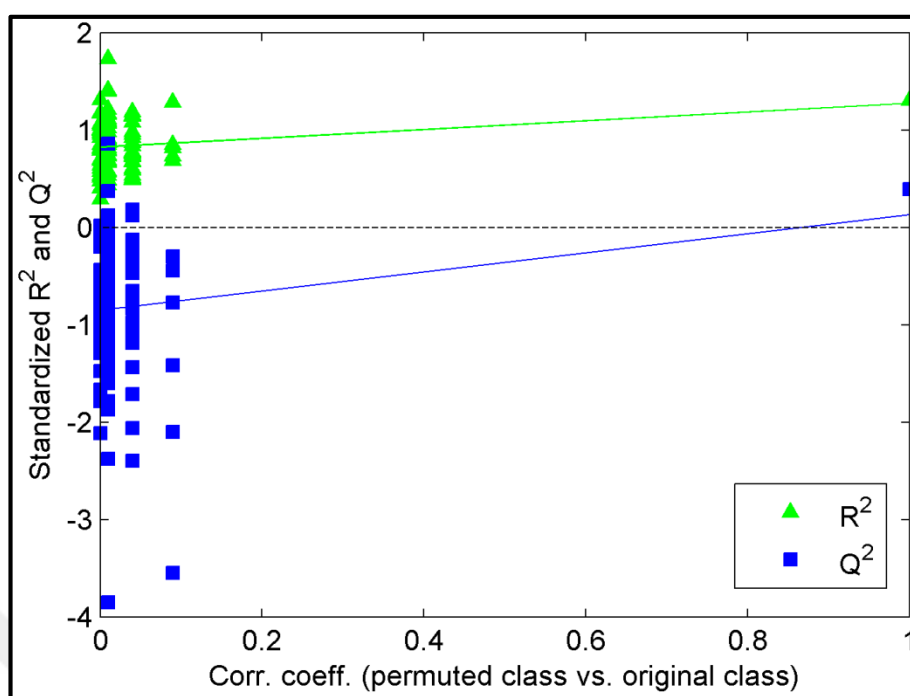


Figure 4.67. Permutation test of chronic vs. control groups (32x AgNP).

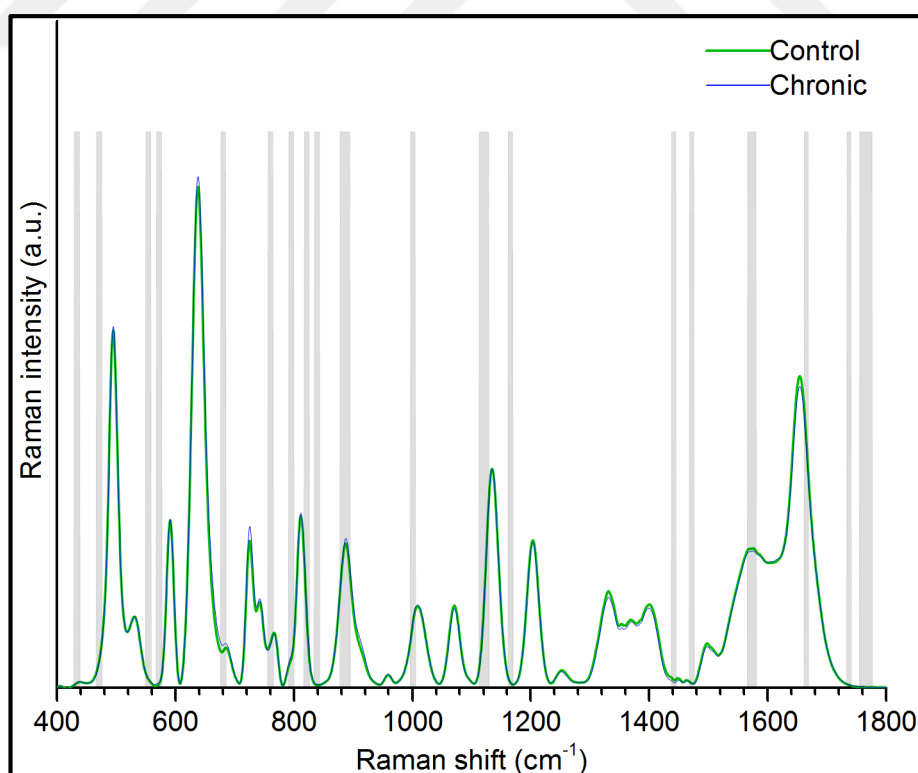


Figure 4.68. Shaded regions are the chosen shift regions with genetic algorithms (GA) for chronic vs. control study with 32x AgNP.

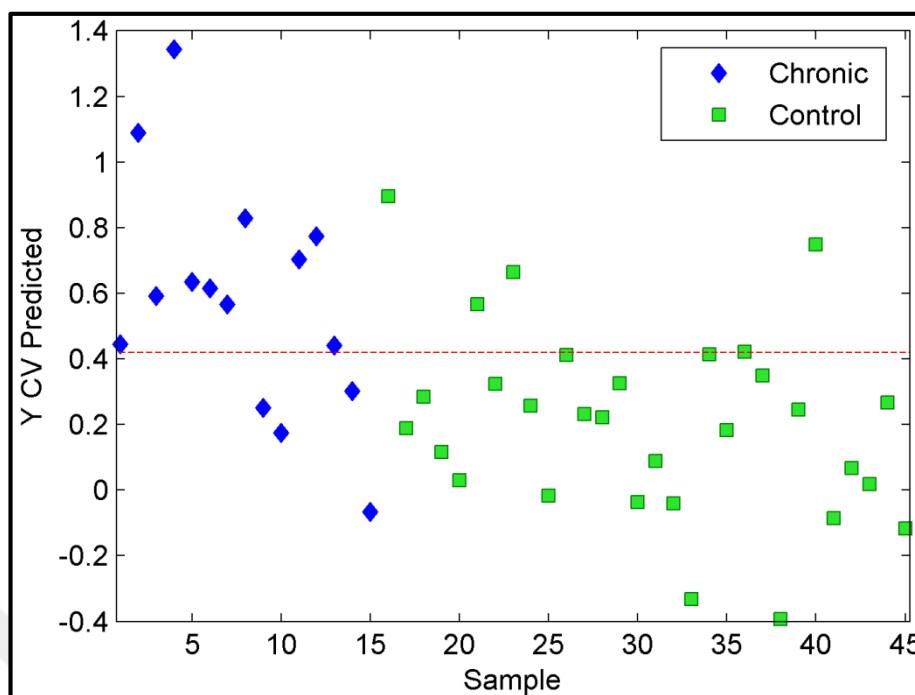


Figure 4.69. PLS-DA scores plot of chronic and control groups (32x AgNP, with GA).

Table 4.16. Classification results of SERS spectra of the chronic and the control group obtained using 32x AgNP (GA).

Chronic vs. Control	
Sensitivity	73% (11/15)
Specificity	83% (25/30)
Accuracy	80% (36/45)

The use of 32x AgNP colloidal suspension was gave very good accuracies for discrimination of cancer group from control group and chronic diseases group. On the other hand, the chronic disease group could not be differentiated from the control group. Even after GA application, accuracy of the PLS-DA model was 80 percent. One reason for this might have been the concentration of AgNP colloid. With the use of 32x AgNP colloid, molecules with lesser affinity to silver surface but higher Raman scattering ability may dominate the spectrum. By decreasing the the AgNP concentration, the other molecules which possess higher affinity to silver surface but less Raman scattering ability may have more chance to contribute the spectral shape of serum. Therefore, the same studies discussed so far were also performed using 8x AgNP colloid. The acquired average

SERS spectra of serum samples of 30 cancer patients, 15 patients with chronic disease, and 30 healthy people (as control group) are shown in the Figure 4.72.

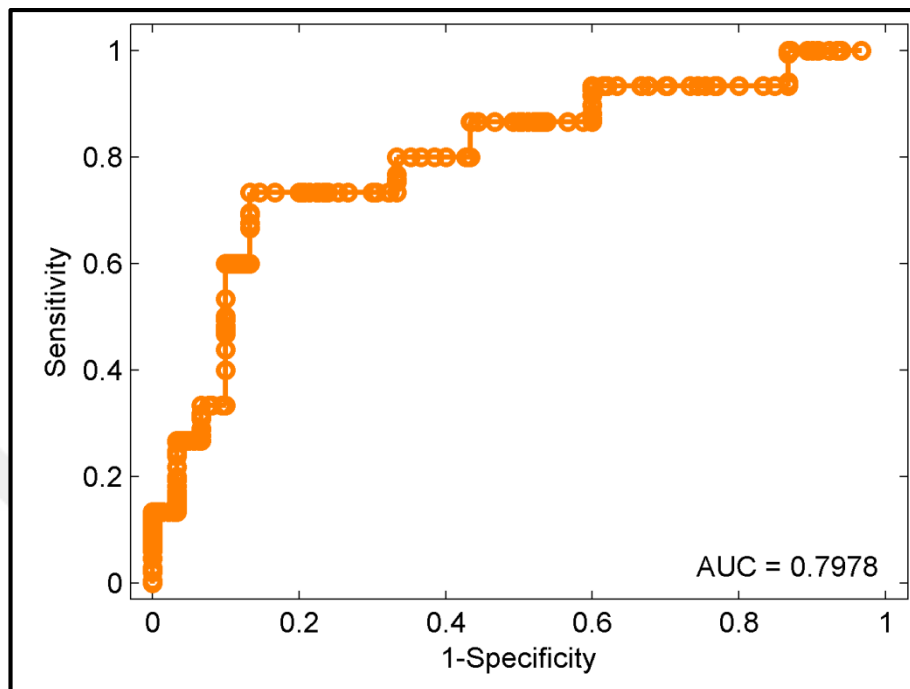


Figure 4.70. ROC curve for chronic and control group (32x AgNP, with GA).

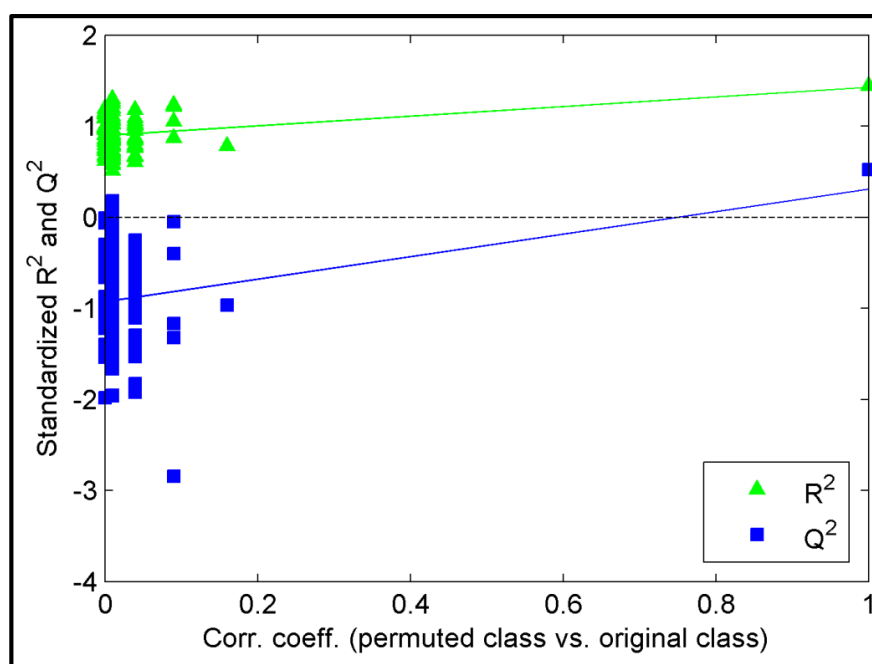


Figure 4.71. Permutation test of chronic vs. control groups (32x AgNP, with GA).

As happened with the use of 32x AgNP, average spectra of the three groups had similar features with commercial WS spectra presented in Figure 1. Spectra of the control group and chronic disease group were similar to the WS spectrum obtained using 8x AgNP, whereas spectrum of the cancer group was similar to the WS spectrum obtained using 4x AgNP. The bands at 725 cm^{-1} , 1330 cm^{-1} , and 1452 cm^{-1} in the difference spectra of cancer and control groups could be attributed to hypoxanthine. On the other hand, the decrease in the intensities of the bands at 495 cm^{-1} , 638 cm^{-1} , and 830 cm^{-1} showed the decrease in uric acid concentration relative to the other metabolites in the case of cancer disease. Standard deviations of the control group spectra and chronic disease group spectra were very low. On the other hand, standard deviation of the cancer group spectrum was high. This meant that for healthy people and for the chronic diseases studied in this thesis, relative concentrations of the metabolites having impact on serum SERS spectrum were about the same, but for cancer patients, they were quite variable. Comparison of the difference spectra of cancer group and control group obtained using 32x AgNP and 8x AgNP are provided in Figure 4.73. If uric acid and hypoxanthine had been the only determinants of serum spectrum, two difference spectra would have been the same. On the other hand, although intensities of 725 cm^{-1} and 638 cm^{-1} bands were the same for both difference spectra, there were differences at many Raman shift positions. This proved that hypoxanthine and uric acid were not the sole determinant of the spectral differences between the cancer group and the control group. The use of different AgNP colloid concentrations and comparing the acquired spectra revealed the effects of some other molecules present in serum. Bands in the difference spectrum of chronic disease group and control group in Figure 4.72 were more prominent than the difference spectra obtained with 32x AgNP. Comparison of the difference spectra of chronic disease group and control group obtained using 32x AgNP and 8x AgNP are provided in Figure 4.73. Two spectra were totally different and hence revealing the effects of other molecules. The weight of 638 cm^{-1} band of uric acid and 725 cm^{-1} band of hypoxanthine on the difference spectrum was more when 8x AgNP was used.

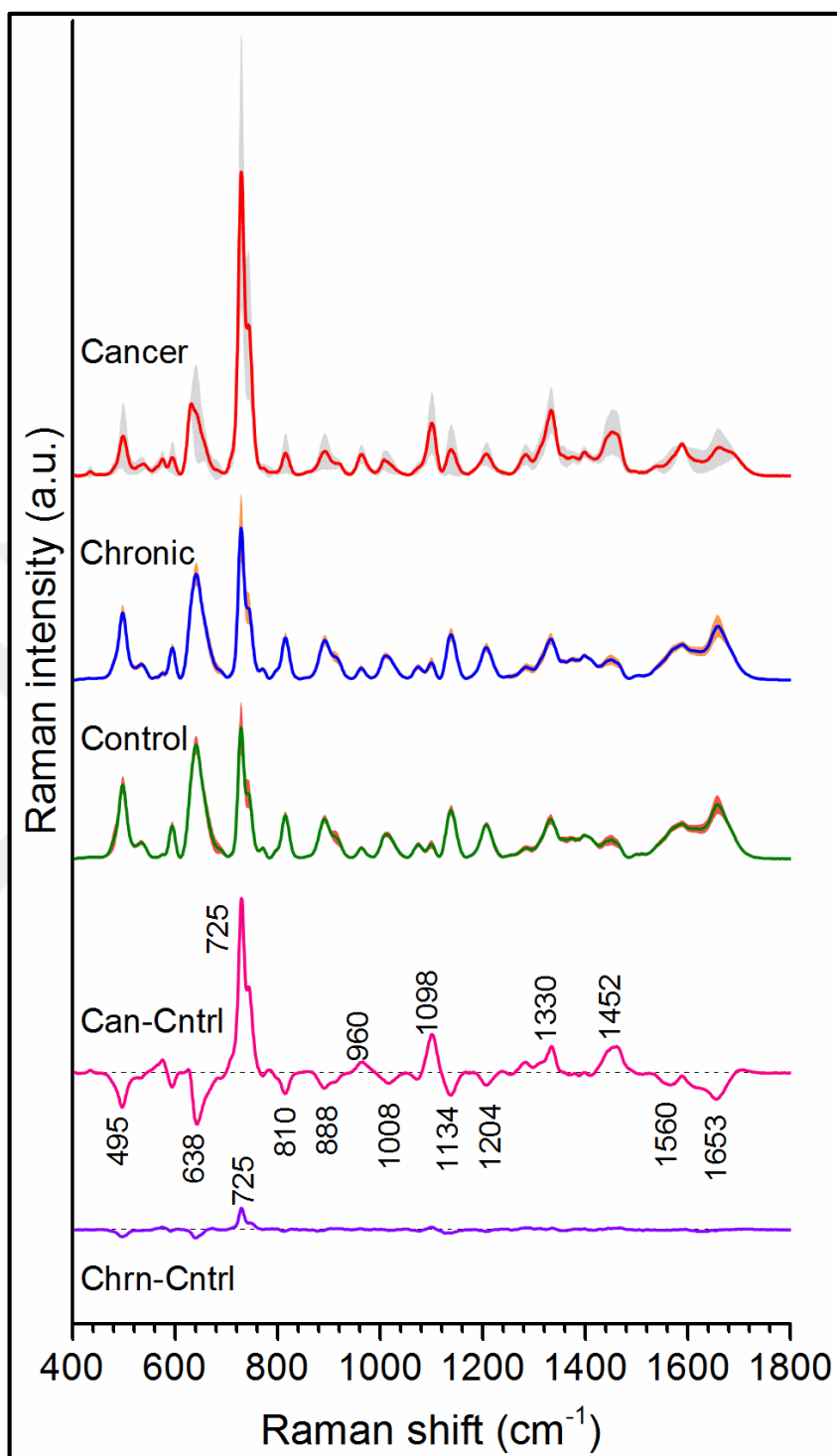


Figure 4.72. Average SERS spectra of serum samples of cancer and chronic disease afflicted patients and healthy subjects obtained using 8x AgNP. Shaded areas around the spectra represent the standard deviations. Bottom two spectra are the difference spectra (Can-Cntrl: Cancer-Control, Chrn-Control: Chronic-Control).

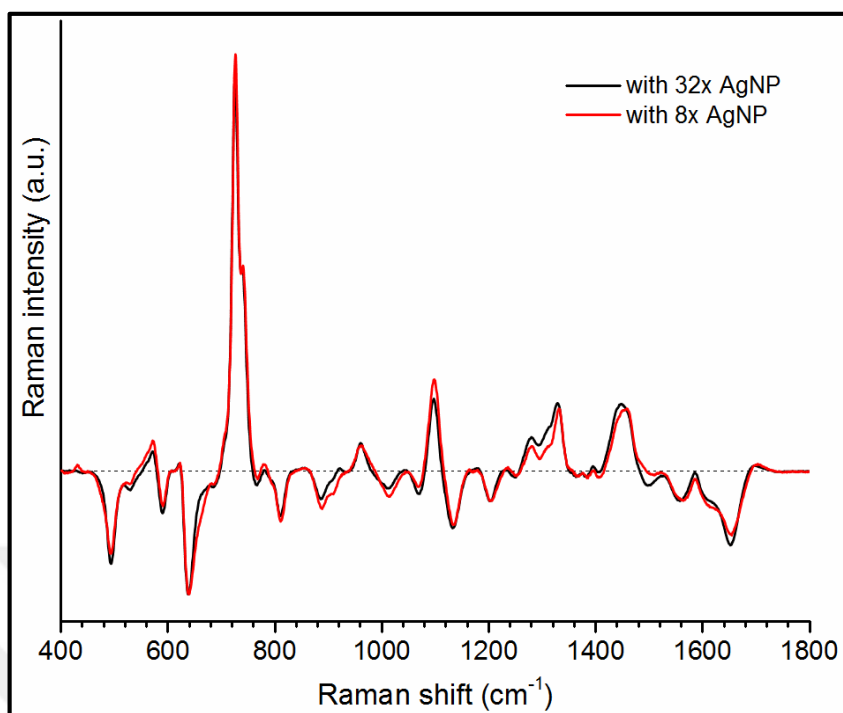


Figure 4.73. The difference spectra of cancer group and control group obtained using 32x AgNP and 8x AgNP.

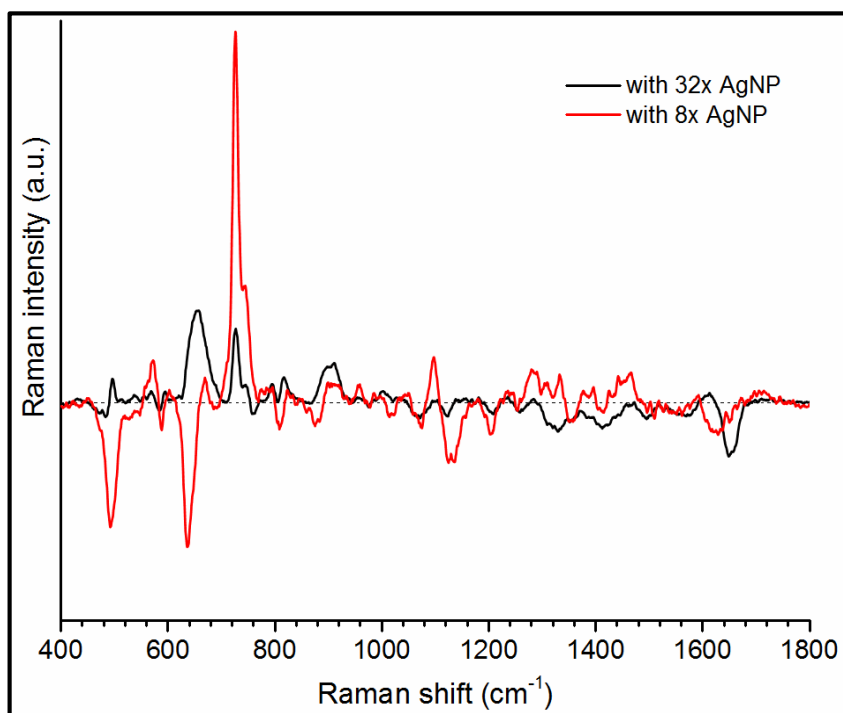


Figure 4.74. The difference spectra of chronic disease group and control group obtained using 32x AgNP and 8x AgNP.

Regarding PLS-DA scores, five of 30 spectra of the cancer group were below the threshold and 3 of the control group were above the threshold (Figure 4.75). Based on these results, prediction sensitivity was 83 percent, specificity was 90 percent, and accuracy was 87 percent (Table 4.17). Performance of PLS-DA model was also evaluated using ROC curve analysis and permutation test. An AUC value of 0.9278 was obtained (Figure 4.76). R^2 and Q^2 values of the permuted classes were a few standard deviations away from the original ones (Figure 4.77). One thing to note that compared to Figure 4.52, distance between the original values and the permuted values were more, which means that the model obtained using 8x was better than using 32x regarding the over-fitting issue was concerned.

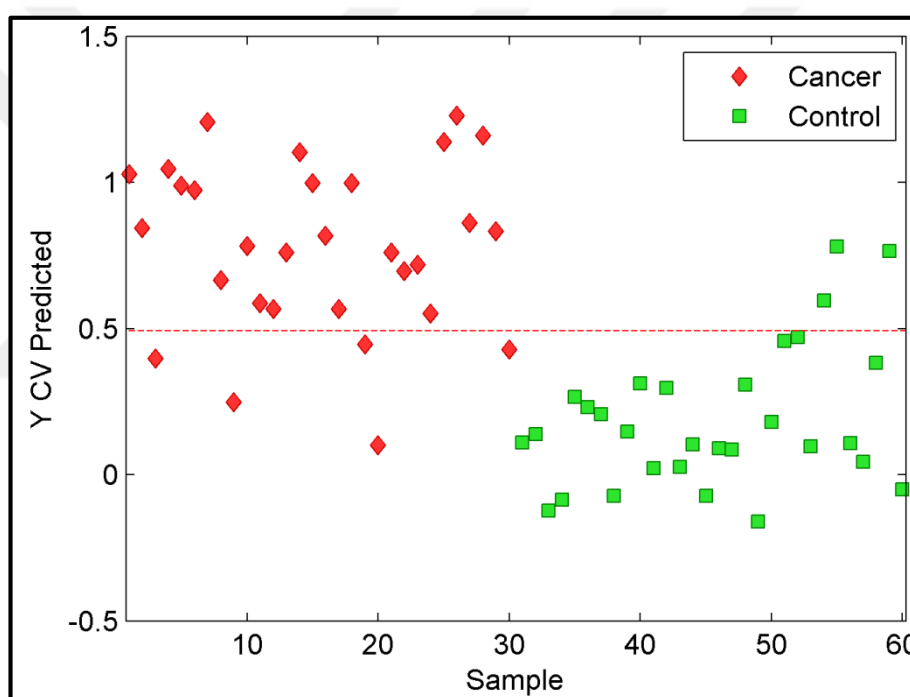


Figure 4.75. PLS-DA scores plot of cancer and control group (8x AgNP).

Table 4.17. Classification results of SERS spectra of the cancer and the control group obtained using 8x AgNP.

	Cancer vs. Control
Sensitivity	83% (25/30)
Specificity	90% (27/30)
Accuracy	87% (52/60)

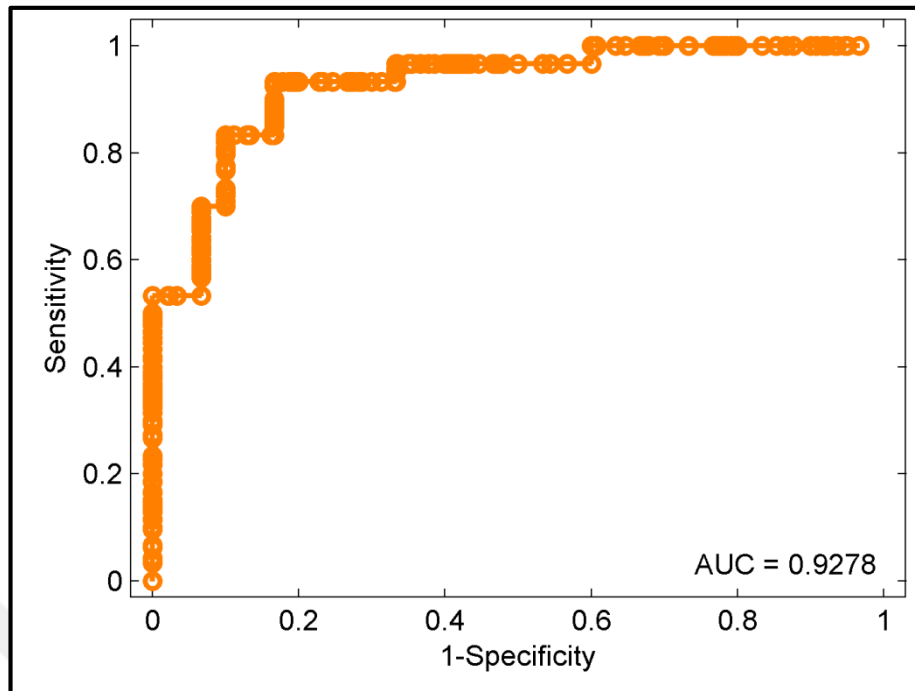


Figure 4.76. ROC curve for cancer and control group (8x AgNP).

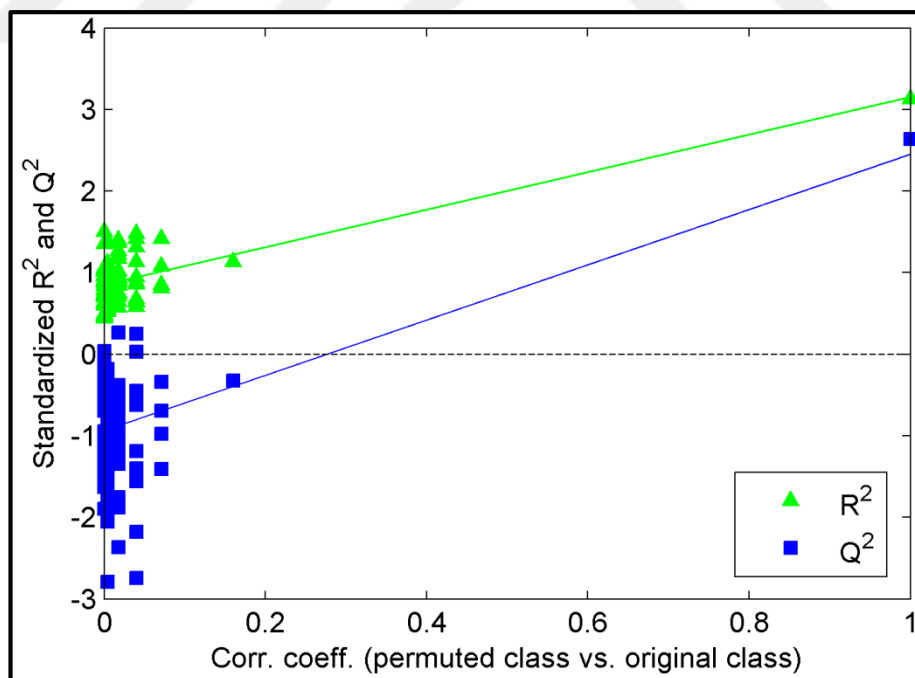


Figure 4.77. Permutation test of cancer vs. control groups (8x AgNP).

GA was also performed to increase diagnostic performance of PLS-DA. Selected 275 Raman shift values were shown in Figure 4.78 below.

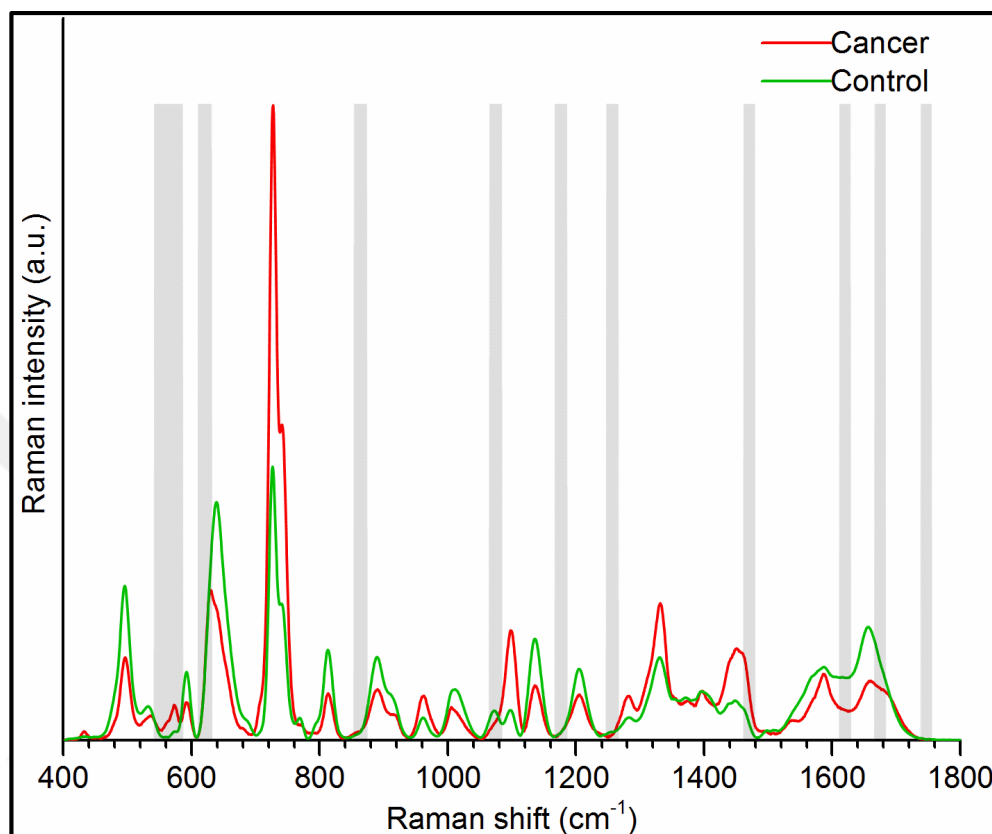


Figure 4.78. Shaded regions are the chosen shift regions with genetic algorithms (GA) for cancer vs. control study with 8x AgNP.

Based on the selected Raman bands, PLS-DA was performed. One out of 30 spectra of cancer group was below the threshold line whereas all 30 spectra of the control group were classified correctly (Figure 4.79). This gave a diagnostic sensitivity of 97 percent, a specificity of 100 percent, and an accuracy of 98 percent (Table 4.18). The AUC value was 0.9989 (Figure 4.80), which was near perfection. R^2 and Q^2 values of the permuted classes were a few standard deviations away from the original ones (Figure 4.81). Although accuracy values were the same with obtained using 32x AgNP, permutation test results were better.

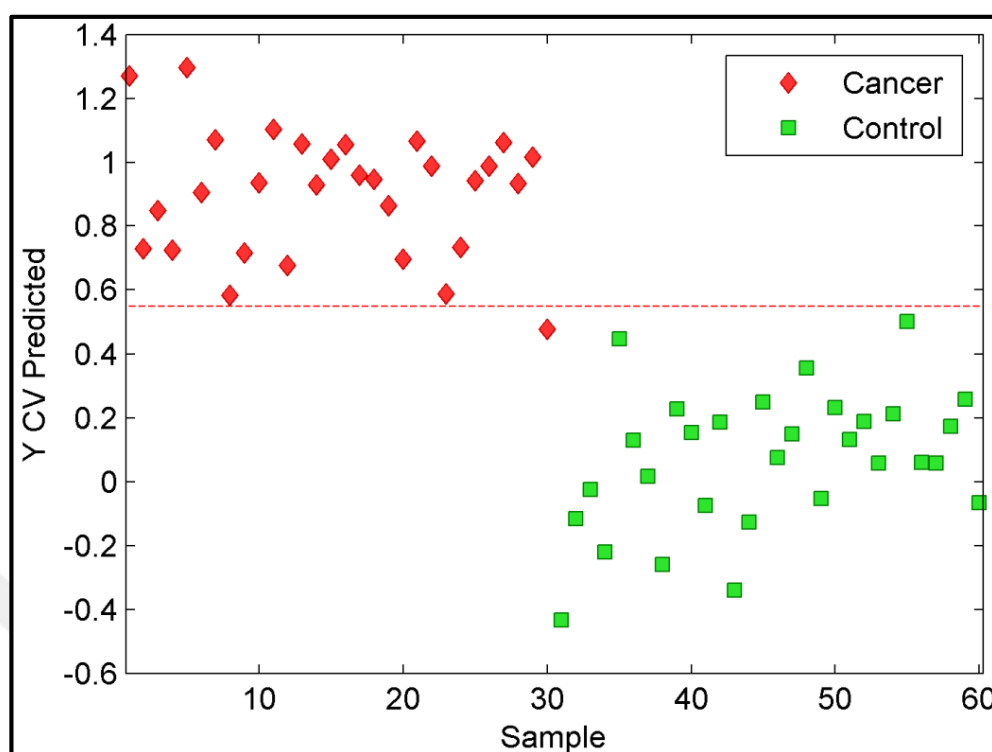


Figure 4.79. PLS-DA scores plot of cancer and control group (8x AgNP, with genetic algorithms (GA)).

Table 4.18. Classification results of SERS spectra of the cancer and the control group obtained using 8x AgNP (GA).

	Cancer vs. Control
Sensitivity	97% (29/30)
Specificity	100% (30/30)
Accuracy	98% (59/60)

The next discrimination was between the chronic disease group and the cancer group. As shown in Figure 4.82, three spectra of the chronic disease group were below the threshold line and four spectra of the cancer group were above the threshold line, yielding a sensitivity of 80 percent, specificity of 87 percent, and an accuracy of 84 percent (Table 4.19). The AUC was 0.94, meaning that PLS-DA model was good at separating two groups (Figure 4.83). R^2 and Q^2 values of the permuted classes were a few standard deviations away from the original ones (Figure 4.84).

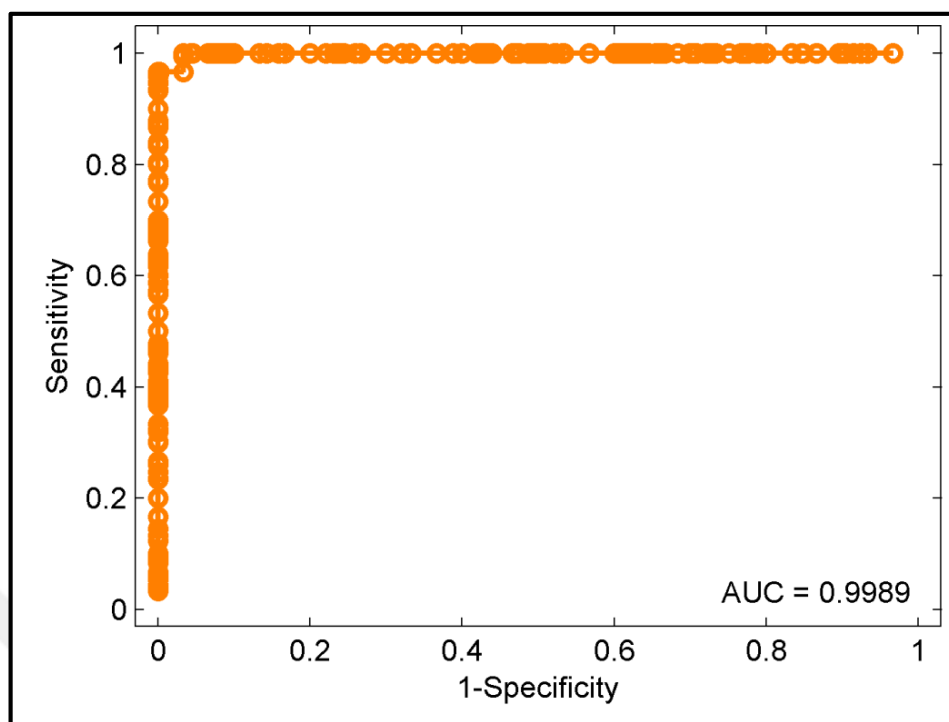


Figure 4.80. ROC curve for cancer and control group (8x AgNP, with GA).

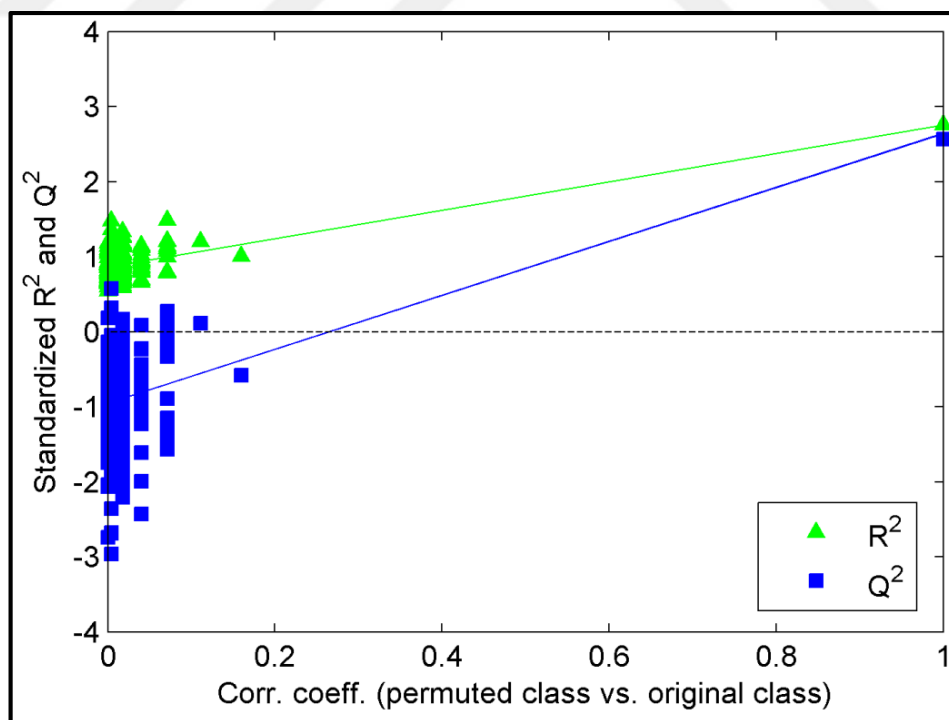


Figure 4.81. Permutation test of cancer vs. control groups (8x AgNP, with GA).

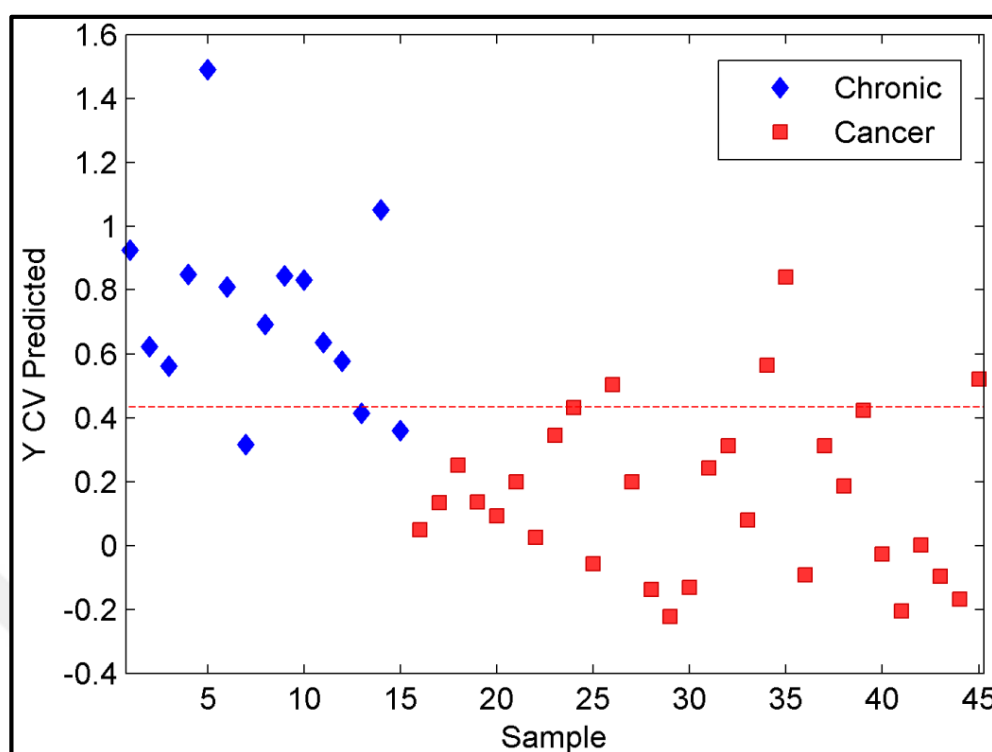


Figure 4.82. PLS-DA scores plot of chronic and cancer groups (8x AgNP).

Table 4.19. Classification results of SERS spectra of the chronic and the cancer group obtained using 8x AgNP.

	Chronic vs. Cancer
Sensitivity	80% (12/15)
Specificity	87% (26/30)
Accuracy	84% (38/45)

By application of GA, 465 Raman shift values were found as better separator of two groups rather than whole 1715 values (Figure 4.85). As a result of the subsequent application of PLS-DA, all spectra of the chronic disease group were discriminated from the cancer group, but three spectra of the latter group were identified as of the former group (Figure 4.86). As a result, a diagnostic sensitivity of 100 percent, a specificity of 90 percent, and an accuracy of 93 percent were reached (Table 4.20). AUC was 0.9667 (Figure 4.87), and R^2 and Q^2 values of the permuted classes were a few standard deviations away from the original ones (Figure 4.88).

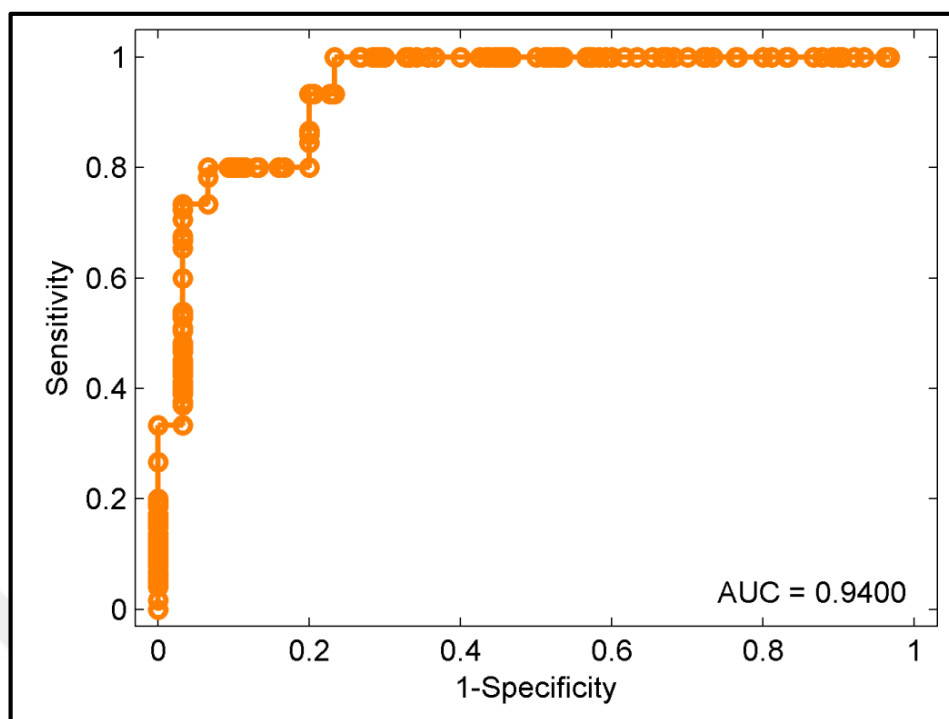


Figure 4.83. ROC curve for chronic and cancer group (8x AgNP).

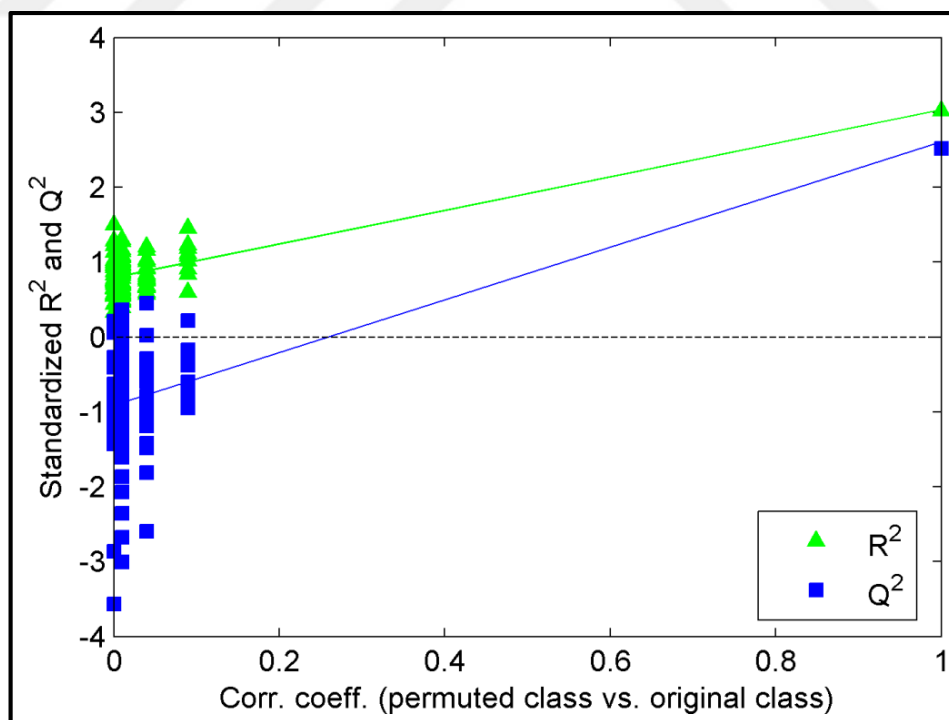


Figure 4.84. Permutation test of chronic vs. cancer groups (8x AgNP).

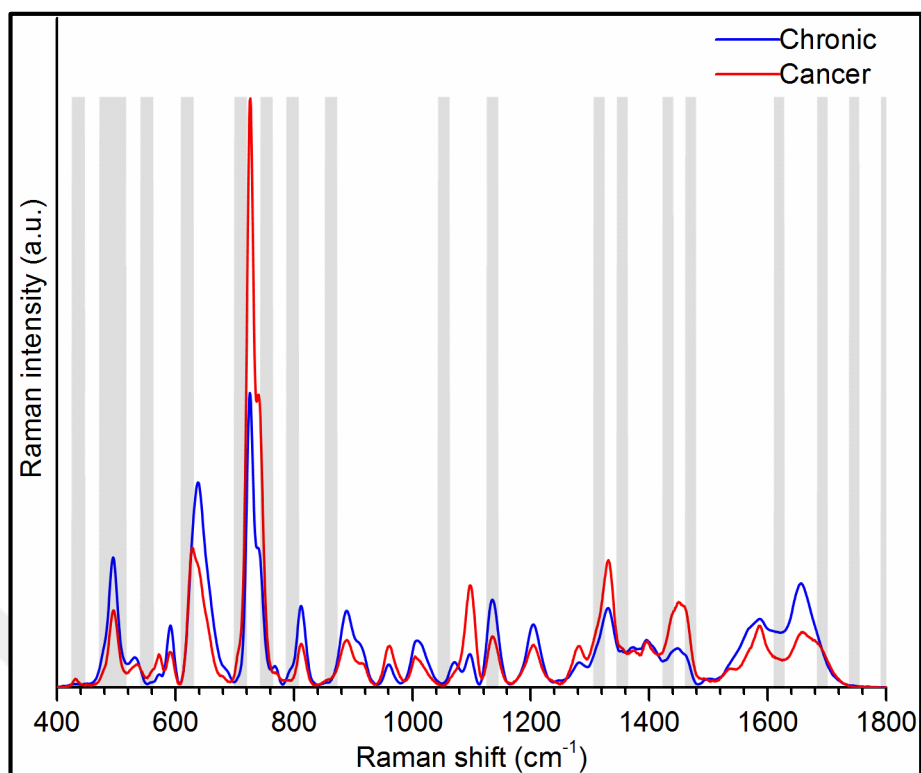


Figure 4.85. Shaded regions are the chosen shift regions with genetic algorithms (GA) for chronic vs. cancer study with 8x AgNP.

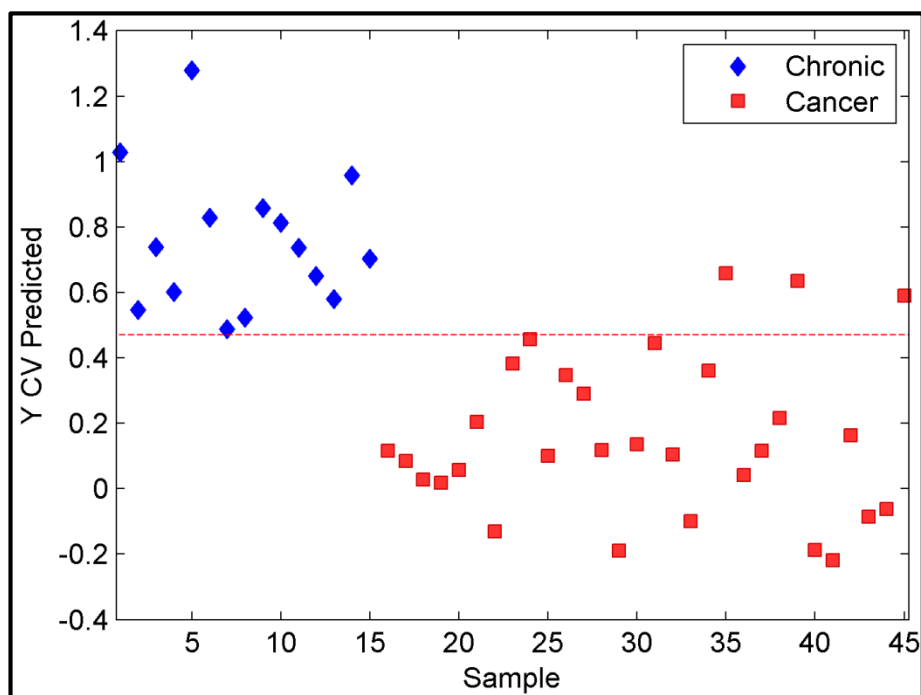


Figure 4.86. PLS-DA scores plot of chronic and cancer group (8x AgNP, with GA).

Table 4.20. Classification results of SERS spectra of the chronic and the cancer group obtained using 8x AgNP (GA).

	Chronic vs. Cancer
Sensitivity	100% (15/15)
Specificity	90% (27/30)
Accuracy	93% (42/45)

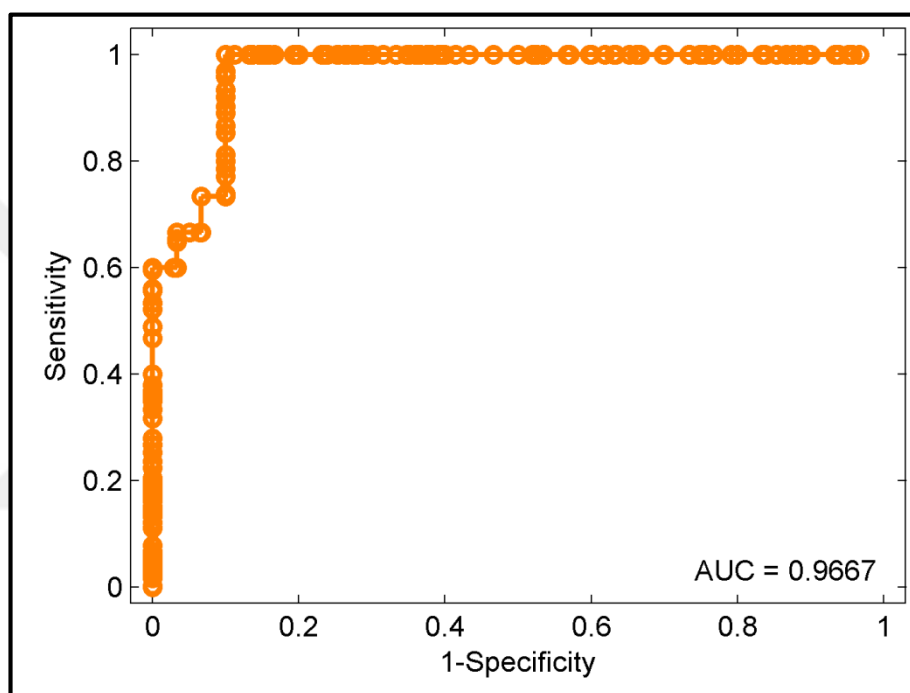


Figure 4.87. ROC curve for chronic and cancer group (8x AgNP, with GA).

The last PLS-DA was performed for discrimination of the chronic disease group and the control group. As seen in Figure 4.89, six spectra of the chronic disease group were below the threshold line and eight spectra of the control group were above the threshold line. Therefore, a sensitivity of 60 percent, a specificity of 73 percent, and an accuracy of 69 per-cent were obtained (Table 4.21). Although sensitivity was similar to the value obtained using 32x AgNP, sensitivity was 17 percent higher. Accuracy was also six percent higher. The area under ROC curve was 0.70 (Figure 4.90). Regarding permutation test, R^2 and Q^2 values of the permuted classes were fairly above the original ones (Figure 4.91).

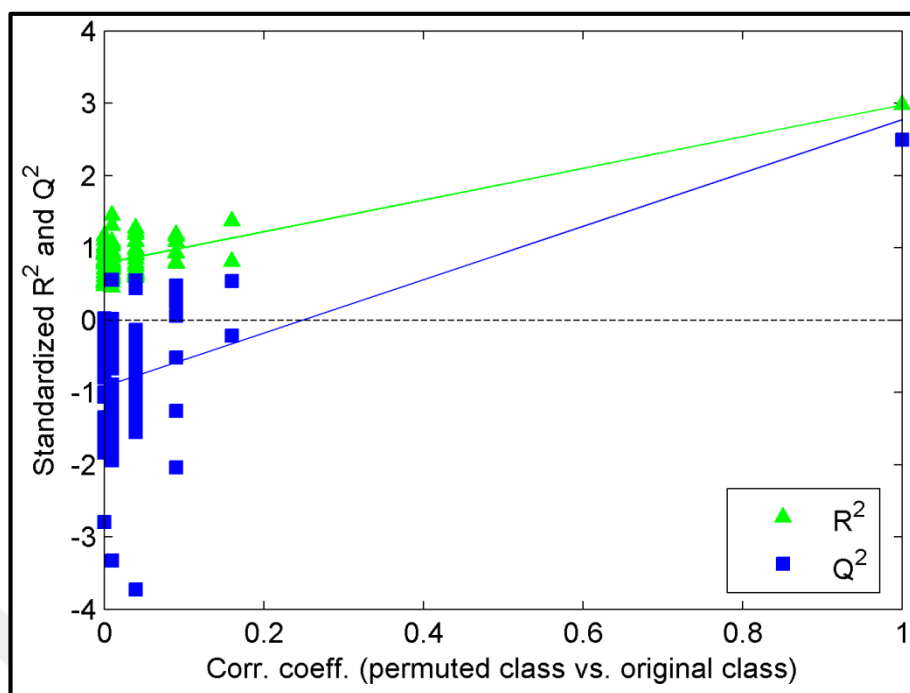


Table 4.21. Classification results of SERS spectra of the chronic and the control group obtained using 8x AgNP.

	Chronic vs. Control
Sensitivity	60% (9/15)
Specificity	73% (22/30)
Accuracy	69% (31/45)

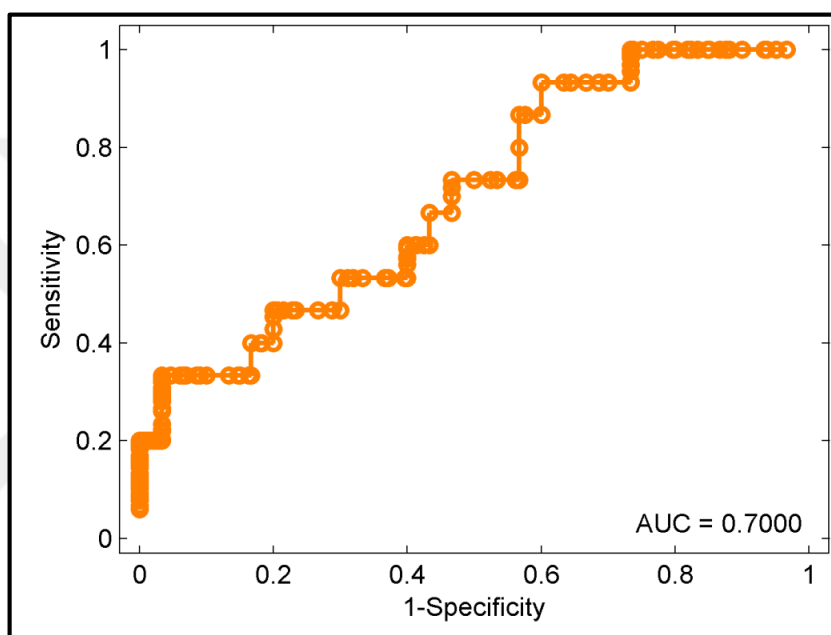


Figure 4.90. ROC curve for chronic and control group (8x AgNP).

Four hundred and fifty Raman shift variables were found by applying GA (Figure 4.92). Using only these variables, PLS-DA performance for discrimination of two groups increased significantly. The results shown above were better than the results obtained using 32x AgNP. Two spectra of the chronic disease group were below the threshold line and two spectra of the control group were above the threshold line (Figure 4.93). A diagnostic sensitivity of 87 percent, a specificity of 93 percent, and an overall accuracy of 91 percent were achieved (Table 4.22). The use of the only important Raman bands and ignoring the other parts of the spectra, accuracy of the PLS-DA model (Figure 4.93) increased by 22 percent (Table 4.22), which enabled discrimination of the SERS spectra of serum samples of the people with chronic diseases and of the healthy people. The area under ROC curve

was 0.9378 (Figure 4.94). Regarding permutation test, R^2 and Q^2 values of the permuted classes were above the original ones (Figure 4.95).

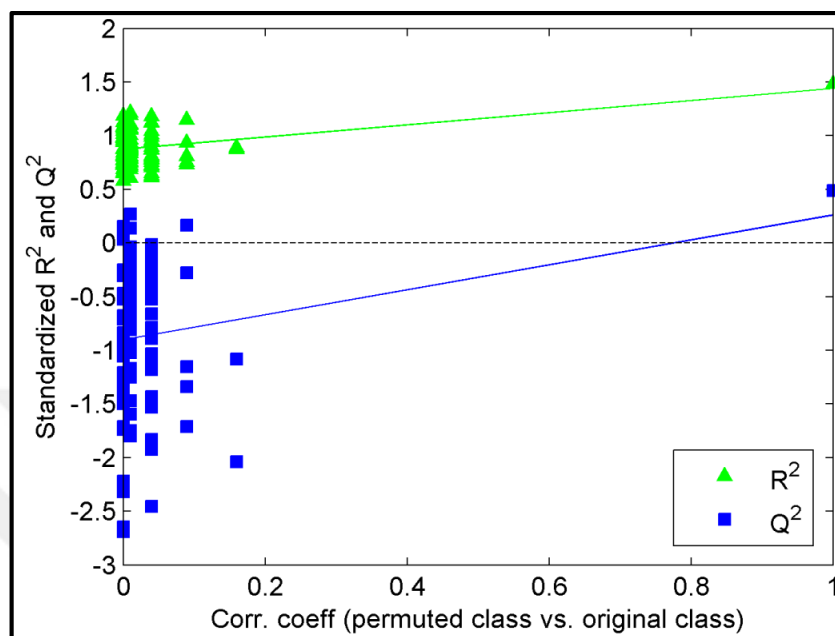


Figure 4.91. Permutation test of chronic vs. control groups (8x AgNP).

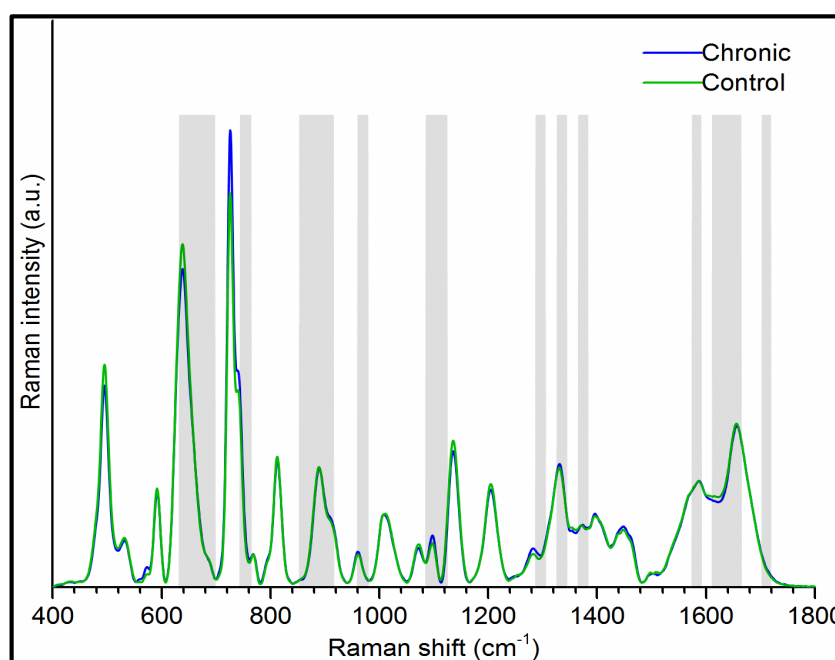


Figure 4.92. Shaded regions are the chosen shift regions with genetic algorithms (GA) for chronic vs. control study with 8x AgNP.

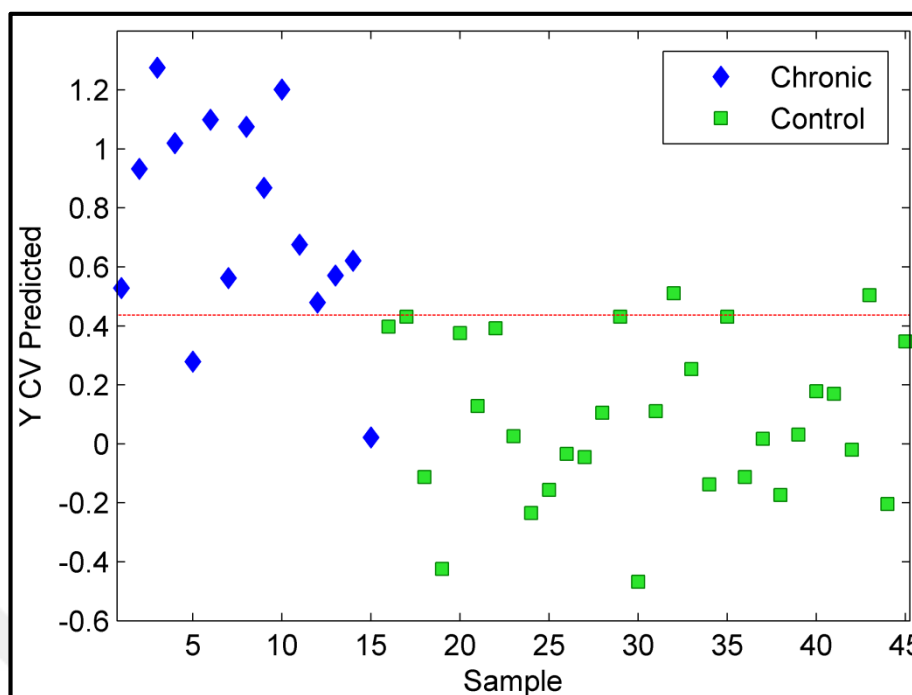


Figure 4.93. PLS-DA scores plot of chronic and control group (8x AgNP, with GA).

Table 4.22. Classification results of SERS spectra of the chronic and the control group obtained using 8x AgNP (GA).

	Chronic vs. Control
Sensitivity	87% (13/15)
Specificity	93% (28/30)
Accuracy	91% (41/45)

Lastly, SERS spectra of serum samples (of 14 patients) collected before and after tumor removal were compared using 32x AgNP colloid. The difference of the mean spectra showed that SERS spectrum of serum after tumor removal started to resemble that of healthy individuals. This finding demonstrated that SERS could be used for monitoring blood composition change after tumor removal. On the other hand, since only 14 serum couples (e.g., serum samples collected before and after tumor removal), standard deviations were high and PLS-DA could not be used for statistical analysis.

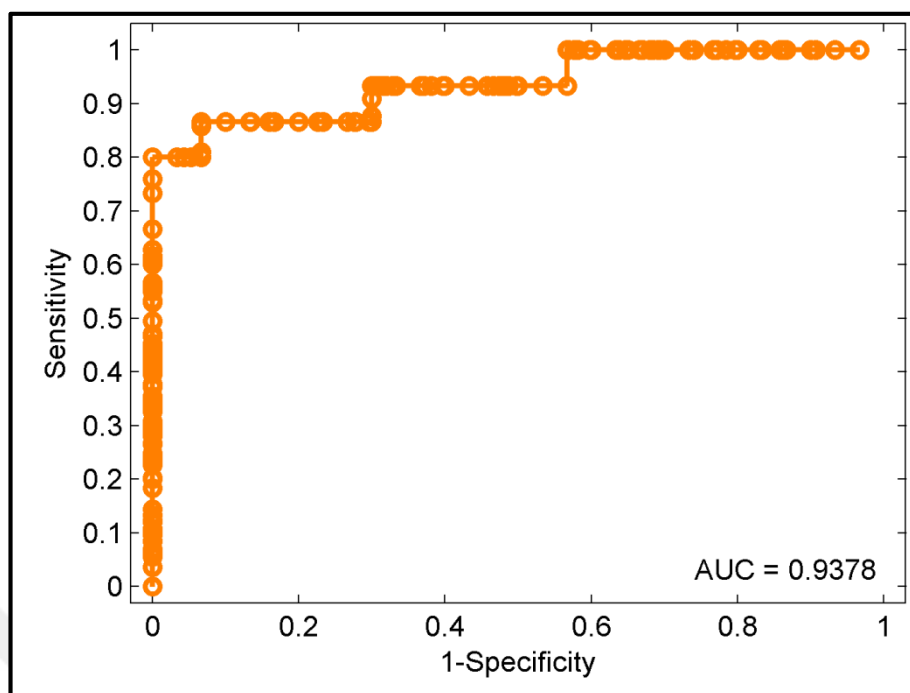


Figure 4.94. ROC curve for chronic and control group (8x AgNP, with GA).

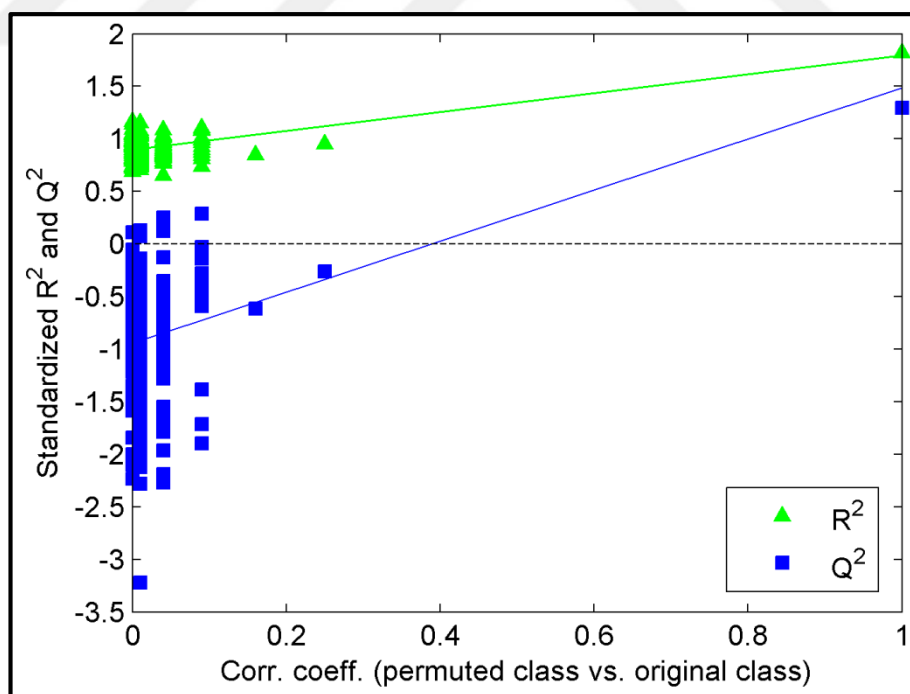


Figure 4.95. Permutation test of chronic vs. control groups (8x AgNP, with GA).

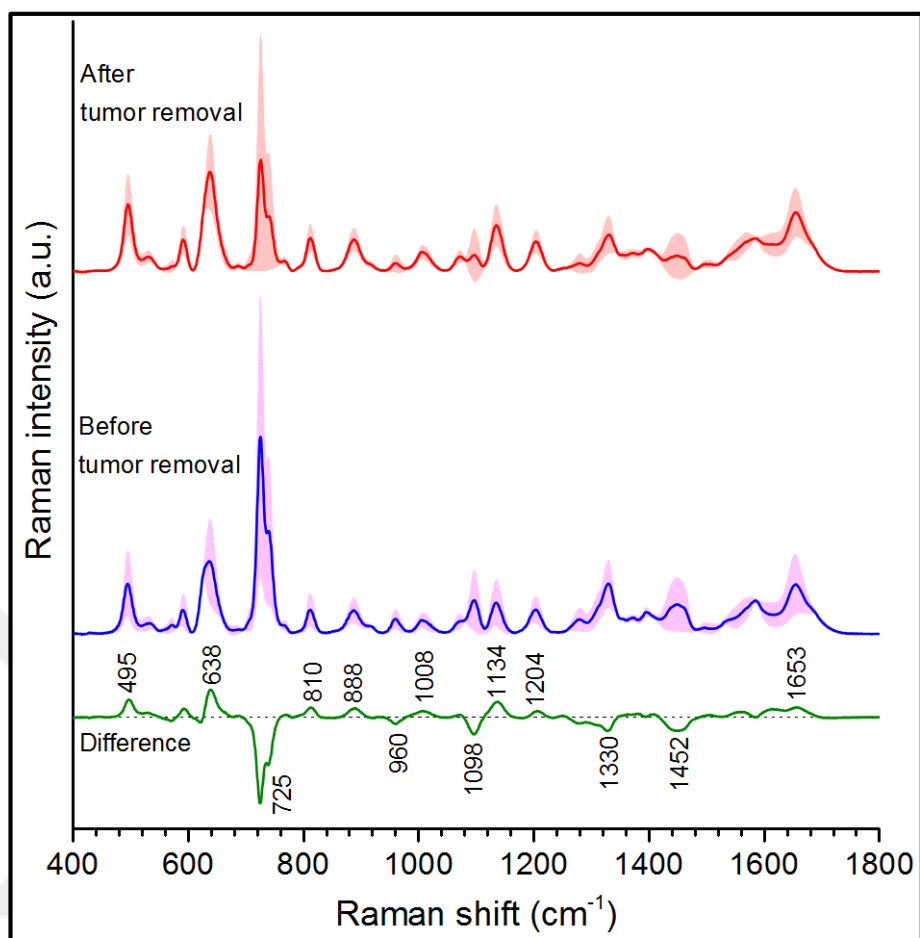


Figure 4.96. SERS spectra of serum samples of cancer patients before and after tumor removal. Shaded areas around the spectra represent the standard deviations.

5. CONCLUSIONS AND FUTURE PERSPECTIVES

In this thesis, a deeper understanding of SERS spectrum of blood serum and discrimination of serum samples of cancer patients from serum samples of chronic diseases patients and healthy individuals were aimed. One original research article was published as outcome that can be found in reference [127]. The study had many levels because blood serum is extremely complex consisting of various type of proteins and biomolecules. First level of the study was protein-SERS. It was important to gain information about the SERS spectra of proteins, especially protein mixtures. As a model, SERS spectra of binary mixtures of eight different proteins were examined. Observation of the effects of different concentrations of proteins in mixtures showed that differentiation of proteins depends both protein size and which statistical method is used. PCA was useful for discrimination of small proteins but not so useful for larger proteins. On the other hand, PLS-DA presented better discrimination abilities. Of course, blood serum contains many other proteins; therefore one can not conclude that PLS-DA is totally useful for SERS study of blood serum proteins. Different statistical methods may be needed when the number of protein type is increased. Nevertheless, findings provided information about the SERS spectra of proteins and their mixtures for the other levels in this thesis study.

Understanding of the origins of blood serum spectra was the other level. Different spectral patterns were observed when different AgNP concentrations were used. This information gave information about which molecules may effects the spectral pattern of the serum SERS spectra. It was understood that uric acid and hypoxanthine contributions are significant but not the only determinants. Many other molecules could contribute to the spectra; therefore some other molecules were spiked into serum and its effects on serum-SERS spectra were observed. Since serum is very complex and many molecules can have similar SERS bands, exact origins of serum SERS spectrum remains as a big challenge. An interesting finding was that proteins were effecting the overall shape of the serum spectra while never contributing their own SERS spectra. Presence of proteins may change orientation some molecules and this may cause change the serum spectra. More detailed analysis are needed in this topic to fully explore the interaction of blood molecules with AgNP surface.

Since uric acid and hypoxanthine were the known molecules, in the next level, SERS spectra of purines and purine derivatives and their binary mixtures were investigated. It was observed that PBS can not be used as model buffer to understand the interactions of uric acid and AgNP in blood serum. The primary buffer system in the body is carbonate-bicarbonate buffer, on the other hand, pH of that buffer changes upon carbon dioxide dissolution in water, damaging the stability of the buffer during experiments. HEPES and Tris buffers can interact with AgNP surface. Borate buffer at pH 8.4 was chosen as a suitable buffer for the study because it did not make any interference on SERS spectra. This time pH was 8.4 but “non-interference” property of the buffer compensated one pH difference. SERS spectra of binary mixtures of purines and purine derivatives showed that interaction of biomolecules with AgNP surface in the presence of other molecules is very complex in nature. Further studies on this topic is needed.

Label-free SERS technique provides fast and low cost analysis. Label-free discrimination of serum of cancer patients from serum of other individuals could provide technique's potential use in clinics in the near future. For the next level in thesis study, SERS spectra of serum of cancer patients, patients with chronic diseases, and healthy individuals were collected using two different AgNP concentrations. PLS-DA was used for discrimination and classification of the spectra. Over than 80-90 percent accuracies were obtained for discrimination of cancer group from control group, and cancer group from chronic disease group. On the other hand, accuracy for discrimination of chronic disease group from control group was less than 70 percent. The use of genetic algorithms with PLS-DA resulted in higher accuracy values (82 percent with 32x AgNP, and 91 percent with 8x AgNP). Results were satisfactory, on the other hand, the amount of serum samples were low to perform a more realistic study. In order to be 100 percent sure about the usefulness of the label-free SERS for this type of studies, sample sizes for each class (i.e, sample sizes of serum samples for each cancer type, for each chronic disease type, and for healthy controls) have to be increased.

REFERENCES

1. Hanahan D, Weinberg RA. Hallmarks of cancer: the next generation. *Cell*. 2011;144(5):646-674.
2. Loeb KR, Loeb LA. Significance of multiple mutations in cancer. *Carcinogenesis*. 2000;21(3):379-385.
3. Baylin SB, Jones PA. Epigenetic determinants of cancer. *Cold Spring Harbor perspectives in biology*. 2016;8(9):1-37.
4. Thompson SL, Compton DA. Chromosomes and cancer cells. *Chromosome Research*. 2011;19(3):433-444.
5. Jeggo PA, Pearl LH, Carr AM. DNA repair, genome stability and cancer: a perspective. *Nature Reviews Cancer*. 2016;16(1):35-42.
6. Tsai W-B, Aiba I, Long Y, Lin H-K, Feun L, Savaraj N, et al. Activation of Ras/PI3K/ERK pathway induces c-Myc stabilization to upregulate argininosuccinate synthetase, leading to arginine deiminase resistance in melanoma cells. *Cancer Research*. 2012;72(10):2622-2633.
7. Bieging KT, Mello SS, Attardi LD. Unravelling mechanisms of p53-mediated tumour suppression. *Nature Reviews Cancer*. 2014;14(5):359-370.
8. Pritchard CC, Mateo J, Walsh MF, De Sarkar N, Abida W, Beltran H, et al. Inherited DNA-repair gene mutations in men with metastatic prostate cancer. *New England Journal of Medicine*. 2016;375(5):443-453.
9. Atchley DP, Albarracin CT, Lopez A, Valero V, Amos CI, Gonzalez-Angulo AM, et al. Clinical and pathologic characteristics of patients with BRCA-positive and BRCA-negative breast cancer. *Journal of Clinical Oncology*. 2008;26(26):4282-4288.

10. Danaei G, Vander Hoorn S, Lopez AD, Murray CJ, Ezzati M, group CRAc. Causes of cancer in the world: comparative risk assessment of nine behavioural and environmental risk factors. *The Lancet*. 2005;366(9499):1784-1793.
11. Bray F, Ferlay J, Soerjomataram I, Siegel RL, Torre LA, Jemal A. Global cancer statistics 2018: GLOBOCAN estimates of incidence and mortality worldwide for 36 cancers in 185 countries. *CA: A Cancer Journal for Clinicians*. 2018;68(6):394-424.
12. Jafari SH, Saadatpour Z, Salmaninejad A, Momeni F, Mokhtari M, Nahand JS, et al. Breast cancer diagnosis: Imaging techniques and biochemical markers. *Journal of Cellular Physiology*. 2018;233(7):5200-5213.
13. Kasivisvanathan V, Rannikko AS, Borghi M, Panebianco V, Mynderse LA, Vaarala MH, et al. MRI-targeted or standard biopsy for prostate-cancer diagnosis. *New England Journal of Medicine*. 2018;378(19):1767-1777.
14. O'connor JP, Aboagye EO, Adams JE, Aerts HJ, Barrington SF, Beer AJ, et al. Imaging biomarker roadmap for cancer studies. *Nature Reviews Clinical Oncology*. 2017;14(3):169-186.
15. Wu L, Qu X. Cancer biomarker detection: recent achievements and challenges. *Chemical Society Reviews*. 2015;44(10):2963-2997.
16. Strutt J. XXXVI. On the light from the sky, its polarization and colour. *The London, Edinburgh, and Dublin Philosophical Magazine and Journal of Science*. 1871;41(273):274-279.
17. Strutt JW. XV. On the light from the sky, its polarization and colour. *The London, Edinburgh, and Dublin Philosophical Magazine and Journal of Science*. 1871;41(271):107-120.

18. Strutt JW. LVIII. On the scattering of light by small particles. *The London, Edinburgh, and Dublin Philosophical Magazine and Journal of Science*. 1871;41(275):447-454.
19. Rayleigh L. X. On the electromagnetic theory of light. *The London, Edinburgh, and Dublin Philosophical Magazine and Journal of Science*. 1881;12(73):81-101.
20. Rayleigh L. XXXIV. On the transmission of light through an atmosphere containing small particles in suspension, and on the origin of the blue of the sky. *The London, Edinburgh, and Dublin Philosophical Magazine and Journal of Science*. 1899;47(287):375-384.
21. Raman CV. On the molecular scattering of light in water and the colour of the sea. *Proceedings of the Royal Society A*. 1922;101(708):64-80.
22. Compton AH. A quantum theory of the scattering of X-rays by light elements. *Physical Review*. 1923;21(5):483-502.
23. Raman CV, Krishnan KS. A new type of secondary radiation. *Nature*. 1928;121(3048):501-502.
24. Tuschel D. Raman thermometry. *Spectroscopy*. 2016;31(12):8-13.
25. Smith E, Dent G. *Modern Raman spectroscopy-a practical approach*. Chichester: John Wiley and Sons Ltd.;2005.
26. Ritchie RH. Plasma losses by fast electrons in thin films. *Physical Review*. 1957;106(5):874-881.
27. Barnes WL, Dereux A, Ebbesen TW. Surface plasmon subwavelength optics. *Nature*. 2003;424(6950):824-830.
28. Maier SA, Atwater HA. Plasmonics: localization and guiding of electromagnetic energy in metal/dielectric structures. *Journal of Applied Physics*. 2005;98(1):10-21.

29. Kelly KL, Coronado E, Zhao LL, Schatz GC. The optical properties of metal nanoparticles: the influence of size, shape, and dielectric environment. *The Journal of Physical Chemistry B*. 2003;107(3):668-677.
30. Sosa IO, Noguez C, Barrera RG. Optical properties of metal nanoparticles with arbitrary shapes. *The Journal of Physical Chemistry B*. 2003;107(26):6269-6275.
31. Stiles PL, Dieringer JA, Shah NC, Van Duyne RP. Surface-enhanced Raman spectroscopy. *Annual Review of Analytical Chemistry*. 2008;1(1):601-626.
32. Fleischmann M, Hendra PJ, McQuillan AJ. Raman spectra of pyridine adsorbed at a silver electrode. *Chemical Physics Letters*. 1974;26(2):163-166.
33. Jeanmaire DL, Van Duyne RP. Surface Raman spectroelectrochemistry: part I. heterocyclic, aromatic, and aliphatic amines adsorbed on the anodized silver electrode. *Journal of Electroanalytical Chemistry and Interfacial Electrochemistry*. 1977;84(1):1-20.
34. Albrecht MG, Creighton JA. Anomalously intense Raman spectra of pyridine at a silver electrode. *Journal of the American Chemical Society*. 1977;99(15):5215-5217.
35. Van Duyne R. Raman applications of Raman spectroscopy in electrochemistry. *Le Journal de Physique Colloques*. 1977;38(5):239-252.
36. Creighton JA, Blatchford CG, Albrecht MG. Plasma resonance enhancement of Raman scattering by pyridine adsorbed on silver or gold sol particles of size comparable to the excitation wavelength. *Journal of the Chemical Society, Faraday Transactions 2: Molecular and Chemical Physics*. 1979;75(1):790-798.
37. Moskovits M. Surface roughness and the enhanced intensity of Raman scattering by molecules adsorbed on metals. *The Journal of Chemical Physics*. 1978;69(9):4159-4161.

38. Moskovits M. Surface-enhanced spectroscopy. *Reviews of Modern Physics*. 1985;57(3):783-826.
39. Persson B. On the theory of surface-enhanced Raman scattering. *Chemical Physics Letters*. 1981;82(3):561-565.
40. Kleinman SL, Frontiera RR, Henry A-I, Dieringer JA, Van Duyne RP. Creating, characterizing, and controlling chemistry with SERS hot spots. *Physical Chemistry Chemical Physics*. 2013;15(1):21-36.
41. Le Ru E, Meyer M, Blackie E, Etchegoin P. Advanced aspects of electromagnetic SERS enhancement factors at a hot spot. *Journal of Raman Spectroscopy*. 2008;39(9):1127-1134.
42. Ding S-Y, Yi J, Li J-F, Ren B, Wu D-Y, Panneerselvam R, et al. Nanostructure-based plasmon-enhanced Raman spectroscopy for surface analysis of materials. *Nature Reviews Materials*. 2016;1(6):1-16.
43. Fang Y, Seong N-H, Dlott DD. Measurement of the distribution of site enhancements in surface-enhanced Raman scattering. *Science*. 2008;321(5887):388-392.
44. Camden JP, Dieringer JA, Wang Y, Masiello DJ, Marks LD, Schatz GC, et al. Probing the structure of single-molecule surface-enhanced Raman scattering hot spots. *Journal of the American Chemical Society*. 2008;130(38):12616-12617.
45. Stranahan SM, Willets KA. Super-resolution optical imaging of single-molecule SERS hot spots. *Nano Letters*. 2010;10(9):3777-3784.
46. Chen H-Y, Lin M-H, Wang C-Y, Chang Y-M, Gwo S. Large-scale hot spot engineering for quantitative SERS at the single-molecule scale. *Journal of the American Chemical Society*. 2015;137(42):13698-13705.

47. Ross MB, Ashley MJ, Schmucker AL, Singamaneni S, Naik RR, Schatz GC, et al. Structure–function relationships for surface-enhanced Raman spectroscopy-active plasmonic paper. *The Journal of Physical Chemistry C*. 2016;120(37):20789-20797.
48. Stewart S, Fredericks P. Surface-enhanced Raman spectroscopy of amino acids adsorbed on an electrochemically prepared silver surface. *Spectrochimica Acta Part A: Molecular and Biomolecular Spectroscopy*. 1999;55(7-8):1641-1660.
49. Suh J, Moskovits M. Surface-enhanced Raman spectroscopy of amino acids and nucleotide bases adsorbed on silver. *Journal of the American Chemical Society*. 1986;108(16):4711-4718.
50. Stewart S, Fredericks P. Surface-enhanced Raman spectroscopy of peptides and proteins adsorbed on an electrochemically prepared silver surface. *Spectrochimica Acta Part A: Molecular and Biomolecular Spectroscopy*. 1999;55(7-8):1615-1640.
51. Ngola SM, Zhang J, Mitchell BL, Sundararajan N. Strategy for improved analysis of peptides by surface-enhanced Raman spectroscopy (SERS) involving positively charged nanoparticles. *Journal of Raman Spectroscopy*. 2008;39(5):611-617.
52. Yu Q, Golden G. Probing the protein orientation on charged self-assembled monolayers on gold nanohole arrays by SERS. *Langmuir*. 2007;23(17):8659-8662.
53. Wabuyele MB, Vo-Dinh T. Detection of human immunodeficiency virus type 1 DNA sequence using plasmonics nanoprobe. *Analytical Chemistry*. 2005;77(23):7810-7815.
54. Barhoumi A, Zhang D, Tam F, Halas NJ. Surface-enhanced Raman spectroscopy of DNA. *Journal of the American Chemical Society*. 2008;130(16):5523-5529.
55. Zhou Q, Zheng J, Qing Z, Zheng M, Yang J, Yang S, et al. Detection of circulating tumor DNA in human blood via DNA-mediated surface-enhanced Raman

- spectroscopy of single-walled carbon nanotubes. *Analytical Chemistry*. 2016;88(9):4759-4765.
56. Sharma B, Bugga P, Madison LR, Henry A-I, Blaber MG, Greeneltch NG, et al. Bisboronic acids for selective, physiologically relevant direct glucose sensing with surface-enhanced Raman spectroscopy. *Journal of the American Chemical Society*. 2016;138(42):13952-13959.
57. Costas C, López-Puente V, Bodelón G, González-Bello C, Pérez-Juste J, Pastoriza-Santos I, et al. Using surface enhanced Raman scattering to analyze the interactions of protein receptors with bacterial quorum sensing modulators. *ACS Nano*. 2015;9(5):5567-5576.
58. Wang H, Zhou Y, Jiang X, Sun B, Zhu Y, Wang H, et al. Simultaneous capture, detection, and inactivation of bacteria as enabled by a surface-enhanced Raman scattering multifunctional chip. *Angewandte Chemie International Edition*. 2015;54(17):5132-5136.
59. Zhou H, Yang D, Ivleva NP, Mircescu NE, Schubert Sr, Niessner R, et al. Label-free in situ discrimination of live and dead bacteria by surface-enhanced Raman scattering. *Analytical Chemistry*. 2015;87(13):6553-6561.
60. Bodelón G, Montes-García Vn, Costas C, Pérez-Juste I, Pérez-Juste J, Pastoriza-Santos I, et al. Imaging bacterial interspecies chemical interactions by surface-enhanced Raman scattering. *ACS Nano*. 2017;11(5):4631-4640.
61. Wang P, Pang S, Chen J, McLandsborough L, Nugen SR, Fan M, et al. Label-free mapping of single bacterial cells using surface-enhanced Raman spectroscopy. *Analyst*. 2016;141(4):1356-1362.
62. Poliseti S, Baig NF, Morales-Soto N, Shrout JD, Bohn PW. Spatial mapping of pyocyanin in *Pseudomonas aeruginosa* bacterial communities using surface enhanced Raman scattering. *Applied Spectroscopy*. 2017;71(2):215-223.

63. Keleştemur S, Çulha M. Understanding and discrimination of biofilms of clinically relevant microorganisms using surface-enhanced Raman scattering. *Applied Spectroscopy*. 2017;71(6):1180-1188.
64. Avci E, Kaya NS, Uçankus G, Culha M. Discrimination of urinary tract infection pathogens by means of their growth profiles using surface enhanced Raman scattering. *Analytical and Bioanalytical Chemistry*. 2015;407(27):8233-8241.
65. Sánchez-Purrà M, Carré-Camps M, de Puig H, Bosch I, Gehrke L, Hamad-Schifferli K. Surface-enhanced Raman spectroscopy-based sandwich immunoassays for multiplexed detection of zika and dengue viral biomarkers. *ACS Infectious Diseases*. 2017;3(10):767-776.
66. Zhan L, Zhen SJ, Wan XY, Gao PF, Huang CZ. A sensitive surface-enhanced Raman scattering enzyme-catalyzed immunoassay of respiratory syncytial virus. *Talanta*. 2016;148(1):308-312.
67. Lin D, Gong T, Hong Z-Y, Qiu S, Pan J, Tseng C-Y, et al. Metal carbonyls for the biointerference-free ratiometric surface-enhanced Raman spectroscopy-based assay for cell-free circulating DNA of epstein-barr virus in blood. *Analytical Chemistry*. 2018;90(12):7139-7147.
68. Li M, Cushing SK, Liang H, Suri S, Ma D, Wu N. Plasmonic nanorice antenna on triangle nanoarray for surface-enhanced Raman scattering detection of hepatitis b virus DNA. *Analytical Chemistry*. 2013;85(4):2072-2078.
69. Fan C, Hu Z, Riley LK, Purdy GA, Mustapha A, Lin M. Detecting food-and waterborne viruses by surface-enhanced Raman spectroscopy. *Journal of Food Science*. 2010;75(5):302-307.
70. Aioub M, El-Sayed MA. A real-time surface enhanced raman spectroscopy study of plasmonic photothermal cell death using targeted gold nanoparticles. *Journal of the American Chemical Society*. 2016;138(4):1258-1264.

71. Pallaoro A, Hoonejani MR, Braun GB, Meinhart CD, Moskovits M. Rapid identification by surface-enhanced Raman spectroscopy of cancer cells at low concentrations flowing in a microfluidic channel. *ACS Nano*. 2015;9(4):4328-4336.
72. Li DW, Qu LL, Hu K, Long YT, Tian H. Monitoring of endogenous hydrogen sulfide in living cells using surface-enhanced Raman scattering. *Angewandte Chemie International Edition*. 2015;54(43):12758-12761.
73. Shen Y, Liang L, Zhang S, Huang D, Zhang J, Xu S, et al. Organelle-targeting surface-enhanced Raman scattering (SERS) nanosensors for subcellular pH sensing. *Nanoscale*. 2018;10(4):1622-1630.
74. Kuku G, Saricam M, Akhatova F, Danilushkina A, Fakhrullin R, Culha M. Surface-enhanced Raman scattering to evaluate nanomaterial cytotoxicity on living cells. *Analytical Chemistry*. 2016;88(19):9813-9820.
75. Manago S, Zito G, Rogato A, Casalino M, Esposito E, De Luca AC, et al. Bioderived three-dimensional hierarchical nanostructures as efficient surface-enhanced Raman scattering substrates for cell membrane probing. *ACS Applied Materials & Interfaces*. 2018;10(15):12406-12416.
76. Lee S, Kim S, Choo J, Shin SY, Lee YH, Choi HY, et al. Biological imaging of HEK293 cells expressing PLC γ 1 using surface-enhanced Raman microscopy. *Analytical Chemistry*. 2007;79(3):916-922.
77. Zavaleta CL, Smith BR, Walton I, Doering W, Davis G, Shojaei B, et al. Multiplexed imaging of surface enhanced Raman scattering nanotags in living mice using noninvasive Raman spectroscopy. *Proceedings of the National Academy of Sciences*. 2009;106(32):13511-13516.
78. Vendrell M, Maiti KK, Dhaliwal K, Chang Y-T. Surface-enhanced Raman scattering in cancer detection and imaging. *Trends in Biotechnology*. 2013;31(4):249-257.

79. Feng S, Lin J, Cheng M, Li Y-Z, Chen G, Huang Z, et al. Gold nanoparticle based surface-enhanced Raman scattering spectroscopy of cancerous and normal nasopharyngeal tissues under near-infrared laser excitation. *Applied Spectroscopy*. 2009;63(10):1089-1094.
80. Henry A-I, Sharma B, Cardinal MF, Kurouski D, Van Duyne RP. Surface-enhanced Raman spectroscopy biosensing: in vivo diagnostics and multimodal imaging. *Analytical Chemistry*. 2016;88(13):6638-6647.
81. Garai E, Sensarn S, Zavaleta CL, Loewke NO, Rogalla S, Mandella MJ, et al. A real-time clinical endoscopic system for intraluminal, multiplexed imaging of surface-enhanced Raman scattering nanoparticles. *PloS One*. 2015;10(4):1-16.
82. Cialla-May D, Zheng X-S, Weber K, Popp J. Recent progress in surface-enhanced Raman spectroscopy for biological and biomedical applications: from cells to clinics. *Chemical Society Reviews*. 2017;46(13):3945-3961.
83. Wang YW, Doerksen JD, Kang S, Walsh D, Yang Q, Hong D, et al. Multiplexed molecular imaging of fresh tissue surfaces enabled by convection-enhanced topical staining with SERS-coded nanoparticles. *Small*. 2016;12(40):5612-5621.
84. Andreou C, Neuschmelting V, Tschaharganeh D-F, Huang C-H, Oseledchyk A, Iacono P, et al. Imaging of liver tumors using surface-enhanced Raman scattering nanoparticles. *ACS Nano*. 2016;10(5):5015-5026.
85. Feng S, Chen R, Lin J, Pan J, Chen G, Li Y, et al. Nasopharyngeal cancer detection based on blood plasma surface-enhanced Raman spectroscopy and multivariate analysis. *Biosensors and Bioelectronics*. 2010;25(11):2414-2419.
86. Feng S, Chen R, Lin J, Pan J, Wu Y, Li Y, et al. Gastric cancer detection based on blood plasma surface-enhanced Raman spectroscopy excited by polarized laser light. *Biosensors and Bioelectronics*. 2011;26(7):3167-3174.

87. Lin D, Feng S, Pan J, Chen Y, Lin J, Chen G, et al. Colorectal cancer detection by gold nanoparticle based surface-enhanced Raman spectroscopy of blood serum and statistical analysis. *Optics Express*. 2011;19(14):13565-13577.
88. Lin D, Pan J, Huang H, Chen G, Qiu S, Shi H, et al. Label-free blood plasma test based on surface-enhanced Raman scattering for tumor stages detection in nasopharyngeal cancer. *Scientific Reports*. 2014;4(1):47-55.
89. Li X, Yang T, Li S, Wang D, Guan D. Detecting esophageal cancer using surface-enhanced Raman spectroscopy (SERS) of serum coupled with hierarchical cluster analysis and principal component analysis. *Applied Spectroscopy*. 2015;69(11):1334-1341.
90. Li S, Zhang Y, Xu J, Li L, Zeng Q, Lin L, et al. Noninvasive prostate cancer screening based on serum surface-enhanced Raman spectroscopy and support vector machine. *Applied Physics Letters*. 2014;105(9):91-95.
91. Chen J, Huang M, Zou Y, Song B, Wang Y, Wang K, et al. Multiple myeloma detection based on blood plasma surface-enhanced Raman spectroscopy using a portable Raman spectrometer. *Laser Physics Letters*. 2016;13(10):105-111.
92. Sánchez-Rojo S, Martínez-Zerega B, Velázquez-Pedroza E, Martínez-Espinosa J, Torres-González L, Aguilar-Lemarroy A, et al. Cervical cancer detection based on serum sample surface enhanced Raman spectroscopy. *Revista Mexicana de Física*. 2016;62(3):213-218.
93. Vargas-Obieta E, Martínez-Espinosa JC, Martínez-Zerega BE, Jave-Suárez LF, Aguilar-Lemarroy A, González-Solís JL. Breast cancer detection based on serum sample surface enhanced Raman spectroscopy. *Lasers in Medical Science*. 2016;31(7):1317-1324.
94. Cervo S, Mansutti E, Del Mistro G, Spizzo R, Colombatti A, Steffan A, et al. SERS analysis of serum for detection of early and locally advanced breast cancer. *Analytical and Bioanalytical Chemistry*. 2015;407(24):7503-7509.

95. Bonifacio A, Dalla Marta S, Spizzo R, Cervo S, Steffan A, Colombatti A, et al. Surface-enhanced Raman spectroscopy of blood plasma and serum using ag and au nanoparticles: a systematic study. *Analytical and Bioanalytical Chemistry*. 2014;406(9-10):2355-2365.
96. Lee P, Meisel D. Adsorption and surface-enhanced Raman of dyes on silver and gold sols. *The Journal of Physical Chemistry*. 1982;86(17):3391-3395.
97. Leopold N, Lendl B. A new method for fast preparation of highly surface-enhanced Raman scattering (SERS) active silver colloids at room temperature by reduction of silver nitrate with hydroxylamine hydrochloride. *The Journal of Physical Chemistry B*. 2003;107(24):5723-5727.
98. Haiss W, Thanh NT, Aveyard J, Fernig DG. Determination of size and concentration of gold nanoparticles from UV–Vis spectra. *Analytical Chemistry*. 2007;79(11):4215-4221.
99. Wan Y, Guo Z, Jiang X, Fang K, Lu X, Zhang Y, et al. Quasi-spherical silver nanoparticles: aqueous synthesis and size control by the seed-mediated Lee–Meisel method. *Journal of Colloid and Interface Science*. 2013;394(1):263-268.
100. Paramelle D, Sadovoy A, Gorelik S, Free P, Hopley J, Fernig DG. A rapid method to estimate the concentration of citrate capped silver nanoparticles from UV-visible light spectra. *Analyst*. 2014;139(19):4855-4861.
101. Bratek-Skicki A, Żeliszewska P, Adamczyk Z, Cieśla M. Human fibrinogen monolayers on latex particles: role of ionic strength. *Langmuir*. 2013;29(11):3700-3710.
102. Wasilewska M, Adamczyk Z, Jachimska B. Structure of fibrinogen in electrolyte solutions derived from dynamic light scattering (DLS) and viscosity measurements. *Langmuir*. 2009;25(6):3698-3704.

103. Wasilewska M, Adamczyk Z. Fibrinogen adsorption on mica studied by AFM and in situ streaming potential measurements. *Langmuir*. 2010;27(2):686-696.
104. Gao F, Lei J, Ju H. Label-free surface-enhanced Raman spectroscopy for sensitive DNA detection by DNA-mediated silver nanoparticle growth. *Analytical Chemistry*. 2013;85(24):11788-11793.
105. Guerrini L, Graham D. Molecularly-mediated assemblies of plasmonic nanoparticles for surface-enhanced Raman spectroscopy applications. *Chemical Society Reviews*. 2012;41(21):7085-7107.
106. Manikas AC, Causa F, Della Moglie R, Netti PA. Tuning gold nanoparticles interfaces by specific peptide interaction for surface enhanced raman spectroscopy (SERS) and separation applications. *ACS Applied Materials & Interfaces*. 2013;5(16):7915-7922.
107. Sánchez-Cortés S, García-Ramos J. Anomalous Raman bands appearing in surface-enhanced Raman spectra. *Journal of Raman Spectroscopy*. 1998;29(5):365-371.
108. Dong X, Gu H, Liu F. Study of the surface-enhanced Raman spectroscopy of residual impurities in hydroxylamine-reduced silver colloid and the effects of anions on the colloid activity. *Spectrochimica Acta Part A: Molecular and Biomolecular Spectroscopy*. 2012;88(1):97-101.
109. Kahraman M, Sur I, Culha M. Label-free detection of proteins from self-assembled protein-silver nanoparticle structures using surface-enhanced Raman scattering. *Analytical Chemistry*. 2010;82(18):7596-7602.
110. Keskin S, Çulha M. Label-free detection of proteins from dried-suspended droplets using surface enhanced Raman scattering. *Analyst*. 2012;137(11):2651-2657.
111. Keskin S, Kahraman M, Çulha M. Differential separation of protein mixtures using convective assembly and label-free detection with surface enhanced Raman scattering. *Chemical Communications*. 2011;47(12):3424-3426.

112. Keskin S, Efeoglu E, Keçeci K, Çulha M. Label-free detection of proteins in ternary mixtures using surface-enhanced Raman scattering and protein melting profiles. *Journal of Biomedical Optics*. 2013;18(3):1-9.
113. Avci E, Culha M. Influence of droplet drying configuration on surface-enhanced Raman scattering performance. *RSC Advances*. 2013;3(39):17829-17836.
114. Das G, Gentile F, Coluccio M, Perri A, Nicastri A, Mearini F, et al. Principal component analysis based methodology to distinguish protein SERS spectra. *Journal of Molecular Structure*. 2011;993(1-3):500-505.
115. Bonnier F, Byrne H. Understanding the molecular information contained in principal component analysis of vibrational spectra of biological systems. *Analyst*. 2012;137(2):322-332.
116. Premasiri WR, Gebregziabher Y, Ziegler LD. On the difference between surface-enhanced Raman scattering (SERS) spectra of cell growth media and whole bacterial cells. *Applied Spectroscopy*. 2011;65(5):493-499.
117. Cheung W, Shadi IT, Xu Y, Goodacre R. Quantitative analysis of the banned food dye sudan-1 using surface enhanced Raman scattering with multivariate chemometrics. *The Journal of Physical Chemistry C*. 2010;114(16):7285-7290.
118. Zhou Z, Han X, Huang GG, Ozaki Y. Label-free detection of binary mixtures of proteins using surface-enhanced Raman scattering. *Journal of Raman Spectroscopy*. 2012;43(6):706-711.
119. Maiti NC, Apetri MM, Zagorski MG, Carey PR, Anderson VE. Raman spectroscopic characterization of secondary structure in natively unfolded proteins: α -synuclein. *Journal of the American Chemical Society*. 2004;126(8):2399-2408.
120. Niaura G, Gaigalas AK, Vilker V. Non-resonant SERS study of the adsorption of cytochrome c on a silver electrode. *Journal of Electroanalytical Chemistry*. 1996;416(2):167-178.

121. Wood BR, Langford SJ, Cooke BM, Lim J, Glenister FK, Duriska M, et al. Resonance Raman spectroscopy reveals new insight into the electronic structure of β -hematin and malaria pigment. *Journal of the American Chemical Society*. 2004;126(30):9233-9239.
122. Hu S, Smith KM, Spiro TG. Assignment of protoheme resonance Raman spectrum by heme labeling in myoglobin. *Journal of the American Chemical Society*. 1996;118(50):12638-12646.
123. Ballabio D, Consonni V. Classification tools in chemistry. part 1: linear models. PLS-DA. *Analytical Methods*. 2013;5(16):3790-3798.
124. Sevilla P, Sánchez-Cortés S, Garcia-Ramos JV, Feis A. Concentration-controlled formation of myoglobin/gold nanosphere aggregates. *The Journal of Physical Chemistry B*. 2014;118(19):5082-5092.
125. Psychogios N, Hau DD, Peng J, Guo AC, Mandal R, Bouatra S, et al. The human serum metabolome. *PloS One*. 2011;6(2):1-23.
126. Nanjappa V, Thomas JK, Marimuthu A, Muthusamy B, Radhakrishnan A, Sharma R, et al. Plasma Proteome Database as a resource for proteomics research: 2014 update. *Nucleic Acids Research*. 2013;42(1):959-965.
127. Avci E, Culha M. Influence of protein size on surface-enhanced Raman scattering (SERS) spectra in binary protein mixtures. *Applied Spectroscopy*. 2014;68(8):890-899.

APPENDIX A: ETHICAL APPROVAL FORM



T.C. YEDİTEPE ÜNİVERSİTESİ

Sayı : 37068608-6100-15-1547
Konu: Klinik Araştırmalar
Etik kurul Başvurusu hk.

04/10/2018

İlgili Makama (Ertuğ Avcı)

Yeditepe Üniversitesi Mühendislik Fakültesi Genetik ve Biyomühendislik Anabilim Dalı Prof. Dr. Mustafa Çulha'nın koordinatör, Sakarya Üniversitesi Sakarya Eğitim ve Araştırma Hastanesi Genel Cerrahi Anabilim Dalı Doç. Dr. Fatih Altıntoprak ve Yeditepe Üniversitesi Tıp Fakültesi Tıbbi Biyoloji Anabilim Dalı Doç. Dr. Soner Doğan'ın sorumlu olduğu "**Kan ve Doku Örneklerinin Yüzece Zenginleştirilmiş Raman Spektroskopisi ile Kanser Tanısı Amaçlı Analizi**" isimli araştırma projesine ait Klinik Araştırmalar Etik Kurulu (KAEK) Başvuru Dosyası (**1523** kayıt Numaralı KAEK Başvuru Dosyası), Yeditepe Üniversitesi Klinik Araştırmalar Etik Kurulu tarafından **03.10.2018** tarihli toplantıda incelenmiştir.

Kurul tarafından yapılan inceleme sonucu, yukarıdaki isimi belirtilen çalışmanın yapılmasının etik ve bilimsel açıdan uygun olduğuna karar verilmiştir (**KAEK Karar No: 903**).

Prof. Dr. Turgay ÇELİK
Yeditepe Üniversitesi
Klinik Araştırmalar Etik Kurulu Başkanı